Faculty of Science
Department of Physics and Astronomy

Identification of Lollipop signature from tau neutrino events in IceCube

Simon Vercaemer

Supervisor:
Matthias Vraeghe

Promotor:
Prof. Dr. Dirk Ryckbosch

Thesis ingediend tot het behalen van de academische graad van Master in de Fysica en Sterrenkunde

Acknowledgement

I would like to thank my parents. They gave me the chance to study and motivated me to take this opportunity.

I would like to thank the IceCube group in Ghent for the feedback on my ideas and the input of new ideas to make this thesis a better thesis. Also the very interesting experience they offered me is deeply appreciated, it has been a pleasant year. I also would like to thank my colleague students whom I shared an office with, the year would have been less pleasant without you.

My deepest appreciation goes to the people who read this, for them incomprehensible, document to make it textually better. I would like to thank Matthias again for reading this document and correcting violations to both the English language and the truth.

As last, I would like to thank the Flemish tax payers for funding my education.

Thank you.

Contents

List of Figures

List of Tables

Introduction

From all the elementary particles, neutrinos are probably the weirdest. Far less is known about neutrinos than about any other of the elementary particles. Even the Higgs boson has better measured parameters than neutrinos, and it only got discovered in 2012. Some properties are luckily known, that it only interacts via the weak force for example. This makes neutrinos interesting to do astronomy astronomy.

As its name suggests, the weak force is very weak. A weakly interacting particle can easily travel straight through planets. This behaviour is both a blessing and a curse. Since neutrinos go straight through about everything, one can look straight through intergalactic gas clouds. This same trait makes them almost impossible to detect; immense instruments are therefore required to find them at a reasonable rate.

The IceCube Neutrino Observatory is worlds largest neutrino detector, having a sensible volume of one cubic kilometre of ice. It is build on the South Pole, 1.5 kilometre deep in the Antarctic ice. This cubic kilometre is equipped with more than 5000 basketball sized detectors called DOMs (digital optical mode). These DOMs consist of a photomultiplier tube (PMT) which collects light and an electronics segment which reads out and digitizes the PMT signal and sends the digitized signal to the surface.

There are three types of neutrinos: electron, muon and tau. Electron and muon neutrinos are readily produced in various processes in both cosmic accelerators and in the atmosphere. There is however no way to produce a significant flux of tau neutrinos from these sources. Detection of a tau neutrino therefore implies neutrino oscillations and a source from outside our solar system. This can lead to a better determination of the oscillation parameters, a better understanding of the cosmic accelerators and an improvement in the determination of the neutrino masses.

In this thesis, a search for tau neutrinos is performed using the Lollipop detection channel. In the first chapter of this thesis, all necessary physics will be introduced, a historical overview of neutrino physics will be given and the production of high energy neutrinos will be explained. The second chapter explains the physics of neutrino detection and the IceCube detector. Next to all tau neutrino detection channels, also background sources to tau neutrino detection and other physics goals of IceCube are explained in chapter two. A short third chapter explains the used software and simulation techniques. In chapter four, the cuts based on Monte Carlo are explained and a comparison to real data is done. Finally in chapter 5, a quick summary is given. In the appendices, the code is explained, ideas for more cuts are offered and additional plots are presented to show the effect of the different cuts.

Chapter 1

Neutrinos

In this first chapter, a background of all physical and historical processes that are relevant to this thesis is given. In the first part of this chapter, the Standard Model will be introduced. This will be done in broad lines except for neutrinos, these will be treated more elaborately. Where possible, mathematics will be avoided. In the second part of this chapter, the historical evolution of our understanding about neutrinos will be sketched. This sketch will contain only the major events. Books can, and are, written simply about the topic of the history of neutrinos; this is not the place to reproduce such a work. In the last part of this chapter, the production of high energy neutrinos in the universe will be explained. Along with this, also the production of high energy charged particles will be considered.

1.1 The Standard Model

One of the most quoted theories in physics is the Standard Model of particle physics. Its goal is to predict the various interactions between the different elementary particles via the different fundamental forces. This model has been tested by various experiments all over the world during the last five decades and was confirmed to predict physics with an extraordinary precision. It works so good that it somehow acquired capital letters in its name.

The Standard Model is generally depicted by an image such as Figure 1.1. This gives a nice overview of the different elementary particles that exist and at the same time gives a couple of properties of those particles. It is however also a very limited view of the Standard Model since not a single Lagrangian is written down. Therefore, all strengths and types of the interactions are missing from this simple representation.

The Standard Model can be split in two main parts by looking at the spin of the particles. On the right side of the figure (fourth and fifth column) are the bosons, these have integer spin. Particles on the left (first three columns) have half integer spin and are called fermions. Bosons have a double function. On the one hand, they are fundamental particles just as the fermions. In that manner, they interact with their environment like any other *real particle*. On the other hand, they also fulfil a regulating function; they 'carry' the fundamental forces between real particles. The Higgs-Englert-Brout boson is an exception to that, it exists so that the Z boson and the photon have the mass they have [1, 2]. Even though that is a very interesting topic in itself, this is of no consequence for this thesis and won't be mentioned any further.

1.1.1 Forces and Carriers

A particle that carries a force is a *virtual particle*. Unlike real particles, a virtual particle doesn't follow (all of) the normal rules of physics. Such a particle can be *off shell*, meaning that it doesn't have the mass it would have if that particle was a real particle. A particle can't be too far off shell; the further it is from the mass of the real particle (*on shell*), the less likely it will be for a force to propagate in this way [3]. Virtual particles can also never be detected, they can only be seen via the influence they have on real particles. Other physical principles, such as causality and conservation of energy and momentum, are obeyed by both virtual and real particles.

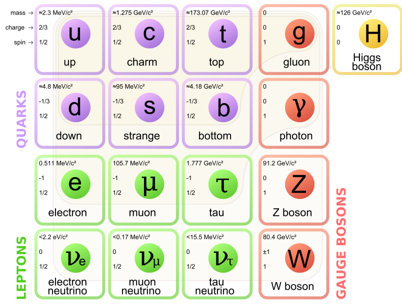

Figure 1.1: The Standard Model[1]. The fermions are in the first three columns, the fourth and fifth column contain the bosons.

The fundamental forces are the strong force, the weak force and electromagnetism[2]. Each of these forces has its own quantum number. For the strong force, that is colour. Colour comes in six different varieties, three pairs of colour and anti-colour. These colours are green, red and blue [4]. The electromagnetic force has electric charge of the electron as its quantum number ($q = 1.602 \cdot 10^{-19}\ C = 1e$). Particles that have electric charge follow the Coulomb laws.

The quantum number of the weak force is called weak isospin. The weak isospin and electric charge can be combined into the weak hypercharge. This is the quantum of the electroweak force, a unification of the weak and electromagnetic force and part of the Standard Model[3] [5].

The Strong Force

The gluon (g) is the gauge boson responsible for carrying the strong force. It has spin 1, is massless and has no electrical charge. It does however have a colour and

[1]Figure taken from Wikipedia.

[2]Gravity is not included in this list since it much weaker than the weakest of the other forces. Its effect is truly negligible on the very small mass scales considered in the subatomic world.

[3]It are things like these that show how incomplete Figure 1.1 is, this unification is the very core of the Standard Model

an anti-colour component, this makes it the only gauge boson that has the charge of the force it carries itself. Due to the three kinds of colours, eight different gluons exist.

Because they have their own charge, different gluons interact with each other. This is the reason why they can't move freely even though they are massless. If a gluon were to wander too far, it would be pulled back to the other gluons. Since the transmission of a force requires a gauge boson to travel between the two interacting particles, the strong force has a limited range.

The strong force binds quarks (purple entries in Figure 1.1) to a vast array of hadrons[4]. All these hadrons, except for the proton and neutron, decay almost instantaneously after their creation. The strong force also keeps nuclei bound in the nucleus of atoms. Because the limited range of the strong force, only atoms up to a certain mass number can exist. Beyond that point, the diameter of the nucleus grows larger than the range of the strong force. The strong interaction then can no longer compete with the repelling Coulomb force between the protons and the nucleus breaks up.

The Electromagnetic Force

The photon (γ) carries the electromagnetic force. Just as the gluon, it has spin 1, no mass and no electrical charge. The fact that it doesn't have an electric charge gives it a less exotic appearance than gluons, e.g. they have an infinite range as their masslessness suggests and they don't interact among themselves.

The electromagnetic force binds electrons into the nucleons to form atoms and binds the atoms to molecules. Next to these properties, the electromagnetic force is also responsible for a couple of very interesting phenomena when it comes to charged particles with high energy. These effects are, among others, bremsstrahlung and the emission of Cherenkov light. These phenomena will be treated extensively in Section 2.1, where the detection principle of the IceCube Neutrino Observatory is explained.

Unlike the other gauge bosons, real photons can wander freely through space. These real photons make up the electromagnetic spectrum, all the way from the high energetic gamma rays over the visual spectrum to the low energetic radio waves. Photons are often produced in reactions as a way to carry away energy. For example the light emitted by stars is created in the core where nuclear fusion takes place and photons are produced to take away excess energy in the newly formed nuclei [7].

The Weak Force

The weak force can be split into two distinct categories, each with its own boson. On the one hand, there is the charged current. Interactions that happen via the charged current are mediated by the electrically charged W^+ and W^- bosons. These two bosons are simply each others antiparticle, they will be referred to simply as the

[4]A list of all known hadrons and their properties can be found in reference [6]

W boson from now on. The electrical charge will always be clear from the context. On the other hand, there is the neutral current. This part of the weak force is modulated by the electrically neutral Z boson.

Both these bosons are very heavy, W and Z have a respective mass of 80.385 GeV and 91.1876 GeV [6]. This is the main reason why the weak force is so weak, it is extremely improbable to create these particles at low energies. At higher energies, when the rest mass energy of the W and Z boson are negligible contributions to the total energy of the considered system, the weak force is as strong as the electromagnetic force. This is clear from the fact that these forces can be united in the electroweak theory [8].

The weak charge interacts with all types of fermions, so the different interactions are devided into different categories, based on the involved particles. These categories are leptonic, semileptonic and non-leptonic processes in which respectively only leptons, leptons and quarks or only quarks are involved. All three categories contain decays of unstable particles. In the leptonic and semileptonic categories, there are also neutrino interactions. Since neutrinos only have a weak charge, they can only interact via the weak force. The other fermions can also interact via the weak force, but interactions via the other forces are much more probable [9].

When considering day to day situations, the weak force is mainly responsible for radioactive β decay. When one goes beyond unstable nuclei and more exotic particles are considered, the weak force is responsible for the decay of muons and charged pions. For most hadrons, decay via the electromagnetic or strong interaction is possible and the weak force is responsible for only a part of the decays. This *branching fraction* varies from more than 60% to insignificant amounts.

The weak force is the only manner of interaction for neutrinos. More information about neutrinos and their modes of interaction will be given in Section 1.1.4.

1.1.2 Quarks

Quarks, the six purple entries in the upper left corner of Figure 1.1, are the heaviest type of fermions (spin 1/2). They are the building blocks of all hadrons, which make up 99.99% of all visible mass in the universe[5]. Although there are six types of quarks, only two of them contribute to the stable matter in the universe. These two are the up and the down quark, they populate the first *generation* of quarks. The quarks in the second generation received the names charm and strange, those in the third are named top and bottom.

Each generation of quarks consists of a positively charged ($q = +2/3e$) or *up-type* quark and a negatively charged ($q = -1/3e$) or *down-type* quark. The fact that these particles have an electrical charge that is a fraction of the quantum of the electromagnetic force is no problem; quarks also have a colour charge. Therefore, quarks always have to come in groups such that the colour charge of the group is

[5]The visible mass makes up only 4% of the entire universe [10].

neutral. It is impossible to find a combination of quarks that is white[6] and has a non-integer electrical charge. Since the strong force is so much stronger than the electromagnetic force, the electromagnetic force might as well not exist inside a hadron. From the outside perspective, the electrical charge is added to an integer times e and the hadron seems like a point particle to the electromagnetic force.

The different generations of quarks have mostly the same properties, only their mass increases with increasing generation. All quarks are stable with respect to the strong and electromagnetic interaction, they are however not stable for the weak interaction. Except for the heaviest quark, the top quark, the cross section for decay is so low that they bind to hadrons long before they can decay. The newly formed hadrons that hold these unstable quarks do however decay. In those decays, the quark content is not necessarily conserved. The top quark ($m = 172.0$ GeV) is the only quark heavy enough to be able to decay to a W boson and a down-type quark [11].

Hadronization

The reasoning why the strong force is a short range force can also be made for quarks. If a quark goes wandering off alone, it is quickly pulled back by the other quarks in the hadron. Even though it is not known whether or not the total electric charge in the universe is zero, one could make the same reasoning with the Coulomb force and wonder why atoms are so easily ionized. It is at this point that a justification of the names of the fundamental forces shows up. At an interaction energy of 1 GeV, the strong force is approximately 6 orders of magnitude stronger than the electromagnetic force [12].

It is however always a possibility that a quark is ejected with so much kinetic energy that it can not be pulled back. If this is the case, a process called hadronization takes place. In the ever growing potential field between the two quarks, enough potential energy will eventually be stored to create two more quarks, thus reducing the total potential field present [13]. These created quarks will have an amount of kinetic energy themselves. If this energy again exceeds the particle creation threshold, more particles will be created. If not, two hadrons will come out of this interaction.

Really energetic reactions can create a true shower of particles in this way. Due to the intrinsic probabilistic quantum mechanical nature of pair creation and decay of particles, the final decay products of such a shower can only be predicted approximately. However, several software packages exist that can simulate such a hadronizition process very reliably.

1.1.3 Leptons

Leptons (the green entries in the lower left of Figure 1.1) are, just as the quarks, fermions with spin 1/2 and are divided into three generations or *flavours* of each

[6]Particles that have no net colour charge are called white.

two particles. Again, the three generations are mostly the same except for mass and therefore decay possibilities. Unlike quarks, the masses of the two particles within the same generation differ by many orders of magnitude. The heavier charged leptons have well determined masses that exceed 500 keV, the uncharged leptons or *neutrinos* (symbolised with ν_x, where x indicates the flavour of the neutrino), do not have a well measured mass (yet). An upper limit of 2 eV to the electron neutrino mass is set, based on spectroscopy of the electron freed in tritium decay [14].

Leptons do not have a colour charge, they are invisible to the strong interaction. Both charged leptons and neutrinos have a weak charge but only the charged leptons have an electrical charge. This makes neutrinos very interesting but also hard to find, they are the only particle to interact only via the aptly named weak interaction.

Charged Leptons

The charged leptons (electron e, muon μ and tau lepton τ) all have electrical charge $q = -e$. This makes them stable with respect to the electromagnetic interaction, which conserves electrical charge. The electron is the lightest charged lepton ($m =$ 511 keV) and is therefore stable even for the weak interaction. The muon is heavier ($m = 105.66$ MeV) than the electron but still lighter than the lightest charged hadron[7]. Therefore there is only one possible decay channel for the muon, $\mu^- \rightarrow e^-\bar{\nu}_e\nu_\mu$. This decay is mediated by a heavily off-shell W^-, the muon therefore has a long lifetime of $2.20 \cdot 10^{-6}$ s.

The tau lepton (τ) has a mass of 1.777 GeV, well above that of the lightest charged hadrons. A multitude of possible tau decay products exists, all of which start with the decay of the τ to a virtual W-boson and a tau-neutrino. The W subsequently decays into a lepton or a quark pair. This process is depicted for decay in a muon and muon neutrino in Figure 1.2 with a so called *Feynman diagram*, the dashed line of the W boson indicates that that particle is a virtual particle. In case of a decay to a quark pair, hadronization takes place and a number of different hadrons can be formed. Those are mostly charged pions and kaons, although neutral pions and kaons show up almost half the time when a hadronic decay takes place.

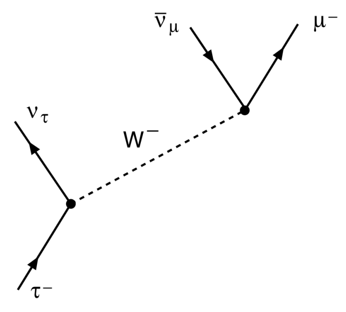

Figure 1.2: Decay of a τ^-

1.1.4 Neutrinos

From the fundamental particles, the least is known about neutrinos. More properties are known about the Higgs boson than about neutrinos, and it only got discovered

[7]This is the pion, $m_\pi = 139.57$ MeV

in 2012 [15]. Even the very nature of neutrinos, are they their own anti-particle (Majorana particle) or not (Dirac particle)[8], is not yet known [16]. Unlike the other leptons, their mass is not accurately known. There is an upper limit to their mass, but that does not yield the entire picture. It is also not known which neutrino is the heaviest, which is the second and which is the lightest. It is known that from the three neutrinos, two are close together in mass and one is further off. The mass of the further off neutrino with respect to the other two is not known (the $1-2-3$ vs. $3-1-2$ scenario). Luckily, some other things are known.

The *helicity* of neutrinos has been measured very soon after the experimental confirmation of the existence of neutrinos[9] [17]. Helicity h is a property of particles with non-zero spin defined as

$$h = \frac{\mathbf{s} \cdot \mathbf{p}}{|\mathbf{s}| \cdot |\mathbf{p}|} \tag{1.1}$$

in which $\mathbf{s}$ is the spin vector and $\mathbf{p}$ is the momentum vector. Particles for which the spin and momentum point in the same direction have helicity $+1$. Particles with spin and momentum pointed in opposite directions have helicity -1. Particles with positive helicity are said to be right handed, particles with negative helicity are left handed. Neutrinos were found to have negative helicity.

Neutrino Oscillations

Even though the mass of the neutrinos is not yet known, it is certain that all neutrino flavours have mass [18]. This is because *neutrino oscillations*, a neutrino changing its flavour without any interaction whatsoever, can not happen with massless neutrinos. Even though this process has been confirmed experimentally [19, 20], some of the various oscillation parameters have not yet been determined to satisfying precision. These oscillation parameters fix relations between the neutrino masses, but do not set an exact mass scale [21]. Absolute mass measurements based on cosmological arguments set an upper limit on the summed mass of the three flavours as low as 0.23 eV[10] [23–26].

Neutrinos only interact via the weak force, which conserves flavour. When neutrinos propagate through space, they don't interact and flavour is of no importance. What does count is the energy and rest mass of the particle. To decide which flavour or mass a neutrino should have, one can imagine the particle as a point in a three dimensional space[11] with two different orthonormal bases. One basis has to be used when interactions take place, the different axis on that basis are the so called *flavour eigenstates*, indicated with ν_e, ν_μ or ν_τ. When considering propagation, the other basis has to be used. On this basis, the axis represent the *mass eigenstates*, indicated with ν_1, ν_2 or ν_3.

[8] This is currently being investigated by various [6] experiments but no conclusive result has presented itself yet.

[9] More information on the history of neutrinos will be given in Section 1.2.

[10] One measurement based on gravitational lensing predicts neutrino masses of 1.5 eV [22].

[11] Three for the number of flavours.

Parameter	best fit ($\pm 1\sigma$)	3σ
$sin^2\theta_{12}$	$0.312^{+0.018}_{-0.015}$	$0.265 - 0.364$
$sin^2\theta_{23}$	$0.42^{+0.08}_{-0.03}$	$0.34 - 0.64$
$sin^2\theta_{13}$	$0.025^{+0.007}_{-0.008}$	$0.005 - 0.050$

Table 1.1: Best fit values and 3σ allowed ranges of the 3-neutrino oscillation parameters [27, 28].

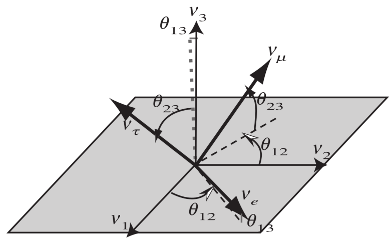

Figure 1.3: Mixing angles between neutrino flavour and mass eigenstates. The shown angles are the experimental values of the angles indicated in Equation 1.3 [9].

The flavour and mass eigenstates can be converted into one another by the Cabibbo-Kobayashi-Maskawa matrix,

$$\begin{pmatrix} \nu_e \\ \nu_\mu \\ \nu_\tau \end{pmatrix} = \begin{pmatrix} U_{e1} & U_{e2} & U_{e3} \\ U_{\mu 1} & U_{\mu 2} & U_{\mu 3} \\ U_{\tau 1} & U_{\tau 2} & U_{\tau 3} \end{pmatrix} \begin{pmatrix} \nu_1 \\ \nu_2 \\ \nu_3 \end{pmatrix}. \tag{1.2}$$

This matrix U can be written as

$$U = \begin{pmatrix} 1 & 0 & 0 \\ 0 & c_{23} & s_{23} \\ 0 & -s_{23} & c_{23} \end{pmatrix} \begin{pmatrix} c_{13} & 0 & s_{13}e^{-i\delta} \\ 0 & 1 & 0 \\ -s_{13}e^{i\delta} & 0 & c_{13} \end{pmatrix} \begin{pmatrix} c_{12} & s_{12} & 0 \\ -s_{12} & c_{12} & 0 \\ 0 & 0 & 1 \end{pmatrix} P, \tag{1.3}$$

where s_{ij} and c_{ij} are respectively the sine and cosine of θ_{ij}, the euler angles between the two bases. For the specific case of the flavour and mass base, these angles are called *mixing angles*, they are depicted in Figure 1.3. The angle δ is a $\mathcal{CP}$ violation phase. This effect has not yet been observed nor excluded experimentally so far; this parameter is only there for theoretical reasons. The matrix P can be written as

$$P = \begin{pmatrix} 1 & 0 & 0 \\ 0 & e^{i\alpha_1/2} & 0 \\ 0 & 0 & e^{i\alpha_2/2} \end{pmatrix}.$$

The parameters α_1 and α_2 are two more $\mathcal{CP}$ violating phases. The matrix P is necessary only if neutrinos are Majorana particles.

Combining results from different experiments that measure different parameters such as flux and energy spectrum of various sources can lead to a fit of the different angles. The results as of 2012 are listed in Table 1.1.

Constraints on neutrino masses

When a neutrino is created, it is created in a specific flavour eigenstate. To consider propagation towards its point of interaction, the neutrino has to be converted to the mass basis and it finds itself in a superposition of different mass eigenstates Ψ.

$$|\Psi\rangle = \phi_1 |\psi_1\rangle + \phi_2 |\psi_2\rangle + \phi_3 |\psi_3\rangle \tag{1.4}$$

where ψ_1, ψ_2 and ψ_3 are the three mass eigenstates. The initial value of the phase factors ϕ_1, ϕ_2 and ϕ_3 are determined by the mixing angles. As any quantum mechanical system, the wave function of this system undergoes time evolution while it propagates. Every phase factor can be written on any moment as

$$\phi_i(t) = \phi_i(0) \cdot e^{-iE_i t} \tag{1.5}$$

with $t = 0$ the moment of interaction [29].

At the point of interaction, the wave function needs to be evaluated in flavour eigenstates again and the wave function collapses to one flavour state. The probability with which the wave function collapses to any flavour state l is given by

$$P(\nu_l | k, E) = |\langle \psi_l | \Psi \rangle|^2 \tag{1.6}$$

where k and E are respectively the initial flavour and energy of the neutrino. The sum of these probabilities for the three flavours e, μ and τ should always be exactly 1.

Looking at an example of neutrino oscillation with only two flavours and two mass eigenstates will show how the mixing angles and propagation yields relations between the different masses. Even though this example is incomplete, it captures the full workings of neutrino oscillations while avoiding a lot of mathematics. Adding in the third neutrino flavour and mass eigenstate would not introduce additional information or clarity, it however adds two mixing angles.

When considering the oscillations between ν_e and ν_μ, the mixing matrix becomes

$$\begin{aligned} \begin{pmatrix} \nu_e \\ \nu_\mu \end{pmatrix} &= \begin{pmatrix} U_{e1} & U_{e2} \\ U_{\mu 1} & U_{\mu 2} \end{pmatrix} \begin{pmatrix} \nu_1 \\ \nu_2 \end{pmatrix} \\ &= \begin{pmatrix} cos\theta_{12} & sin\theta_{12} \\ -sin\theta_{12} & cos\theta_{12} \end{pmatrix} \begin{pmatrix} \nu_1 \\ \nu_2 \end{pmatrix} \end{aligned} \tag{1.7}$$

with θ_{12} the mixing angle. The sine and cosine of this angle will from now on be indicated by s and c respectively. The flavour eigenstates can be written as

$$\begin{aligned} |\nu_e\rangle &= c\,|\nu_1\rangle + s\,|\nu_2\rangle \\ |\nu_\mu\rangle &= -s\,|\nu_1\rangle + c\,|\nu_2\rangle \end{aligned} \tag{1.8}$$

When considering a beam of neutrinos, there will be a certain spread on the energy and momentum. This spread can be ignored for now and one can assume all neutrinos to have the same momentum. The result of this approximation will be discussed after the oscillation principle has briefly been introduced.

Due to the different masses, the different mass states will have different energies. Assuming the rest mass is very small compared to the total energy, one can write

$$E_i = \sqrt{p^2 + m_i^2} \approx p + \frac{m_i^2}{2p} \approx p + \frac{m_i^2}{2\bar{E}} \tag{1.9}$$

In this last approximation, the average energy $\bar{E}$ was substituted for the more correct E_i. This can be done since the different energies will be very close to each other, they can not be further apart than the mass of the heaviest state.

One can now look, as an example, at the probability for a neutrino in an electron neutrino beam with energy $\bar{E}$ to become a muon neutrino at time t. The time evolution of an electron neutrino can be written as

$$\begin{aligned} |\nu_e(t)\rangle &= ce^{-iE_1t}|\nu_1(0)\rangle + se^{-iE_2t}|\nu_2(0)\rangle \\ &= \left[c^2e^{-iE_1t} + s^2e^{-iE_2t}\right]|\nu_e(0)\rangle + sc\left[e^{-iE_2t} - e^{-iE_1t}\right]|\nu_\mu(0)\rangle \end{aligned} \tag{1.10}$$

When looking at the probability of finding a muon neutrino, only the muon component remains and the probability is given by

$$\begin{aligned} P(\nu_e \to \nu_\mu, t) &= |\langle\nu_e(t)|\nu_\mu(0)\rangle|^2 \\ &= s^2c^2\left|e^{-iE_2t} - e^{-iE_1t}\right|^2 \\ &= s^2c^2\left|2ie^{\frac{E_1+E_2}{2}t}sin\left(\frac{E_1-E_2}{2}t\right)\right|^2 \end{aligned} \tag{1.11}$$

Now applying Formula 1.9 on 1.11 yields the more simple form

$$P(\nu_e \to \nu_\mu, t) = sin^2\theta_{12}\ sin^2\left(\frac{\Delta m^2}{4\bar{E}}t\right) \tag{1.12}$$

From this equation, the constraint on the mass difference imposed by the mixing angle can clearly be seen. Only the difference between the squared masses is subject to limitations imposed by oscillations. Neutrino oscillations set no constraints on the absolute masses of neutrinos.

Notice that the time t in Formula 1.12 is the *proper time*, the time as experienced by the neutrino. Due to their small mass, neutrinos are already extremely relativistic at very low energies. Stating that neutrinos travel at the speed of light can hardly be distinguished from the truth, the difference is (currently) beyond experimental verification [30, 31]. When converting the time parameter to a distance parameter, using c as neutrino velocity can therefore safely be done. This ultimately leads to

$$P(\nu_e \to \nu_\mu, t) = sin^2\theta_{12}\ sin^2\left(1.27\Delta m^2\frac{L}{E}t\right) \tag{1.13}$$

with E in GeV, L in km and Δm in eV.

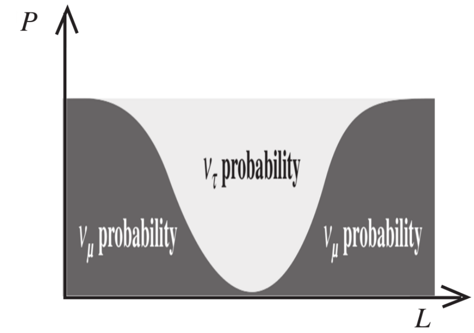

(a) Flavour detection probability in a $\nu_\mu - \nu_\tau$ system with a monochromatic neutrino beam.

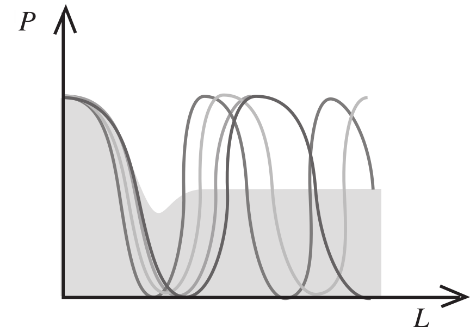

(b) Flavour detection probability of the initial flavour in a two neutrino system with a non-monochromatic neutrino beam.

Figure 1.4: Neutrino oscillations with and without an energy spread

The approximation that all neutrinos in a beam have the same momentum is obviously wrong[12]. The consequences of making this approximation can be seen in Figure 1.4. In 1.4(a), all the neutrinos in the beam have the same energy. It can be seen that the two flavours consistently exchange probabilities, the dominant flavour will depend on the exact distance between the detector and the source. In 1.4(b), no such thing is assumed. The lines depict the flavour detection probabilities for individual neutrinos at different energies. One can see that these probabilities are roughly the same immediately after the creation of the neutrino, but as it gets further from the source, the difference in proper time grows larger for the different energies. As a consequence, the different dominant probabilities will counterbalance each other perfectly after some distance. This results in an equal probability of detecting each type of neutrino if the detector is far enough from the production site.

1.2 Historical Overview

Before neutrinos were ever mentioned, Victor Hess discovered *cosmic radiation* or *cosmic rays* in 1913 [33]. It was known that there is ionizing radiation present in the atmosphere, but the origin was unknown. By using a hot air balloon to measure the ionization on different heights, Hess found an increase in radiation at higher altitude. He correctly concluded that ionizing radiation in the atmosphere must find its origin in outer space[13]. The knowledge about cosmic radiation increased a lot since 1913. It is now known that cosmic radiation is caused by highly energetic

[12] This derivation can be made without this approximation by introducing entanglement with the other particles involved in the production of the neutrinos [32]. Doing that would lead to far and is of no consequence here.

[13] Victor Hess was rewarded the Nobel Prize in 1936, *"for his discovery of cosmic radiation"*.

particles that collide in the atmosphere. In that collision, an *extensive air shower* (EAS) is created. This is a diverting beam of secondary particles travelling in the direction of the initial particle, these are mostly electrons, muons, pions and kaons.

The presence of cosmic radiation has an important effect on neutrino experiments. When a EAS develops, electrons and muons can reach ground level (pions and kaons quickly decay or interact and do not make it to the earth surface). These particles interact via the electromagnetic force, they therefore have a much higher probability to interact with a detector than a neutrino.

In a neutrino experiment that is not shielded from cosmic radiation, the amount of detected neutrino events would be dwarfed by the number of events caused by cosmic radiation. Unless there is a very strict veto from above, the experiment would be useless. Rock is much denser than air and is therefore much better at stopping charged particles. That is why all neutrino detection experiments take place buried deep under the surface, mostly in mines or in tunnels under mountains. Despite all this shielding, some activity from cosmic radiation will always be present. This is because muons have a very small, yet non-zero, chance to penetrate kilometres of rock.

1.2.1 Theoretical predictions

The neutrino was first hypothesised by W. Pauli in 1930 to solve the problem of missing energy in the β-decay spectrum and the unexplained spin of certain nuclei in the proton-electron nuclear model [34]. At that time, the neutron was not yet discovered and the neutrino was initially named neutron. When the neutron was discovered in 1932, the spin problem got solved that same year by describing atoms with protons, neutrons and electrons.

Using this new nuclear model and the hypothesis of Pauli, Fermi theorized that

$$p \to n + e^- + \nu \tag{1.14}$$

describes β-decay in 1934. He also proposed the new name neutrino ('little neutral one' in Italian), which is now still used. Inspired by the Hamiltonian of photon emission from an excited atom $\mathcal{H}^{EM}$, Fermi wrote down a Hamiltonian $\mathcal{H}^{\beta}$ where the proton and nucleon fields couple to the electron and neutrino fields in a point interaction [35]. This interaction has a coupling constant G_F, the Fermi constant.

From $\mathcal{H}^{\beta}$, not only β-decay probabilities can be calculated. Also the cross section for neutrino interactions with nuclei can be calculated. This was done by Bethe and Peierls in the same year Fermi proposed his theory. They found a cross section $\sigma < 10^{-44}$ cm^2, which corresponds with an absorption length in solid matter larger than 10^{14} km [36]. They concluded that *"there is no practically possible way of observing the neutrino"*. Even though present day calculations confirm the early estimations of Bethe and Peierls, neutrinos have been detected [37].

1.2.2 Early experimental observations

In 1956, Cowan and Reines published the results of their reactor experiment in the Savannah River Plant [38]. By using the inverse β-decay process,

$$\bar{\nu}_e + p \to n + e^+ \tag{1.15}$$

they were able to detect about three neutrinos per hour[14]. This was possible by placing two water reservoirs close (at 11 m) to the reactor. The reactor provided a flux of $5 \cdot 10^{13}$ neutrinos per second per square centimetre [39] while the water reservoir provided the protons for the neutrinos to interact with. ^{108}Cd was added in the water to capture the neutrons freed by the neutrino interaction. After neutron capture, ^{109}Cd is in an excited state; it then quickly relaxes by emitting a photon. The water reservoirs were surrounded by liquid scintillator to collect the positron annihilation photons and the Cadmium relaxation photon.

Only two years later, in 1958, Goldhaber, Grodzins and Sunyar measured the helicity of neutrinos with a beautiful experiment [17]. This was done by using a clever chain reaction that finally resulted in a photon being emitted. The polarization of this photons than determines the helicity of the neutrino.

If $^{152}_{63}$Eu captures an electron, it becomes $^{152}_{62}$Sm* and emits a neutrino:

$$^{152}_{63}\mathrm{Eu} + e^- \to\ ^{152}_{62}\mathrm{Sm}^* + \nu_e. \tag{1.16}$$

Since Europium has spin zero, the spin one excited state of Samarium and the neutrino have to be emitted such that their combined spin equals that of the polarized electron. The excited Samarium relaxes to its spinless ground state and emits a photon. If the spin is emitted in the recoil direction, spin conservation demands that the photon and the neutrino have the same helicity. Measuring the polarization of the photons resulted in

$$h_{\nu_e} = -1.0 \pm 0.3. \tag{1.17}$$

This experiment clearly confirmed that electron neutrinos are left handed.

In 1962, Lederman, Schwartz and Steinberger discovered the muon neutrino [40]. This solved a discussion that started early after the discovery of the muon [41] in 1937. People quickly noticed that the decay $\mu \to e + \nu$, which should take place if there is only one neutrino, does not occur. The hypothesis of two neutrinos is then readily made. It was expected that if there were only one type of neutrino, neutrino interactions would produce electrons and muons in equal abundance. If there are two neutrino types, then no electrons should be produced at all when looking at interactions with muon type neutrinos.

This hypothesis was tested at the AGS synchrotron in the Brookhaven National Laboratory. By having a proton beam collide with a Beryllium target, a pion beam is produced. The pions in the beam are given space to decay via

$$\pi \to \mu + \nu. \tag{1.18}$$

[14] Reines received the Nobel Prize in 1995 *"for the detection of the neutrino"*, Cowan died in 1974.

The resulting muons are then stopped in a 13.5 m thick iron shield. What remains behind the shield is a tolerable flux of muons and neutrinos produced in Reaction 1.18. Ledermann, Schwartz and Steinberger measured a total of 113 events. 34 of these events were identified as muon events with an expected background of 5 muons from cosmic radiation. In the one neutrino hypothesis, there should be an equal number of electron events. There were however only 6 electron events. The probability of observing 6 events when 29 events are expected is only $2.1 \cdot 10^{-7}$, thus confirming the existence of a second neutrino flavour, the muon neutrino (ν_μ)[15].

1.2.3 The solar neutrino problem

In 1968, the first experimental indication of neutrino oscillations was seen. The Homestake experiment of Davis was looking for *solar neutrinos* by using inverted β-decay of Chlorine: $^{37}\mathrm{Cl} + \nu_e \rightarrow \ ^{37}\mathrm{Ar} + e^-$, indicated with Cl on Figure 1.5 [42]. Solar neutrinos are neutrinos produced in the core of our sun by nuclear fusion processes. The various nuclear fusion cycles in the sun each produce a certain number of neutrinos per cycle, this can be seen in Figure 1.5. Using various data about the sun and the known cross sections of the nuclear reactions, helioseismologists can make a solar model that predicts the neutrino output of the sun at various energies [43].

In the Homestake experiment, a large tank filled with 390000 liter tetrachloroethylene (good for 520 tons of Chlorine) was placed 1478 m under ground in the Homestake mine (Lead, USA-SD). As is shown in Figure 1.5, this method of detection is predominantly sensitive to neutrinos from Beryllium decay. Periodically, the Argon atoms were counted. This gave the number of neutrino interactions that happened in the tank since the previous Argon-counting. The result of this experiment was that only half of the expected neutrinos was detected, starting the *solar neutrino problem*.

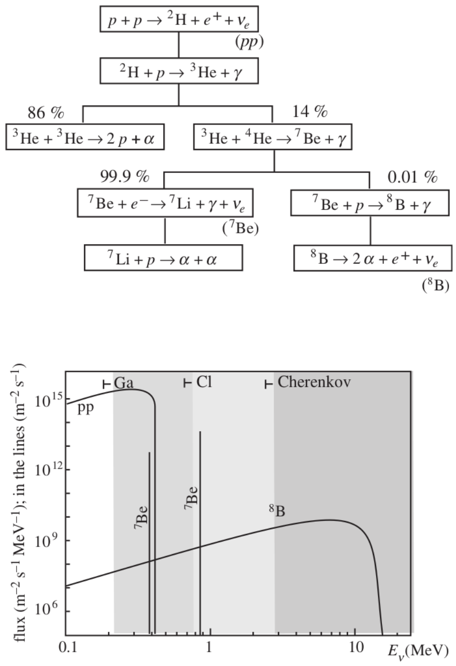

Figure 1.5: The solar standard model [9]. The top figure shows the different fusion cycles in the sun, the bottom figure shows the solar neutrino spectrum and the energy range of three detection methods.

[15]Schwartz, Lederman and Steinberger got awarded the 1988 Nobelprize, "for the neutrino beam method and the demonstration of the doublet structure of the leptons through the discovery of the muon neutrino".

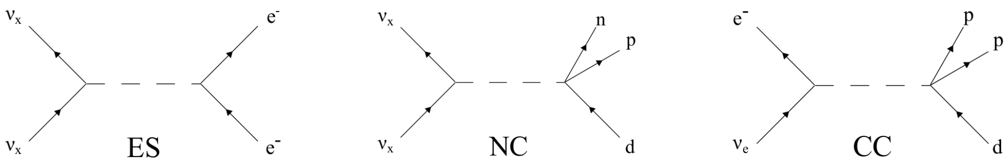

Figure 1.6: SNO neutrino detection reactions

This difference between prediction and measurement had to be explained somehow. Even though theories for neutrino oscillation had been created before this result was published [44, 45], they were not given much attention initially. At that time, neutrinos were considered to be massless and neutrino oscillations should therefore be impossible.

The solar neutrino problem remained an unresolved question for a long time, gathering more mystery over the years. In 1989, the Kamiokande-II experiment in Japan published a measurement of the solar neutrino flux [46]. By using 948 photomultiplier tubes (PMTs) looking at 2140 m^3 of ultra pure water, neutrino interactions could be counted[16]. After conversion of the count rate to neutrino flux, the measured value was about half the expected flux. This result confirmed the problem, but gave no solution.

However, there had come an indication of massive neutrinos in 1987, such that neutrino oscillations suddenly became possible. On February 24, Kamiokande-II detected eleven neutrinos from Supernova 1987A. The eight first neutrinos arrived within two seconds from each other, the remaining three arrived 9.2, 10.4 and 12.4 seconds after the first neutrino. Since detecting three neutrinos in 3.2 seconds is extremely unlikely, they were assigned to the supernova, making the event last 12.4 s. Astrophysical models predicted that all neutrinos should have been emitted in a time window of maximum four seconds. If neutrinos were massless, they would travel at the same speed and arrive within the time range in which they were produced. Due to this discrepancy between the detected and predicted time spread, it was concluded that neutrinos are massive [47]. Also from this time spread, it was concluded that neutrinos must have an upper mass limit of 12 eV.

Now that neutrino oscillations were theoretically possible, dedicated detectors were built to find or exclude oscillation; one of these detectors was the Sudbury Neutrino Observatory (SNO). Like the Kamiokande experiment, SNO used the Cherenkov technique to detect neutrinos. It was made of a 12 m diameter spherical vessel surrounded with 9456 PMTs. Unlike the Kamiokande-II detector, the SNO volume was filled with heavy water (D_2O). This made it possible for the SNO detector to observe reactions that could not be seen by Kamiokande-II. In this experiment, Deuterium is needed to detect charged current (CC) and neutral current

[16]This is the Cherenkov technique that is also used in the IceCube Neutrino Observatory. This technique will be explained in Section 2.1.

(NC) interactions, this can be seen in Figure 1.6.

Even though the Kamiokande-II was sensitive to elastic scattering (ES), which is possible with all three neutrino flavours, it can not be used to measure neutrino oscillations because the result of an ES event is always an electron being accelerated. There is simply no way to learn the flavour of the neutrino that interacted with the electron. Since SNO had the other interaction types to compare with, they could assign a fraction of the neutrinos they detected to each flavour. After 306.4 days of taking data, SNO reported an electron and a non-electron solar neutrino flux, respectively Φ_e and $\Phi_{\mu\tau}$ (in units $10^6\ cm^{-2}s^{-1}$):

$$\begin{aligned} \Phi_e &= 1.76^{+0.05}_{-0.05}\,(stat.)^{+0.09}_{-0.09}\,(syst.) \\ \Phi_{\mu\tau} &= 3.41^{+0.45}_{-0.45}\,(stat.)^{+0.48}_{-0.45}\,(syst.) \end{aligned} \tag{1.19}$$

Since the sun produced only electron neutrinos, $\Phi_{\mu\tau}$ should be zero if there are no neutrino oscillations. This 5.3 σ deviation from zero concludes that there are neutrino oscillations and solves the solar neutrino problem[17] [19].

The results of SNO could also explain the results of the previously mentioned experiments. The Homestake experiment was only sensitive to electron neutrino interactions. If one looks at Equation 1.19, one can see that Φ_e is about one third of the total flux. The Kamiokande-II experiment used ES interactions, which is sensitive to all neutrino flavours. However, an electron neutrino can also interact with an electron via a CC process. The CC and ES interactions have the same initial and final states. This makes Kamiokande-II roughly double sensitive to electron neutrinos. Using this information and the cross sections for the different processes leads to half the expected flux, roughly one third from electron neutrinos and about one sixth from other flavours.

1.2.4 Neutrino physics at particle accelerators

While the solar neutrino problem was being discussed and solved with dedicated neutrino experiments, it was business as usual for particle accelerators. Even though these experiments were not dedicated to neutrino physics, they found some interesting properties as well. In 1976, the linear electron-positron collider in Stanford (SLAC) discovered the tau lepton (τ)[18] [48]. After some analyses, it became clear that the τ had its own neutrino, ν_τ [49].

Even though it was clear from the work of Perl that the tau lepton had its own neutrino, it took a long time to detect the first ν_τ. Before that first detection in

[17] This discovery of the SNO collaboration was a confirmation of the work done by the Homestake and Kamiokande-II experiments. Their leaders, respectively Davis and Koshiba, received the Nobel prize, *"for pioneering contributions to astrophysics, in particular for the detection of cosmic neutrinos"*

[18] Perl, the leading author of the paper that claimed discovery, received the Nobel prize in 1995, *"for the discovery of the tau lepton"*.

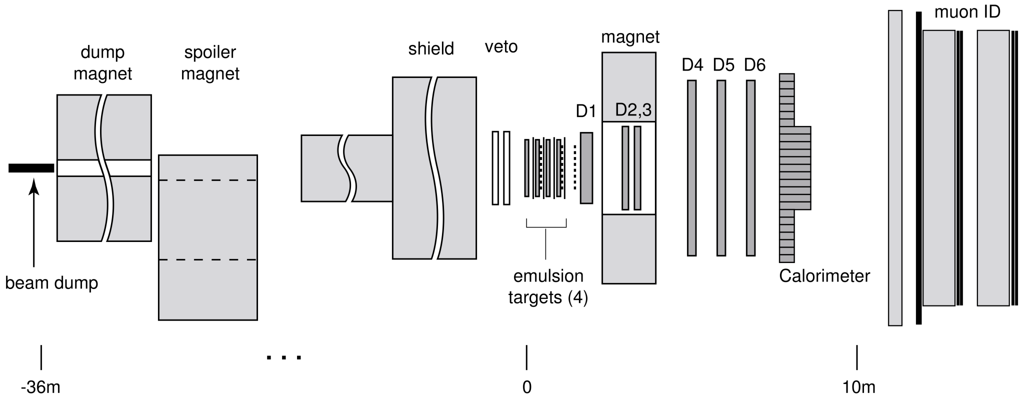

Figure 1.7: The DONUT experiment, the proton beam enters from the left.

2000, another experiment already indicated the existence of the tau neutrino in 1989, using the LEP-collider[19].

When comparing the total decay width of the Z-boson to the sum of the individual decay widths into lepton anti-lepton pairs, one finds an excessive value for the total decay width. This is because the Z-boson also decays to neutrino anti-neutrino pairs. The missing decay width comes from decay to neutrinos. From the standard model, the decay width to a single neutrino flavour can be calculated. Fitting the experimental data to the Standard Model with an undetermined number of neutrino flavours yielded $3.27 \pm 0.24_{stat.} \pm 0.16_{syst.} \pm 0.05_{theo.}$ different neutrino flavours in the accessible energy range of the LEP-collider [50]. The lower mass limit of a fourth neutrino flavour was 30 GeV in 1989, more recent values can be found in *Review of Particle Physics* [6].

Detection of the first tau neutrino

It took until 2000 to detect the first tau neutrinos [51], this was done by the DONUT[20] collaboration at Fermilab. To this day, only a handful of neutrino interaction events have been confirmed to originate from tau neutrinos. The DONUT-collaboration only saw four tau neutrinos in half a year. The expected number of interactions without tau neutrino was 0.32 ± 0.05, so the four neutrinos they saw were more than enough to claim observation.

The experimental setup of the DONUT experiment can be seen in Figure 1.7. When a proton bundle has reached the end of its useful life in a collider, it is dumped in a *beam dump*. This is simply a beamline leading into a block of material with a high melting point. The high melting point is needed to absorb all the kinetic energy of the particles without melting, the beam dump of the LHC has to be able to absorb

[19]Large Electron Positron collider, CERNs collider before the LHC was commissioned.
[20]Direct Observation of NU Tau

362 MJ of beam energy in 90 μs, which comes down to 4 TW. This is roughly the energy produced by all nuclear power plants worldwide in one hour. In the case of Tevatron, the accelerator at Fermilab, this beam dump was made of Tungsten (melting point of 3695 K). In it, the dumped protons interact with protons and neutrons of the Tungsten nuclei. The interactions of interest are those that produce D_S-mesons. The branching fraction of $D_S \to \tau\nu_\tau$ is 5.43%. From this number, it is clear that the majority of interaction do not produce τ neutrinos. Even worse, a lot of interactions produce muon or electron neutrinos.

The charged particles produced in the reactions are easily taken care of. The detector is placed 36 m behind the beam dump. In between, shielding was provided by slabs of concrete, iron and lead. On top of that, magnetic fields were present to deflect charged particles away from the detector. A scintillation counter veto wall was placed in front of the actual detector. Charged particles that reached the detector in spite of all the shielding registered in the scintillation counter and could be rejected in that way.

Neutrinos that interacted in the detector, an emulsion-scintillation hybrid, are not as easily separated by flavour. Neutrino events start in the middle of the detector; at the point of interaction, the corresponding lepton is created. Here, the different behaviour of the different lepton flavours has to be used to assign a flavour to each event. Electrons rapidly lose energy by interaction with atomic electrons or nuclei (Bremsstrahlung), this results in a path filled with interactions. Muons are heavier than electrons, they therefore interact less than electrons. Despite the fact that they are not stable, they have a long enough lifetime to leave the detector.

An interaction with a tau neutrino resulted in a charged tau lepton. This is a very unstable particle, it has a half life of only 0.29 ns. With the typical neutrino energies of the experiment, the tau would decay after about 2 mm path length. It then produces one (86%) or multiple (14%) charged particles. Decays into one charged particle result in a single track with a kink after ± 2 mm, indicating the emission of at least one neutrino with large transverse momentum. Decay into multiple charged particles is always hadronic. These decay products interact heavily with the detector medium and potentially overflow the original tau-track. Therefore, events with multiple tracks are ignored.

For tau neutrino events where the tau lepton decays into a single charge particle, the properties of that particle have to be measured. This is done by the detectors downstream the emulsion targets (right on Figure 1.7). The momentum of the particle is measured by the deviation of the path induced by the magnet that surrounds detectors D2 and D3. If the leaving particle is a hadron (56.6%), its energy is measured by the calorimeter. In case of decay to a muon (20.6%), it is identified by the muon detector on the far right of Figure 1.7. Electrons (22.8%) seldom reach D1 before they are stopped. Their energy is estimated from the energy loss in the emulsion detector.

From the approximately $3.54 \cdot 10^{17}$ protons that got dumped into the Tungsten target, 203 resulted in a neutrino event with satisfying accuracy to be able to measure the place and angle of the kink. From these events, 97 were identified as muon neutrinos and 61 from electron neutrinos. For the remaining events, a number of selection criteria based on computer learning from simulated datasets were applied. Four events passed these criteria. These four events are unambiguously accepted as the four first tau neutrinos ever detected.

This section gives only a quick overview of what happened in neutrino physics. The number of Nobel prizes awarded for discoveries related to neutrinos shows that this is not an insignificant field. Next to those landmark experiments, a lot of other experiments did not get mentioned. After the publication of a Nobel prize winning paper, the results have to be confirmed by an independent collaboration and parameters often are to be measured more accurately. Experiments that do those things are often not mentioned, that does not mean their results are of any less value. They simply were not first. This paragraph is for those experiments, to indicate their contribution to the scientific knowledge.

1.3 Messengers from outer space[21]

As mentioned before, the earth is constantly being bombarded with particles from outer space. These are mostly protons (86%) and alpha particles (11%), but also heavier nuclei (1%) and electrons (2%). Cosmic rays are considered to consist of these initial particles plus the secondary particles they create as they traverse the atmosphere [52]. Neutrinos are typically not included in this definition. This makes sense from a historical point of view. Cosmic rays were used as a particle source in the discovery of the positron in 1932 [53] while two years later, Bethe and Peierls stated that it would be impossible to ever detect a neutrino. The historical importance attached to detection in the atmosphere is the second reason why neutrinos don't show up in traditional definitions of cosmic rays. Because of their low cross section, they hardly ever interact in the atmosphere.

Even though neutrinos are somewhat left out when it comes to cosmic rays, they must have the same origin. Unlike the other particles that make up the primary particles of cosmic rays, neutrinos can be produced in the nuclear fusion processes in the center of stars. This however can not be their only source, these processes produce neutrinos with a maximal energy of about 10 MeV. This is eight orders of magnitude lower than the highest energy neutrinos observed so far [54]. Because neutrinos have no electrical charge, they can not be accelerated once they are created. An independent acceleration mechanism is thus needed to first accelerate charged particles to high energies, after which neutrinos can be created via interaction of the accelerated charged particle.

Acceleration to the highest energies can not take place at ordinary events such

[21] Particles in cosmic rays are often called "messengers from outer space". This romantic name is given to them because they can help us explain the physics that is behind some of the most violent effects in the universe.

as main sequence stars, we would be swamped by high energy radiation from our own sun otherwise[22]. One has to look at more extreme events such as supernovae, binaries, active galactic nuclei (AGNs) or gamma ray bursts (GRBs) as a source of cosmic rays. Supernovae occur when a heavy star has burned through its supply of Hydrogen. As a consequence, a chain reaction takes place. This ultimately leads to the explosion of the star. An AGN is a super massive black hole in the centre of a galaxy that "eats" stars in its environment. The star that gets eaten is gradually ripped apart and plasma gets ejected into space. A binary has the same working principles but uses a neutron star instead of a black hole. The working mechanism of a GRB is not yet known.

1.3.1 Acceleration of cosmic rays

In both supernovae and AGNs, matter gets ejected from the star in shocks. These shocks are density waves that propagate through the interstellar medium at significant fractions of the speed of light. These shocks allow particles to get accelerated with *shock acceleration*. This method was proposed by Fermi in 1949 [55].

When a shock propagates with a velocity u_1, the gas behind the shock moves in the opposite direction with a velocity u_2 (see Figure 1.8). If a particle with velocity v has a head-on collision with the shock and gets reflected, it has an energy gain ΔE.

$$\begin{aligned} \Delta E &= \frac{1}{2} m \left(v + (u_1 - u_2)\right)^2 - \frac{1}{2} m \left(v\right)^2 \\ &= \frac{1}{2} m \left(2v\left(u_1 - u_2\right) + \left(u_1 - u_2\right)^2\right) \end{aligned} \tag{1.20}$$

As the particle velocity is much larger than the shock velocity, the part of this energy gain that is linear in the shock velocity dominates over the quadratic part. The energy gain can thus be approximated by

$$\frac{\Delta E}{E} \approx 2 \frac{u_1 - u_2}{v} \tag{1.21}$$

This mechanism can not explain the very high energies seen in cosmic rays. However, in supernovae, several layers of material are often being ejected quickly after each other, forming several successive shock fronts. In this situation, particles can be trapped between two successive layers and get reflected back and forth between those layers. When this happens, the outer shock front usually has a lower velocity (v_1) than the inner shock front (v_2) as the outer wave has been slowed down by interactions with the interstellar medium.

When a particle gets reflected on the inner shock front, it has a head on collision and gains an amount of energy $\Delta E = \Delta E_2$. When the particle gets reflected on the

[22]Main sequence stars can accelerate charged particles using sunspots, but this mechanism has a maximum energy of the order GeV [10]. This is six orders of magnitude lower that the energies considered in this thesis.

outer shock front, it has to overtake the shock and will lose energy (ΔE_1).

$$\begin{aligned} \Delta E_1 &= \frac{1}{2} m \left(v - v_1\right)^2 - \frac{1}{2} m v^2 \\ \Delta E_2 &= \frac{1}{2} m \left(v + v_2\right)^2 - \frac{1}{2} m v^2 \end{aligned} \tag{1.22}$$

Because the outer shock front is slower, a particle gains energy when it makes a full cycle:

$$\Delta E = \Delta E_1 + \Delta E_2 = \frac{1}{2} m \left(v_1^2 + v_2^2 + 2v \left(v_2 - v_1\right)\right) \tag{1.23}$$

The terms quadratic in the shock velocities can again be neglected. This leads to

$$\frac{\Delta E}{E} \approx 2 \frac{\Delta v}{v} \tag{1.24}$$

with Δv the velocity difference between the inner and the outer shock front [10].

The derivation of the energy gain of a charged particle trapped between two shock fronts presented above is a simplistic one. A few remarks have to be made before its result can be used in further derivations. First, the particle velocity will quickly converge to c, so that Formula 1.24 loses a variable and becomes more gentle. Second, the medium in between the two shock fronts is not vacuum, the particle will lose energy to scattering between the two shock fronts. This will reduce the energy gained per cycle. One can however still conclude that

$$\frac{\Delta E}{E} \sim \frac{\Delta v}{c} \tag{1.25}$$

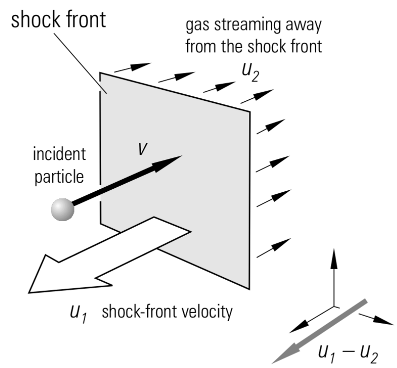

Figure 1.8: Schematics of shock acceleration

This can be rewritten as $\Delta E = \alpha E$, where α contains both the velocity difference between the shocks and the effects of scattering in between the shocks.

When a particle gets injected in the shock front system with an energy E_0, it will have an energy $\left(1 + \alpha\right) E_0$ after one full cycle. After n cycles, its energy will become $\left(1 + \alpha\right)^n E_0$. The number of circulations needed to reach the final energy can be calculated:

$$n = \frac{ln \left(E/E_0\right)}{ln \left(1 + \alpha\right)} \tag{1.26}$$

It is however always possible for the particle to escape the system. If P is the probability for a particle to stay in the system for further acceleration, the number of particles after n cycles will be given by

$$N = N_0 P^n \tag{1.27}$$

Combination of Equation 1.26 and Equation 1.27 yields

$$ln\frac{N}{N_0} = n\ lnP = ln\left(E/E_0\right)\frac{lnP}{ln\left(1+\alpha\right)} = ln\left[\left(\frac{E_0}{E}\right)^s\right] \tag{1.28}$$

In this equation, N is the number of particles that completed n cycles or more in the system. These particles will have an energy higher than E. The differential energy spectrum will have the power law dependence

$$\frac{dN\left(E\right)}{dE} = const.\left(\frac{E}{E_0}\right)^{-(1+s)} \tag{1.29}$$

A more involved treatment of the physics and mathematics in the derivation of this power law spectrum yields $s \approx 1.1$ so that the differential spectrum index is -2.1. The experimentally observed value for the differential energy spectrum of cosmic rays is -2.7. The steeper observed spectrum can be due to an increased escape probability $(1 - P)$ with higher energy. Experimental data seem to confirm this theory [52].

Shock wave acceleration in supernovae is able to accelerate charged particles up to about $100z$ TeV, where z is the electrical charge of the accelerated particle. For protons, $z = 1$; for e.g. Iron nuclei, $z = 26$. Almost no particles with an energy higher than that will come from supernovae. Cosmic ray experiments however see particles with energies that exceed this value by several orders of magnitude, these particles must come from another source[23]. Candidates for this high energy accelerator are AGNs and binaries. These events also eject matter in shock fronts, but combine it with large electric and magnetic fields from plasma clouds [10]. This allows them to accelerate particles to much higher energies.

1.3.2 Astrophysical neutrinos

As mentioned before, neutrinos can not be accelerated. They have to be created with all their energy at once. *Astrophysical neutrinos*, meaning neutrinos that have not been created on Earth, are produced over a broad energy range and come from a large variety of sources. An overview of the astrophysical neutrino spectrum can be seen in Figure 1.9.

Low energy astrophysical neutrinos

The Cosmic Neutrino Background (CνB) is a remnant of the Big Bang. Detection of these neutrinos is currently not within experimental reach, although there are propositions to measure this flux [58]. This spectrum is expected to be an isotropic blackbody spectrum with a temperature of 1.9 K.

[23]The experimental confirmation of supernovae as a source for hadronic cosmic rays was published last year [56].

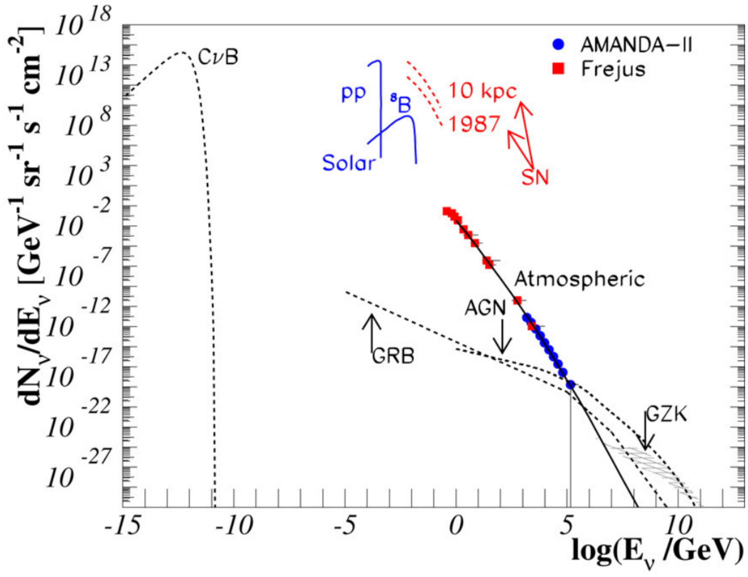

Figure 1.9: Astrophysical neutrino spectrum; predicted fluxes are in dashed lines, measured fluxes are in solid lines [57]

The solar neutrino flux (~ 1 MeV) was already treated in Section 1.2.3. One can see here that the neutrino flux from the sun is much higher than that of any other source.

At slightly higher energies (~ 10 MeV), one can find neutrinos from supernovae. Neutrinos from supernovae are emitted only briefly, the flux is therefore dependent on the distance from the supernova to the earth. On Figure 1.9, the expected flux for a supernova at 10 kpc is depicted and also the flux for the supernova detected in 1987. Even though neutrinos from that supernova have been detected, its spectrum is shown in dashed lines because no spectrum measurement was performed.

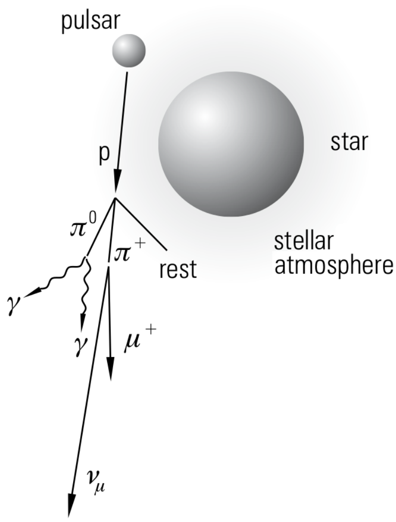

Figure 1.10: Production mechanism of high-energy neutrinos in a binary system [10]

Atmospheric neutrinos

Atmospheric neutrinos are neutrinos produced by interaction of cosmic rays with nuclei in the atmosphere. Technically, these neutrinos have been created on earth. They do not fit the definition of astrophysical neutrinos and are therefore often considered a background in experiments that look for astrophysical neutrinos. They do however have the same energy range as neutrinos from astrophysical sources and are therefore considered here.

In the proton-air interactions, predominantly pions are produced. The decay of charged pions (26 ns lifetime) produces muon neutrinos.

$$\pi^+ \to \mu^+ + \nu_\mu, \qquad \pi^- \to \mu^- + \bar{\nu}_\mu \tag{1.30}$$

Muons themselves are unstable as well, but with their high energy and long lifetime (2.2 μs), they often reach the earth before they decay. When they decay, each muon produces two neutrinos.

$$\mu^+ \to e^+ + \nu_e + \bar{\nu}_\mu, \qquad \mu^- \to e^- + \bar{\nu}_e + \nu_\mu \tag{1.31}$$

One can see that three neutrinos are produced for every charged pion produced in the interaction of the primary particle with the atmosphere. These three neutrino are two muon neutrinos and one electron neutrino, so that the flavour rate of atmospheric neutrinos, $\nu_e : \nu_\mu : \nu_\tau$, is $1:2:0$. The atmospheric neutrino spectrum therefore follows the spectrum of the incident cosmic rays, but with a higher flux. The spectrum also has a lower energy than the cosmic ray spectrum as the total energy is conserved [10].

High energy astrophysical neutrinos

Also indicated on Figure 1.9 are the expected spectra for GRBs, for AGNs and binaries and for GZK neutrinos. GRBs, AGNs and binaries are cosmic accelerators that accelerate charged particles roughly following the principles explained in Section 1.3.1. If a charged particle escapes from its acceleration cycle, it still has to plough through the stellar atmosphere. If an interaction takes place, mainly pions are produced. Decay of charged pions yields neutrinos (Equation 1.30) whereas decay of neutral pions ($8.4 \cdot 10^{-17}$ s lifetime) yields two photons. This process is indicated in Figure 1.10. Depending on the density of the stellar atmosphere, these photons might be reabsorbed so that the binary or AGN is not visible with photons.

Since the production of neutrinos in binaries and AGNs follows the same elementary reactions as those in the production of atmospheric neutrinos, astrophysical neutrinos will be produced with the same $1:2:0$ flavour ratio as atmospheric neutrinos. However, due to the energy distribution of the astrophysical neutrinos and the very long distances they have to travel to reach the earth, the flavour ratio upon arrival is expected to be $1:1:1$. The distance travelled by atmospheric neutrinos is insufficient to have a significant probability for oscillation to a tau neutrino. If a high energy tau neutrino would be detected, it is undoubtedly an astrophysical neutrino. This is one of the design goals of the IceCube Neutrino Observatory[24] [59].

[24]Chapter 2 is dedicated to the IceCube Neutrino Observatory.

Even though the IceCube Neutrino Observatory already detected 28 neutrinos of astrophysical origin [54], for which the collaboration was awarded the "2013 Breakthrough of the Year" by *Physics World*, detection of tau neutrinos remains relevant. A measurement of tau neutrinos can lead to a better understanding of cosmic accelerators and a more precise measurement of oscillation parameters.

The GZK spectrum comes from the predicted interaction of extremely high-energy protons with the photons of the cosmic microwave background (CMB)[25], this interaction takes place for a proton energy of $5 \cdot 10^{19}$ eV and higher. The possible interactions are

$$\begin{aligned} \gamma_{CMB} + p \to \Delta^+ \to p + \pi^0 \\ \gamma_{CMB} + p \to \Delta^+ \to n + \pi^+ \end{aligned} \tag{1.32}$$

The subsequent decay of the pion then produces either two photons or a muon and a muon neutrino [60, 61].

[25] Similar to the CνB, CMB is also a remnant of the Big Bang.

Chapter 2

The IceCube Neutrino Observatory

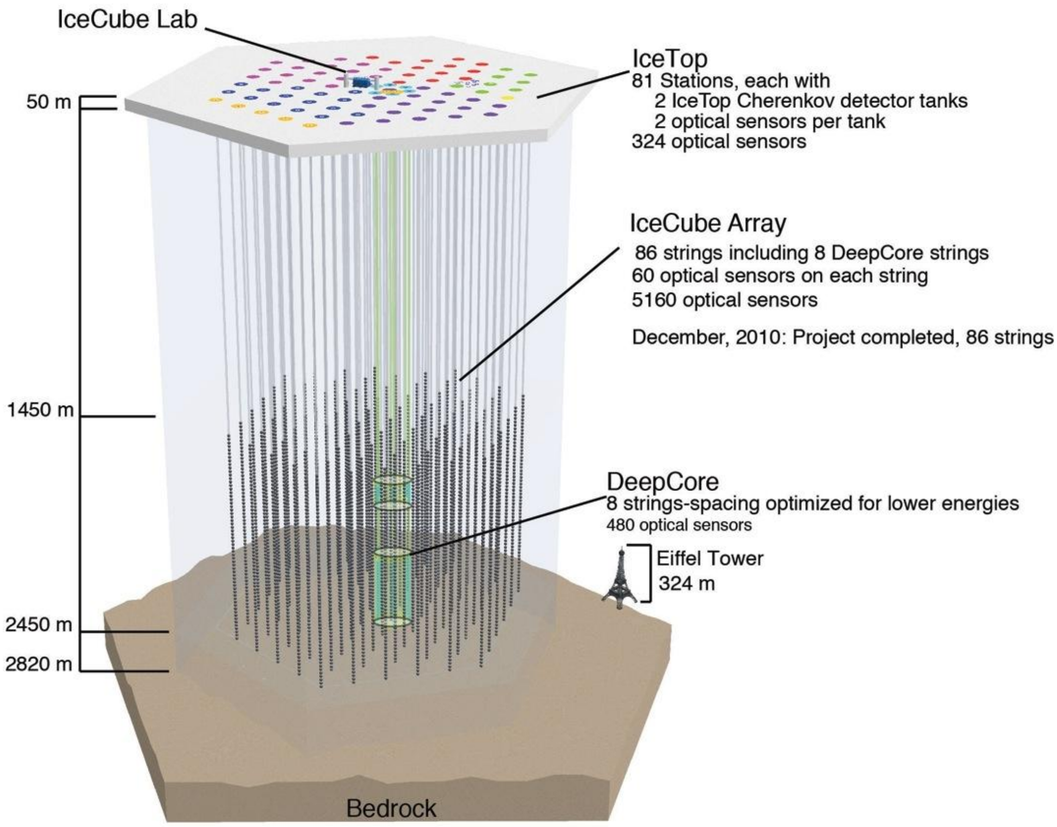

Figure 2.1: The IceCube Neutrino Observatory with all its components. The different colours of the IceTop stations indicate the year of deployment.

The IceCube Neutrino Observatory, depicted in Figure 2.1, is a physics experiment constructed on and in the Antarctic ice, near the Amundsen-Scott South Pole Station at the geographical South Pole. It consists of two main components: IceCube in the ice to detect neutrinos and IceTop on top of the ice to detect EASs. Both components make use of the same Digital Optical Modules (DOMs) to detect their respective targets.

2.1 Detection principle

The speed of light in vacuum, $c = 299792458$ m/s, is the absolute speed limit in the universe. When light travels through a medium however, its phase velocity c_n is a factor n lower than that in vacuum.

$$c_n = \frac{c}{n} \tag{2.1}$$

where n is the refractive index of the medium.

Charged particles that travel through a medium with a velocity higher than the phase velocity in that medium will emit so called Cherenkov radiation. This radiation is the optical analogue of the bang created by a supersonic aircraft. Similar to a supersonic aircraft, the created optical shock front has a cone shape trailing behind the particle. This is illustrated in Figure 2.2. The opening angle θ_c of the cone is determined by the particle velocity v:

$$cos\left(\theta_c\right) = \frac{c_n}{v}. \tag{2.2}$$

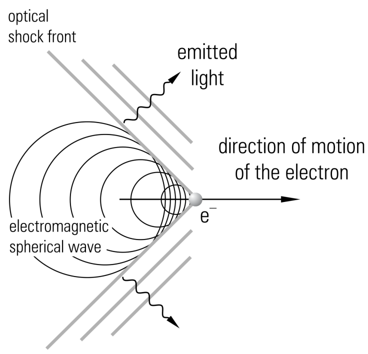

Figure 2.2: Cherenkov radiation by an electron

The number of Cherenkov photons emitted per unit track length and per wavelength is given by the Frank-Tamm formula:

$$\frac{d^2N}{dx\ d\lambda} = \frac{2\pi\alpha z^2}{\lambda^2}\left(1 - \frac{c^2}{v^2 n^2\left(\lambda\right)}\right), \tag{2.3}$$

with z the charge of the particle and α the fine structure constant [62].

Equation 2.3 shows Cherenkov radiation is not emitted at one single wavelength. Emission mainly happens in the blue and ultraviolet wavelengths. This can be seen in the typical blueish glow in the reactor pool of nuclear power plants. Equation 2.3 also shows that the emitted spectrum depends on the particle velocity. For very high energies[1], the velocity of a particle is for all practical purposes the speed of light

[1] A particle reaches 99% of the speed of light once its kinetic energy exceeds six times its rest energy.

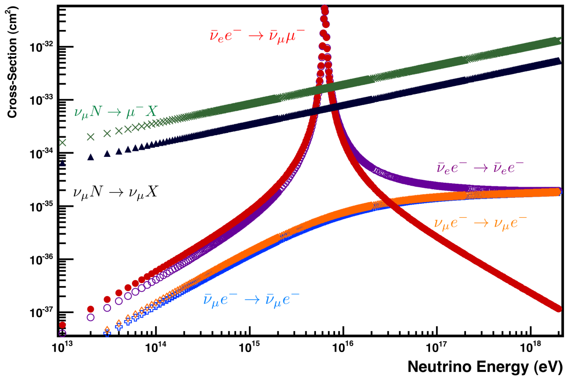

Figure 2.3: Neutrino electron and nucleon scattering in the ultra high energy regime $\left(E_\nu > 10^4 \text{ GeV}\right)$. Shown are the electron interactions $\bar{\nu}_\mu e^- \to \bar{\nu}_\mu e^-$ (crosses, blue), $\nu_\mu e^- \to \nu_\mu e^-$ (diamonds, orange), $\bar{\nu}_e e^- \to \bar{\nu}_e e^-$ (hollow circles, violet), $\bar{\nu}_e e^- \to \bar{\nu}_\mu e^-$ (filled circles, red), and the nucleon charged current (cross markers, green) and neutral current (filles triangles, black) interactions. The leptonic W resonance channel (Glashow resonance) is evident [64].

in vacuum. Therefore, the Cherenkov spectrum mainly depends on the refractive index. For ice, the refractive index gently decreases with increasing wavelength.

Next to Cherenkov radiation, charged particles that propagate through material also lose energy via excitation or ionization of the surrounding material and Bremsstrahlung. These processes result in an additional light production. Bremsstrahlung and excitation-ionization produce light directly, freed electrons and positrons emit Cherenkov radiation as they propagate through the ice [63].

Detection of neutrinos

Neutrinos are electrically neutral. They do not emit Cherenkov radiation or Bremsstrahlung, they also do not ionize the surrounding material. This raises the question about how neutrinos get detected. Actually, the answer is “They don’t.”, only neutrino interactions in which charged particles are produced can be detected. Neutrinos can interact either with electrons or with nucleons. In both cases, interaction can happen via charged current or neutral current. The cross sections for the various interactions are depicted in Figure 2.3.

Not all possible neutrino interactions are shown for every flavour in Figure 2.3. One can however extrapolate the cross sections of the presented interactions to all flavours. For neutrino-nucleon interactions, all flavours are equal. Electron and tau neutrinos therefore follow the line that is depicted for muon neutrinos. When it comes to neutrino-electron interaction, two flavours are already present. Tau neutrino interactions will follow muon neutrino interactions. The neutral current is the same for all three flavours, but $e\nu_e$ interactions are also possible via the charged current.

From Figure 2.3, it is clear that neutrinos will interact with nucleons in the vast majority of the cases. Except for the leptonic W resonance at 6.3 PeV, the neutrino-electron cross section is always several orders of magnitude smaller than than the neutrino-nucleon cross section. This effect is due to the smaller target mass in neutrino-electron interactions [64].

This behaviour also explains how neutrino interactions get detected. At the very high energies that are considered here, neutrinos interact with the individual quarks in the nucleon. This process, called deep inelastic scattering (DIS), takes place via both charged and neutral current.

In the case of a neutral current interaction, the initial and final particles are the same. A Z boson gets exchanged between the quark and the neutrino and results in a simple transfer of energy and momentum from the neutrino to the quark. If enough energy is transferred, the quark gets ejected from the nucleon and hadronization takes place. It is the resulting shower of charged particles that gets detected. These particles are super luminous and emit Cherenkov light. They also heavily ionize the surrounding ice, freeing electrons that produce light as well. This hadronization-ionization process gives rise to a lot of light produced very locally. As the light propagates through the ice, it forms an expanding sphere, called a *cascade*.

In a charged current interaction, the initial and final particles are not the same. Also not every neutrino can interact with all quarks. Charge conservation requires neutrinos to interact with down-type quarks (d,s,b) and antineutrinos with up-type quarks (u,c,t). The result of a charged current interaction of a neutrino with a quark is production of the associated lepton and a highly energetic quark of a different type in the nucleon. Like the neutral current case, hadronization will take place and a cascade will develop. However, also the charged lepton will interact in the ice. The different neutrino signals this gives rise to will be discussed in Section 2.6.

2.2 Digital Optical Modules

The IceCube Neutrino Observatory has a total of 5484 DOMs, 5160 in IceCube and 324 in IceTop. The IceCube DOMs are suspended from the surface along a string, the IceTop DOMs are placed in tanks on the surface. Every tank contains two DOMs and two tanks are placed on top of every IceCube string. These DOMs are used to detect light emitted by charged particles travelling through the ice.

The IceCube DOMs are deployed between 1450 m and 2450 m below the ice surface, they have to be able to withstand enormous pressures. Therefore, all parts are placed in a 13 mm thick, 35.6 cm diameter glass sphere, with a single connection to the outside world (Penetrator in Figure 2.4a). The most important component of a DOM is the 25 cm R7081-02 Hamamatsu photomultiplier tube (PMT). The PMT is the eye of the detector, it captures the photons that fall on it and gives an electrical signal out at the end of the tube [65]. Another vital part of the DOM is the mainboard. On it are the hardware units that read and digitize the PMT output

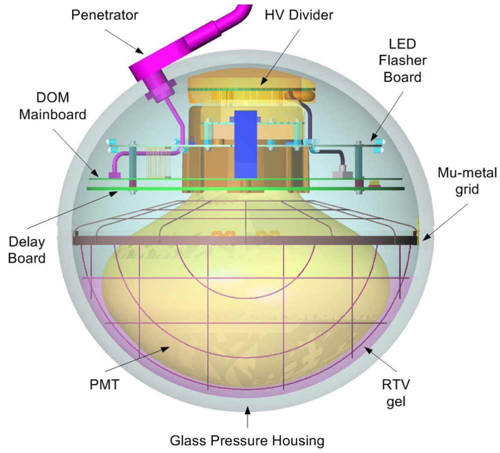

(a) Schematic representation of the DOM hardware components [65]

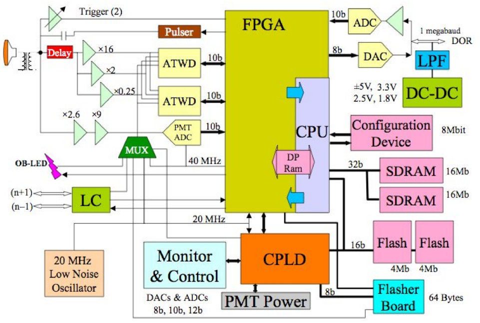

(b) Block diagram of a DOM main board [66]

Figure 2.4: Schematic view of a Digital Optical Module

and also communication systems that send the collected information to the surface. Other components of a DOM are: a mu-metal grid to shield the PMT from the Earth magnetic field, an optical gel to couple the PMT to the glass sphere (RTV[2] gel in Figure 2.4a), LED flashers used in IceCube to calibrate the detector and a high voltage divider to provide the PMT with the voltage it needs.

Figure 2.4b schematically shows a DOM mainboard and its connection to the PMT and outside world. The lines on the figure show how all components work together. The red box indicated with “Delay” is not on the mainboard, it has an individual board that can be seen on Figure 2.4a. On it is a conductive line that guides the signal multiple times around the central aperture, making sure that the signal leaves 75 ns after it was brought on the Delay Board [67].

The PMT is indicated on the left of Figure 2.4b, it is operated with the photocathode grounded. The anode signal formation hence occurs at positive high voltage. To pass the pulse information from the anode to the main board and delay board at ground potential, the anode has to be capacitively coupled. This capacitor is also indicated.

On the mainboard, there are three waveform digitizers. Two purpose designed Analogue Transient Waveform Digitizers (ATWDs) for high precision readout and a less accurate Fast Analog to Digital Converter (FADC). The ATWDs have a limited memory and can each store only 400 ns of information (128 bins of 3.125 ns), after which they take 29 μs to digitize the waveform. To avoid dead time, two ATWDs are placed on every mainboard. The FADC is present because some events take longer than 400 ns. Even though the FADC can digitize arbitrary long pulses, it is chosen to make it digitize 6.4 μs (36 bins of 180 ns). The digitizers are controlled

[2]room temperature vulcanizing

and read out by a field-programmable gate array (FPGA). The FPGA in turn is controlled by the trigger logic. The FPGA builds the hits, compresses the data and passes it on to the CPU. The CPU then sends the data to the surface.

The analogue output of the PMT is split into three streams, one stream goes first through the delay board and then into the ATWDs, another stream is fed to a discriminator trigger and the last stream is fed to the FADC. If the trigger condition is met, the FPGA activates an ATWD and FADC digitization procedure. For the first 400 ns, the FADC output is ignored[3] in favour of the more precise ATWD.

On Figure 2.4b, both ATWDs have three input channels. Each of these channels has a different amplifier in front of the input. When an ATWD is read out, the channel with highest multiplication (x16 multiplier), *channel 0*, is read out first. If one of the bins in this channel exceeds the threshold of 768 counts, the ATWD discards this sample and starts over with channel 1 (x2 multiplier). The same reasoning goes for switching from channel 1 to channel 2 (x0.25 multiplier).

The trigger consists of two steps. The first requirement is met when one sixth of the expected pulse height for a single photo electron (SPE) is received. At that moment, the FADC starts integrating the total collected charge and the trigger time is kept. At the same time, a signal of local coincidence (LC) is sent to the two neighbouring DOMs. If the sending DOM also receives a LC signal within 1 μs from one of its neighbouring DOMs, it starts an ATWD and/or FADC cycle.

If a DOM receives a LC signal but has not triggered itself yet, it simply passes the LC signal along. If that DOM then exceeds the detection threshold within 1 μs of receiving the LC signal, it immediately starts an ATWD and/or FADC cycle. It then also sends a LC signal as a reply to received signal. DOMs that have send a LC signal and received a reply do not pass on that reply as they send the original signal.

LC signals are passed along dedicated wires that connect the individual DOMs. Every DOM, except for the upper and lower DOMs, is in this way connected with his neighbour above and below him. These LC wires are not to be confused with the main wire that supplies the DOMs with power and allows communication with the surface.

2.3 IceCube

IceCube is the part of the IceCube Neutrino Observatory that is inside the ice. It can be seen on Figure 2.1, indicated with “IceCube array”. A cubic kilometre of ice was equipped with 5160 DOMs to collect the light produced when a neutrino interacts in the ice. This is done by lowering 86 strings in the ice, each of which holds 60 DOMs. DOMs are positioned between 1450 m and 2450 m below the ice surface, so that there is a vertical DOM spacing of 17 m. 78 of those strings (strings 1 to 78) are placed in a triangular grid with a spacing of roughly 125 m. The remaining

[3] It is possible that no ATWD is available. In that case, the FADC is read out immediately.

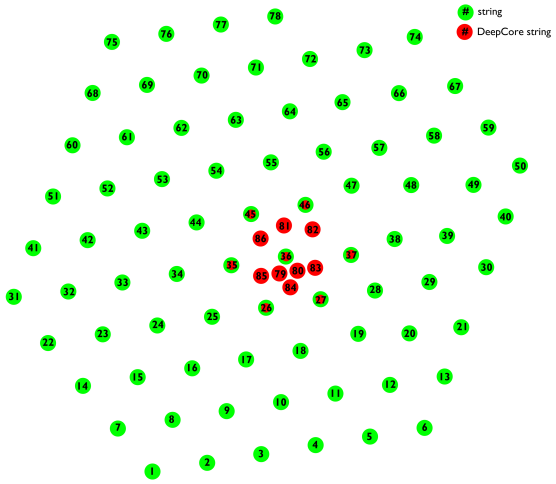

Figure 2.5: Top view of the IceCube strings

eight strings are placed central in the detector with a smaller string spacing. These strings form, together with the 7 closest strings, the DeepCore sub detector. The string positioning can be seen on Figure 2.5.

Highly relativistic muons travel about 5 m in ice per GeV kinetic energy. Since signal from multiple strings is preferred, this DOM spacing leads to a minimum neutrino energy threshold for most analysis of about $50 - 100$ GeV and an optimal response at $E_\nu \gtrsim 1$ TeV using the main part of the detector [68].

2.3.1 DeepCore

The fifteen strings indicated with red in Figure 2.5 form the DeepCore detector. Eight of those strings (strings 79 to 86) are deployed specifically for DeepCore, the seven other strings (26, 27, 35, 36, 37, 45 and 46) are normal IceCube strings that extend DeepCore. The DOM positioning on the dedicated DeepCore strings can be seen in Figure 2.6.

DeepCore is used to locally lower the energy threshold of IceCube. The average interstring horizontal distance between 13 of the 15 DeepCore strings is 72 m. For six of the 15 DeepCore strings, the interstring spacing is 42 m. Of each new string, 50 DOMs with 7 m vertical spacing are locates in the deepest ice instrumented by IceCube, between 2100 and 2450 m below the surface. The region between 2000 and 2100 m depths is not instrumented with DeepCore DOMs due to significant scattering and absorption in that region. The remaining 10 DOMs of each of the eight high-density strings are placed directly above this region with a spacing of 10 m, providing an added overhead veto “plug” to reject background of vertical cosmic rays [68].

This smaller DOM spacing is combined with improved ice quality and HQE PMTs, *high quantum efficiency PMTs*. These PMTs have a quantum efficiency that is improved by 30%. Applying the logic used to estimate the IceCube low energy threshold on the reduced DOM spacing and combining it with the improved PMT and ice characteristics yields a threshold of 10 – 20 GeV.

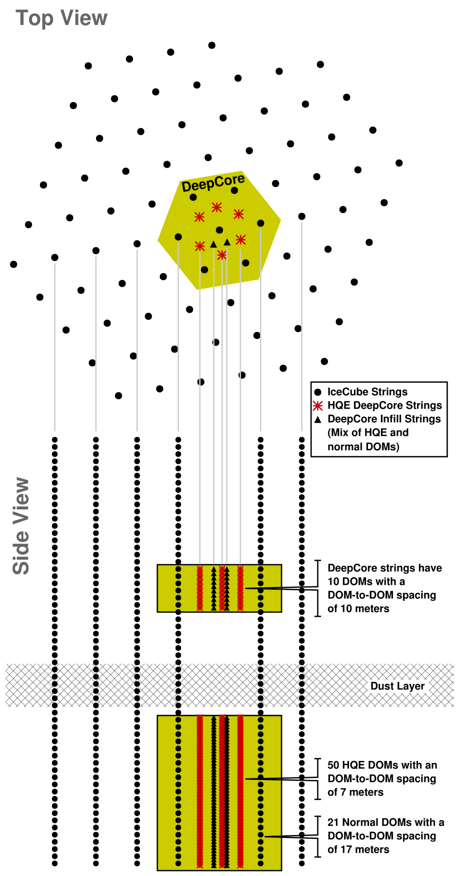

Figure 2.6: A schematic layout of IceCube DeepCore [68].

2.3.2 Ice properties

The optical quality of the ice is a crucial factor for the success of IceCube. Ice quality is mainly determined by two factors, scattering and absorption. Scattering is quantified by the effective scattering length, this is the typical length over which randomization occurs in the limit of many scatters when scattering is not isotropic. In this case, scattering is peaked strongly forward [69]. Absorption is quantified by the absorption length. This is the distance at which the survival probability drops to $1/e$. For both scattering and absorption, the reciprocals of effective scattering length and absorption length are in use. These parameters are named effective scattering coefficient and absorptivity respectively. AMANDA[4], the predecessor and proof of concept of IceCube, thoroughly investigated these parameters, they are plotted in Figure 2.7.

Scattering

Up to $\approx$ 1300 m, scattering is dominated by air bubbles trapped in the ice. From $\approx$ 1400 m on, bubbles are compressed and converted to non-scattering air hydrate crystals. Below 1400 m, four distinct peaks are present in the scattering coefficient depth profile. These are correlated to peaks in dust concentration due to stadials, temporarily colder periods during a glacial period, in the late Pleistocene (110 kya[5] to 12 kya) [69]. Of those four layers, the deepest is by far the dustiest. This layer is generally referred to as “the dust layer”.

[4]Antarctic Muon And Neutrino Detector Array
[5]kilo years ago, 1000 years ago

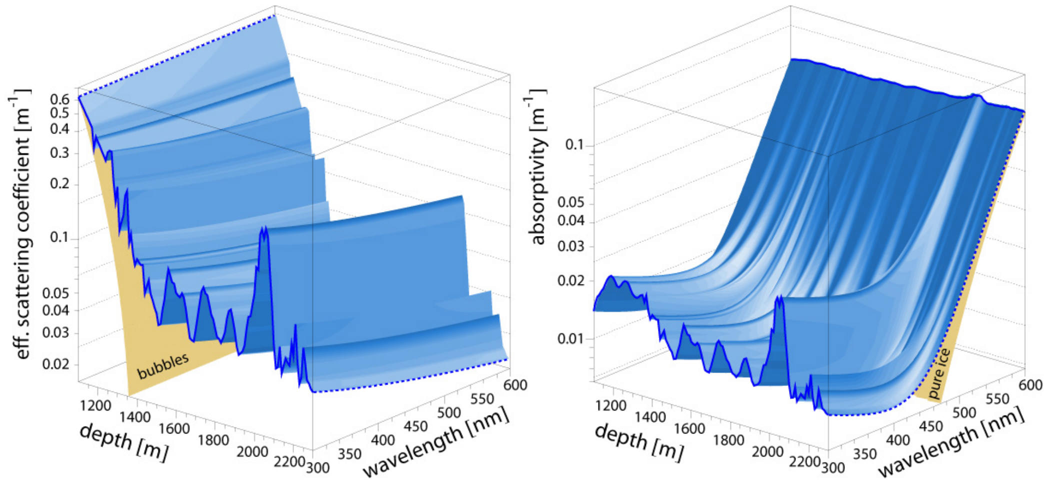

Figure 2.7: Maps of optical scattering and absorption for deep South Pole ice. The depth dependence between 1100 and 2300 m and the wavelength dependence between 300 and 600 nm (left) for the effective scattering coefficient and (right) for absorptivity are shown as shaded surfaces, with the bubble contribution to scattering and the pure ice contribution to absorption superimposed as (partially obscured) steeply sloping surfaces [69].

Absorption

Absorptivity of ice can be parametrized by a three component model, describing low, intermediate and high wavelength behaviour. In the intermediate range, from $\approx$ 200 nm to $\approx$ 500 nm, pure ice is believed to be extremely transparent and absorption is dominated by impurities in the form of insoluble dust [69]. This window roughly coincides with the wavelength range seen by the PMTs (300 nm to 650 nm) [65].

It was found that deep South Pole ice has much higher absorption lengths than lake ice or laboratory ice grown from purified water. Even though the south pole ice was formed over several geological eras associated with warmer and colder periods, which on turn are associated with respectively a cleaner and a dustier atmosphere, the glacial ice is far cleaner than lake ice and probably also chemically purer than laboratory ice [69].

The depth range in which IceCube DOMs are placed, from 1450 m to 2450 m below the surface, is chosen in function of the mechanical and optical properties of the ice. Above 1400 m, bubbles are present in the ice and it is rendered useless. Below 2450 m, the ice gets contaminated by rock dust from the bedrock over which the glacier slides. The DeepCore DOMs are deployed such that they are in the clearest parts of the ice, avoiding the dust layer.

The mechanical properties of the ice make it so that deployment to right above the bedrock is impossible. The deeper ice, which is virtually frozen to the rock surface, moves significantly slower than the top 2000 m of the ice, which moves at 10 m/yr. This difference in velocity gradually deforms the array and might ultimately snap a string. The deepest ice is avoided to counteract snapping, but deformation of the array will occur. This will lead to decreased reconstruction accuracy of the IceCube detector [70].

2.3.3 Construction

The South Pole is a very barren place with hard working conditions. Next to the extreme weather conditions (the highest recorded temperature in the Amundsen-Scott South Pole Station is $-12.3°$C, the lowest $-82.2°$C.), there is also the day-night cycle that is unlike any other place on earth[6]. Because of its position on the Geographic South Pole, the sun rises and sets only once per year, respectively on the September and the March equinox. This leads to a six month "day", followed by a six month "night". During the "night", temperatures drop as low as $-62.8°$C. For obvious reasons, construction happened only during the Antarctic "day" and therefore took several years. Building started in 2005 and was finished in December 2010.

To deploy a string, a 2.45 km deep 50 cm wide hole has to be made in the ice. The first 50 m are a *firn layer*, a layer of compressed snow that has not turned into ice yet. Those first 50 m are drilled with the firn drill. This is an ordinary drill head heated with hot water from the inside to quickly reach the actual ice.

The remaining 2.4 km is drilled with a water drill. Hot water is pushed out of the drill, this melts the ice and leaves a water filled hole. To heat the water needed to drill a single hole, roughly 26500 l of fuel is needed. After the hose and drill have been extracted, deployment can start. First, a 262.15 kg[7] weight is attached to the string. This is lowered into the hole until the first DOM has to be attached. Subsequently, a DOM gets attached and the string gets lowered 17 m, where the next DOM has to be attached to the string. When all DOMs are on the string, it gets lowered until the weight has reached its target depth of 2403 m. The cable then gets fixed in place and a cover is placed over the hole. This is necessary for both safety and physics reasons. The water column remains liquid for about two days, falling into the hole would be dramatic at best and lethal at worst. During the liquid phase, exhaust from the water heater can drift into the water and lessen the optical quality of the ice.

After installation of the string, the end has to get connected to the IceCube counting house. All data gets collected there and a first data selection is made. Events that are pure electronic noise get removed. Various tests are done on the remaining data, events that pass certain tests are labelled as such and are stored until the information can be brought to the northern hemisphere. This can be done either by sending it via a satellite or by physically flying the hard drives to the north.

[6] Except for the North Pole, but there is no land under the North Pole ice.

[7] 400 lb

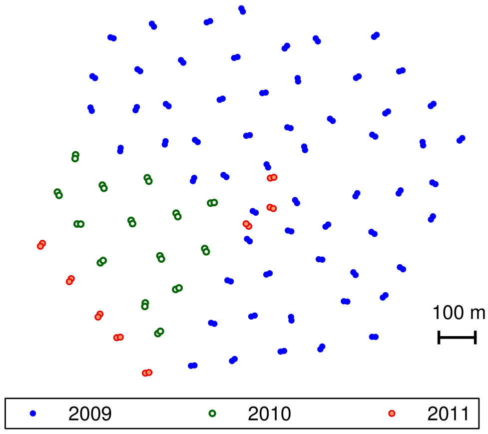

(a) IceTop detector configuration [71]

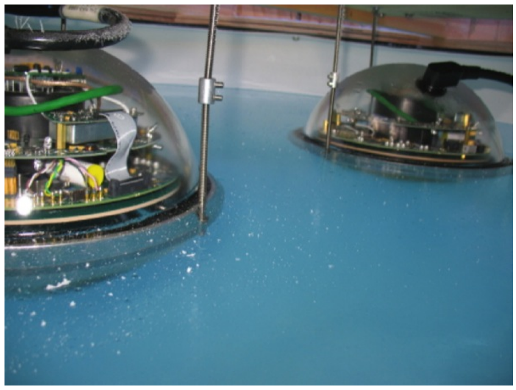

(b) Inside view of an IceTop tank.

Figure 2.8: IceTop configuration

2.4 IceTop

IceTop is the surface segment of the IceCube Neutrino Observatory. It is mainly used as a cosmic ray observatory, but also as a veto for the IceCube detector. The unique location of the detector allows for very good detection of EASs. As it is build on top of a glacier which finds itself on the Antarctic continent, it is situated 2835 m above sea level. This specific elevation has the advantage that it is close to the height where the average EAS reaches its maximum. As a result, an EAS detected with IceTop will give a stronger signal than a similar EAS detected with a detector at sea level.

81 individual stations make up the full IceTop detector. 78 stations are positioned approximately above the IceCube strings. The IceTop equivalent of DeepCore, the InFill array, does not follow the layout of the DeepCore strings. Only three of the eight DeepCore strings have an IceTop station. The position of all tanks and the year of deployment is shown in Figure 2.8a.

An IceTop station contains two tanks, separated approximately 10 m. Each of the tanks holds two DOMs, positioned 58 cm apart. An IceTop tank is a cylindrical vessel of 1.8 m diameter filled with 50 cm of clear ice. Until the water in the tank is frozen, the two DOMs are suspended from the top of the tank such that the PMT is fully submerged. This can be seen on Figure 2.8b. When the water is frozen, the suspension is removed and the DOMs get connected. Because the counting rate of IceTop DOMs is much higher than IceCube DOMs, every DOM has an individual connection to the counting house. Each tank is lined with a reflective material to increase light collection. To maximize the dynamic range of the tank, the two DOMs are operated at different gains ($5 \cdot 10^6$ and 10^5) [66].

2.5 Physics goals

The IceCube Neutrino Observatory was designed and built with a clear goal in mind: making a neutrino telescope. A well-designed neutrino telescope can [72]

- search for high energy neutrinos from transient sources like Gamma Ray Bursts (GRB) or supernova bursts;
- search for steady and variable sources of high energy neutrinos. e.g. Active Galactic Nuclei (AGN) or Supernova Remnants (SNR);
- search for source(s) of cosmic rays;
- search for Weakly Interacting Massive Particles (WIMPs) which may constitute dark matter;
- search for neutrinos from the decay of superheavy particles related to topological defects;
- search for magnetic monopoles an other exotic particles like strange quark matter;
- monitor our galaxy for MeV neutrinos from supernova explosions and operate within the worldwide SuperNova Early Warning System (SNEWS) triangulation network;
- search for unexpected phenomena.

2.5.1 High energy neutrino physics

A standard technique to search for high energy neutrinos of astrophysical origin is to look for upgoing muons induced by muon neutrinos that interacted in the earth. As the PMTs face down, the detector is designed to maximize sensitivity to ν_μ-induced muons from below. Muons from astrophysical neutrinos can be discriminated from muons from atmospheric neutrinos on a statistical basis via the energy spectrum. The atmospheric neutrino flux falls off faster with increasing energy than the astrophysical flux. From a certain energy, the astrophysical flux will dominate over atmospheric flux, this can be seen in Figure 2.9.

As can be seen in Figure 2.3, the cross section for neutrino interactions increases with rising energy. From 100 TeV on, the Earth becomes increasingly opaque to neutrinos. At roughly 1 PeV, no muon or electron neutrinos or ν_μ-induced muons will appear from the Nadir. All muon neutrinos will interact long before the point where a muon might still reach the detector, this can be seen in Figure 2.10. Even if a muon would reach the detector, it will have lost so much energy that it can no longer be associated with a high energy neutrino. The attenuation of electron and muon neutrinos is shown in Figure 2.11.

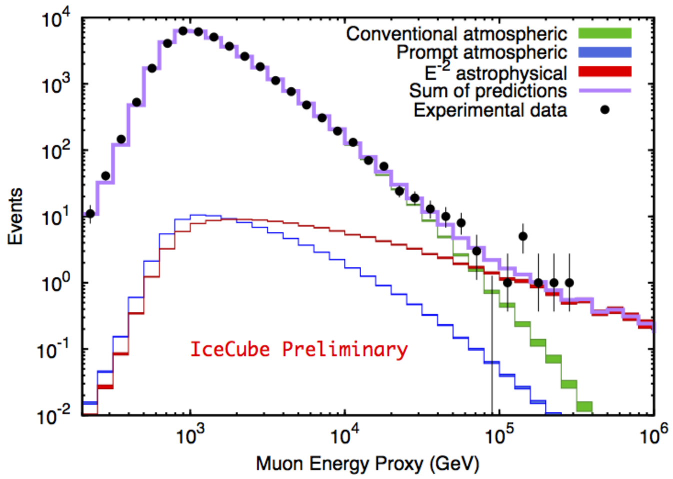

Figure 2.9: Energy distribution of muon neutrino induced events measured by IceCube. The hypothesis of an atmospheric only flux is rejected at 3.9 sigma [73].

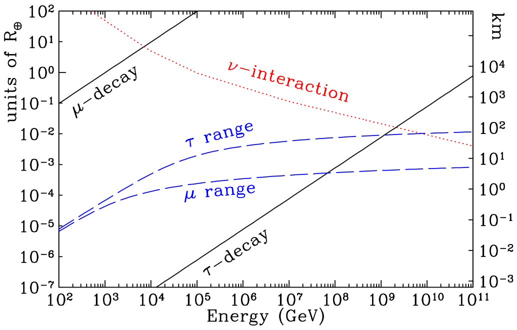

Figure 2.10: Some important length scales versus the energy in GeV for the neutrino or charged lepton. *Solid lines*: the μ and τ decay lengths (ignoring energy loss). *Dashed lines*: the μ and τ range in standard rock (22 g mol^{-1}, 8 g cm^{-3}). This is the length over which they would be fully stopped by their electromagnetic interaction (ignoring decays). *Dotted line*: the neutrino interaction length (the Glashow resonance is not included) [74].

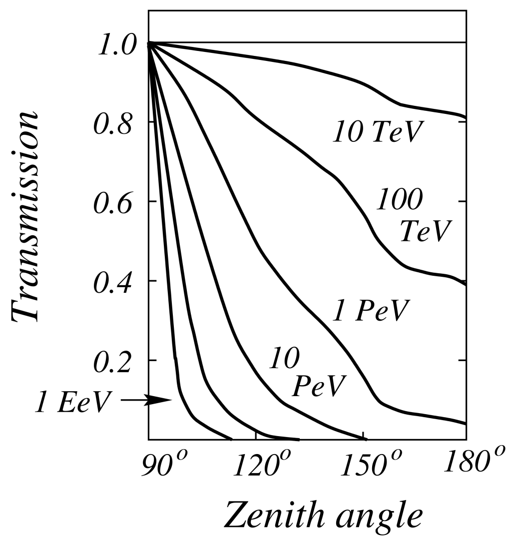

Figure 2.11: Transmission coefficient of the Earth for electron and muon neutrinos as a function of energy and zenith angle. Tau neutrinos have a transmission coefficient of ≈ 1 due to ν_τ regeneration effects, but their energies are degraded [72].

This attenuation is not there for τ neutrinos due to ν_τ*-regeneration*. Figure 2.10 helps explaining this concept and also shows why there is no ν_μ-regeneration. The solid lines indicate the distance a lepton travels in vacuum before it decays. There is no electron line since electrons are stable. The dashed lines indicate the distance a charged lepton can travel before it is stopped by electromagnetic interaction with the surrounding medium. There is again no line for electrons as they as they lose energy very rapidly. The line would fall below the plotted distance range.

To explain regeneration, one simply has to look at the relative positions of the lines. For muons, the range line is for all energies many orders of magnitude lower than the decay line. So long before the muon decays, it has already lost all of its energy. When the muon eventually decays, a ν_μ will be produced with an energy of roughly half the muon rest energy; the energy of this neutrino is far less that the minimal energy required for detection with the IceCube detector. It is therefore of no interest to IceCube. For tau leptons, this is not the case. For all energies below 10^9 GeV, the tau lepton decays before it has lost all of its energy. For the largest part of this energy range, the tau lepton will have lost only an insignificant fraction of its initial energy before it decays again.

The interaction of the tau neutrino and the decay of the tau lepton are not isolated events. When a tau neutrino interacts, it interacts with an electron or with a quark. In the case of a charged current interaction, the surviving lepton carries about 75% of the initial neutrino energy[8]. When the produced tau lepton decays, decay can happen through many branches. All branches however contain a ν_τ and on average, 40% of the tau energy is transferred to the tau neutrino. This regenerated ν_τ carries a fraction $0.75 \cdot 0.4 \simeq 0.3$ of the initial ν_τ energy [74]. So even though tau neutrinos with an initial energy higher than 1 PeV will make it through the earth, they will have lost so much energy during the transfer of the earth that hardly any tau neutrino coming from the Nadir will have an energy exceeding 1 PeV.

2.5.2 Other physics goals

Obviously, $10-20$ MeV supernova neutrinos are far below the detection threshold of IceCube, local coincidence is never satisfied for such a low energy neutrino event. A galactic supernova could be detected however by an increased trigger rate of the individual PMTs over a time window of $5-10$ s. By summing over all PMTs, this increase should be significantly above the dark rate [72].

WIMPs are a popular candidate to make up dark matter. If they do, they would populate the galactic halo of galaxies, including our own Galaxy. If WIMPs collide, they can annihilate pairwise and produce high energy neutrinos[9]. As WIMPs are very heavy, they should be captured gravitationally by stars ans planets where they can annihilate. As WIMPs are only a theoretical model, there is no fixed mass. The

[8]This is also valid for electron and muon neutrinos.

[9]The fact that WIMPs make up dark matter and that they can annihilate to neutrinos is part of a model favoured by theorists.

IceCube Neutrino Observatory is sensitive to WIMPs with mass > 50 GeV annihilating in the center of the Earth if they decay to muon neutrinos (this should be the case in one third of all WIMP annihilations). The IceCube Neutrino Observatory is also sensitive to WIMP annihilation neutrinos from the sun and the galaxy center, but due to the less favourable geometry towards those point sources, the fiducial volume is smaller and the detection threshold is therefore higher [72].

Magnetic monopoles are another theoretically predicted particle, they should be produced during a phase transition in the early universe. A monopole would produce a very distinctive feature in the detector [72].

2.6 Detector signals

As mentioned in Section 2.5, IceCube can be used to detect various physical events. In this section, only high energy events will be mentioned.

2.6.1 Cosmic ray muons

High energy muons produced in cosmic ray events can travel through kilometres of rock and ice before they lose all their energy or decay. They are produced in large numbers, often forming a beam of semi-parallel muons. If such a beam, or even a single high energy muon, travels through the detector, a bright track is produced. This track is characterized by Cherenkov radiation and ionization of the surrounding medium. This ionization frees electrons and produces small cascades along the track.

Cosmic ray muons in IceCube mostly come from the zenith direction. The distance they have to travel to reach the detector, both in ice and in the atmosphere, increases quickly as the direction deviates from the zenith. This distance attenuates the muon beam significantly. On average, a muon loses about 5 GeV of kinetic energy per meter it travels through ice.

2.6.2 Electron neutrinos

As mentioned in Section 2.1, an interacting neutrino always produces a hadronic cascade. If that interaction occurs via the charged current, also the associated lepton is produced. Next to Cherenkov radiation, a highly energetic electron in ice quickly loses energy due to ionization, producing secondary electrons. These secondary electrons also produce Cherenkov radiation and ionize the surrounding medium as well. This process continues until all electrons have lost their energy. As a result, an electron neutrino interacting via the charged current gives rise to a much brighter cascade (hadronic and electromagnetic) than an electron interacting via the neutral current (hadronic only).

2.6.3 Muon neutrinos

Muon neutrinos were already mentioned in Section 2.5. A muon neutrino interaction via the charged current gives rise to the typical neutrino interaction cascade and a muon. Unlike the electron, the muon does not lose all of its energy immediately. Instead, it leaves the interaction position and carries of the neutrino energy that did not go into the quark. The resulting signature is a cascade with a single, leaving muon track.

Given the finite detector volume, this signature gives rise to different topologies. The initial neutrino interaction can either be inside or outside of the detector volume. Events in which the neutrino interaction is contained inside the detector have the topology described earlier. A cascade in the detector and a leaving, bright track.

In the case where the initial interaction is outside the detector, only a single muon track is visible. This is similar to the background of cosmic ray muons. In this case, the point of origin has to be used to conclude if the track is native from a cosmic ray event of from a muon neutrino. Events close to the Zenith can be vetoed with IceTop. If IceTop detected an EAS that can be causally linked with the track, it is not an astrophysical neutrino event. Since IceTop sits exactly on top of IceCube, this method can not be used for slightly more declined tracks. Tracks that come from below the horizon are definitely neutrino induced. This is the signal for which IceCube is optimized.

Even though muons are intrinsically unstable particles, decay is never really considered. At the energies considered for neutrino events, these muons are boosted so much that they are virtually stable.

2.6.4 Tau neutrinos

A tau lepton is much more unstable than a muon, even at very high energies the range of a tau lepton is limited. As a rule of thumb, a tau lepton travels 49.02 m per PeV kinetic energy before decaying. Because tau leptons hardly lose any energy in the ice, they still have a lot of energy when they decay. This decay opens a new range of event topologies.

First of all, several decay modes are possible, as listed in [6]. In case of τ^- decay, a ν_τ is always one of the decay products. The other particles are either an electron and an electron neutrino (17.83%), a muon and a muon neutrino (17.41%) or (a combination of) hadrons (64.76%). There is a wide variation of hadronic decay modes, mostly with a very small branching fractions. All hadronic decays result in a combination of pions and/or kaons (both charged and neutral).

At energies where a ν_τ can be easily differentiated from a ν_μ or a ν_e, i.e. when the tau track is at least 100 m, hadrons created in the tau decay get boosted. The distance travelled before decay (ignoring interactions) by these boosted hadrons is indicated in Table 2.1. Except for π^0, the produced hadrons would travel many kilometres in vacuum before they decay. Since they travel through ice and interact via the strong force, interactions are certain to occur. At the considered energies,

hadron	decay time (s)	$c\tau$ (m), (1 PeV)
π^-	$2.60 \cdot 10^{-8}$	$5.59 \cdot 10^7$
π^0	$8.52 \cdot 10^{-17}$	0.19
K^-	$1.24 \cdot 10^{-8}$	$7.52 \cdot 10^6$
K_S^0	$0.90 \cdot 10^{-10}$	$5.39 \cdot 10^4$
K_L^0	$5.12 \cdot 10^{-8}$	$3.08 \cdot 10^7$

Table 2.1: Hadrons produced in hadronic decay of a τ^-. The second column has the lifetime in seconds, the third column the decay length in vacuum for a kinetic energy of 1 PeV

hadronization resulting in a hadronic cascade is a certainty.

Recalling the description of a ν_e (Section 2.6.2) and a ν_μ (Section 2.6.3) interaction within IceCube, one can conclude that the detectable part of a high energy tau neutrino interaction in ice will always contain an initial cascade and a dim tau track. Depending on the decay mode of the tau, either a high energy muon (17.41%) or another cascade (82.59%) will appear at the end of the tau track. In the case of a cascade, it can either be an electromagnetic (17.83%) or a hadronic (64.76%) cascade. Again considering the finite volume of the detector, this behaviour gives rise to different signal topologies. The following paragraphs give an overview of those different possibilities. They are quickly summarised in Figure 2.12.

Lollipop

This is where the actual neutrino interaction takes place outside the detector, the tau migrates into the detector volume and decays there hadronic or electronic (82.59%). The resulting signal is a dim track coming into the detector, followed by a cascade at the end of that track. Beyond that cascade, no track continues.

Using this topology has the advantage that the detection volume is increased. For extremely high energy events, the tau neutrino could interact kilometres away. It does have the disadvantage that the minimum energy required for this type of events is gigantic. Requiring 200 m track length gives a minimal energy of 4 PeV.

ν_τ regeneration does not allow for 4π detection with this topology as it degrades the neutrino energy. Only events from above the horizon can be seen using this topology.

Sugar Daddy

The Sugar Daddy topology is the counterpart of Lollipop events. The tau neutrinos also interacts outside the detector volume and the tau enters the detector, but then decays muonic (17.41%). An event like this would therefore be a dim track coming in and a bright track getting out. The moment the tau decays into a muon is also the moment the track brightness increases. Also a small kink in the track is possible, this was already discussed in Section 1.2.4.

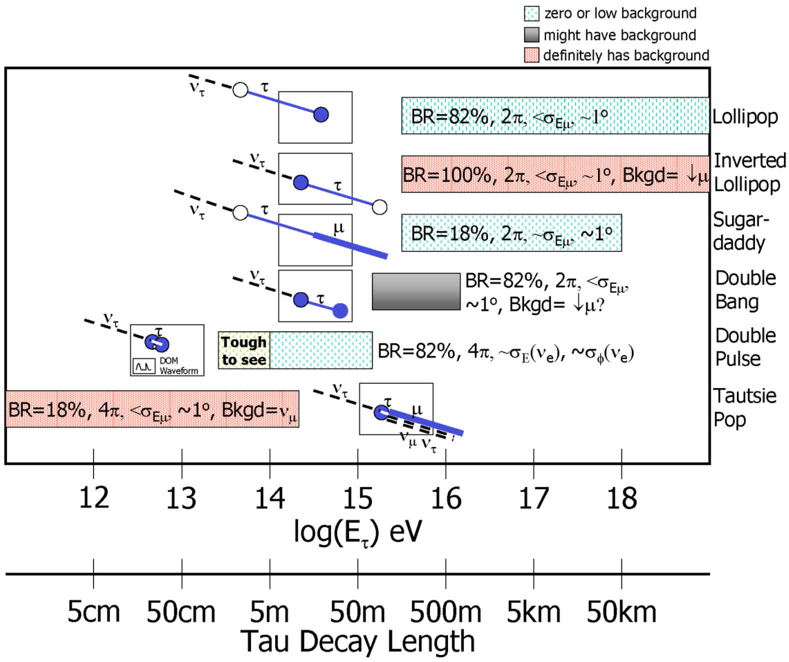

Figure 2.12: All ν_τ event topologies possible with IceCube. For every event, the topology is sketched on a cross section of the detector. Next to that sketch, the energy range over which this topology is possible is indicated by the coloured band. In that band, there is the branching ratio (BR), the opening angle, the estimated energy resolution compared with other detection channels of IceCube, the pointing resolution and, if present, the background. For Double Pulse events, the extra region "tough" is indicated. At those energies, it will be very hard to separate ν_τ from ν_e events [75].

Inverted Lollipop

A high energy ν_τ interacts with the ice inside the detector and the subsequent tau lepton travels out of the detector, this is the topology of an Inverted Lollipop event. The method of decay of the tau lepton is irrelevant in this topology, giving it a branching fraction of 100%.

Just like the Lollipop topology, this method also has an extended detection volume and requires a very high energy. On top of that, it has the added disadvantage that is very similar to a muon neutrino event. Both events consist of a cascade and a leaving track. A muon neutrino and a tau neutrino are expected to deposit the same amount of energy into the initial hadronic cascade if they have the same neutrino energy. The tau track will however be less bright than the muon track. The difference has to be made by comparing the brightness of the leaving track with the energy deposited in the cascade.

This event topology has the same energy requirements as Lollipop events. Also here, a 4π opening angle is not possible due to the energy deprecation of the tau neutrino in regeneration.

Double Bang

A Double Bang event is the topology where a ν_τ interacts, propagates and decays inside the detector. The tau is required to propagate over such a distance that the two decays can easily be separated using the position information of the hits, typically 100 m. Because of the cascade separation requirement, these events also require a high energy, starting from about 2 PeV. At this energy, ν_τ-regeneration already plays a role. One can therefore argue that Double Bang events also have only 2π opening angle.

Double Pulse

This is the low energy version of a Double Bang event. If the two cascades can not be easily separated based on position information, one has to rely on the timing information in the ATWD. A DOM that is close to the event should see the light of the first cascade arriving first and only some time later, the light of the second cascade will arrive. This “double pulse” in the ATWD waveform can be used to separate this topology from electron neutrino events. DOMs that are further away from the interaction and decay points will not be able to make this separation due to scattering of the light.

Low Energy μ Lollipop

This topology resembles more the topology of an Inverted Lollipop. It is also the low energy version of a Sugar Daddy. A tau neutrino interacts within the detector. The produced tau lepton decays before it has left the expanding cascade into a muon. As a result, this event looks very much like a muon neutrino interaction. The only difference is that a significant fraction of the energy is carried away by the two neutrinos. This should cause the E_{shower}/E_{track} to be larger by a factor $2-3$ than for muon neutrino events.

Even though this channel has a small branching fraction, it has the benefit that it is available down to very low energies, possibly tens of TeV.

Chapter 3

Software and Simulation

3.1 Software

The IceCube Collaboration uses dedicated software modules to process data and Monte Carlo simulation. These modules are gathered in an IceRec metaproject. A file extension, .i3, was created to efficiently store and handle data and Monte Carlo simulations. The IceTray framework acts as a carrier between the i3 files and IceRec.

3.1.1 i3 files

i3 files are separated in frames, of which six types exist. A frame is a dictionary structure whose name gets determined by its entries. The I frame (TrayInfo) contains the processing history of the file. The G frame (Geometry) holds the x, y and z position of the IceCube DOMs. The C frame (Calibration) contains the calibration information, such as PMT voltage, of every DOM. The D frame (DetectorStatus) contains information about bad DOMs, broken LC links etc. The Q frame (DAQ) contains all DOM output of a single event. In case of simulation, also a particle tree containing the Monte Carlo truth is present.

The P frame (Physics) holds a processed version of the DOM output, i.e. the ATWD and FADC bin values are converted into "hits" with definite charge (the number of PE that entered the multiplier section of the PMT), time and LC information. For IC79, the detector configuration used in this thesis, hits are stored in "OfflinePulses". This is a library structure with an entry for every DOM that triggered in the event. The content of each entry is a time ordered list of all hits in that DOM. Additional information from calculations is added to the P frame as well. This will be elaborated further in this section.

The G, C and D frames are the same for a number of events. They therefore do not get added to every i3 file but are stored in separate files, so called GCD files. For every run in IceCube, a single GCD file is created[1]. For physics simulation, only

[1]A typical run lasts 8 hours and an i3 file is created every few minutes.

one GCD file exists for every detector configuration[2].

A typical data file consists of a series of Q and P frames. It can happen that several P frames belong to a single Q frame. This is the case when multiple events take place at the same time in the detector. The hit information of the entire detector is then split into individual events and each event is stored in a separate P frame. The most basic splitting is done "online", before events get written to disk for the first time. After the necessary splitting took place, several online tests and reconstructions are done. The results of these are added to the P frame.

The P frame contains, next to the event hits and information of online test and reconstructions, also several pulse series. These are the hits cleaned to a particular purpose, this mostly means removing noise. Pulse series have the library structure of OfflinePulses, but contain a boolean for every hit. This boolean indicates if that particular hit is noise or part of the event. In this analyses, the TWOfflinePulsesHLC pulse series is used. HLC stands for hard local coincidence, all hits that do not satisfy local coincidence conditions are rejected from the OfflinePulsesHLC pulse series. The added TW stands for time window cleaning, only hits reconstructed within 6 μs from the first hit are kept.

The I frame only gets added when analyses is conducted. One I frame exists in every file. Even when files get merged, only one I frame is kept.

3.1.2 IceRec and IceTray

Several releases of IceRec exist. In every release, standard pieces of software are included to read, write and manipulate i3 files. Also non standard, but still purpose written, software is available in a svn repository. These can easily be added to a personal IceRec installation. Also up and downgrades of the standard projects can be performed. This software comes in modules and services.

To use an IceRec module or service on an i3 file, it has to be added to an IceTray tray. Personal functions can be added to a tray as a module. Analysis code consists of initiation of a tray, a series of modules and services that are added and a statement to execute the analysis [76].

Most modules and services available in IceRec are written in C++, but pybindings exist so that analysis code can be written in python. This gives the ease of use of coding in Python combined with the superior calculation speed of C++ code. All code for this analysis is written in Python.

3.2 Simulation

In order to do an analysis, the proper events have to be selected from the huge data set. This can not be done by hand, there are simply too many events. Also, when

[2]Also benchmark and systematics simulation exists. These can have different GCD files but are of no consequence here.

humans grow tired, they tend not to pay attention to their task. This gives ample room for mistakes.

The protocols for event selection ultimately have to be written by humans, but they are executed by computers using strict criteria. To come up with those criteria, detector simulation of both the sought after signal and the background is needed.

3.2.1 Atmospheric muons

Simulation of atmospheric muons is done with Corsika (COsmic Ray SImulations for KAscade[3]), modified to fit the situation of IceCube. Corsika takes an initial isotope with a certain energy and direction and calculates the positions, directions and energies of the muons that will reach the detector.

These muons are passed on to the Muon Monte Carlo (MMC) program which propagates them through the detector and its vicinity. Several software modules are subsequently used to calculate in which DOMs the emitted Cherenkov photons would produce a photo electron and how the detector reacts to those photo electrons. Also random noise hits are added to make a more realistic simulation.

3.2.2 Neutrinos

Neutrinos are simulated with Neutrino Generator, or NuGen for short. NuGen puts a neutrino with a chosen energy and flavour on a chosen position on the surface of the Earth and propagates it towards the detector. To do this, the cross sections of Figure 2.3 and an earth model [77] are used. If the neutrino reaches the detection volume[4] without interaction, it is forced to interact there.

NuGen takes into account ν_τ regeneration; if a ν_τ interacts via a CC interaction and a tau lepton is produces, it is propagated and then made to decay. The new neutrino is then again propagated as if it were the initial neutrino, being forced to interact inside the detection volume if no interaction, or only NC interactions, occurred before it reached the detection volume. In case of a muon being produced in the Earth, NuGen calculates if it can reach the detection volume. If it can, it is passed to MMC[5]. Otherwise, NuGen forces the interaction into a neutral current interaction.

This process gives rise to charged leptons and interactions that will result in cascades in the detection volume. NuGen does not simulate these cascades or the propagation of the leptons, it passes them on to programs like Cascade Monte Carlo (CMC) and Muon Monte Carlo[6] (MMC). From there on, the steps that are taken

[3] Kascade is a cosmic ray experiment in Karlsruhe, Germany.

[4] The detection volume for NuGen is not the actual detector volume. It is extended to a cylinder around IceCube to allow for Lollipop and Sugardaddy signatures in case of ν_τ, for upgoing muons in case of ν_μ and for uncontained cascades of any flavour.

[5] In more recent, mainly for IC86, neutrino simulations, PROPOSAL is used to propagate muons and tau leptons.

[6] Also tau leptons are propagated by MMC. MMC was designed to propagate both tau leptons and muons, but was named only for muons. There is however a problem in tau lepton propagation,

in atmospheric muon simulation are also taken here.

3.2.3 Event weighting

Both Corsika and NuGen calculate the physical outcome from a given initial condition, another program is required to generate that input. With this program, one can cheat nature and generate whatever input is most suited. If one wants to do a study of highly energetic events, it would be a waste of computer power to simulate the real, soft, physical spectrum of cosmic radiation or astrophysical neutrinos. Almost all events would be of low energy and therefore uninteresting.

To avoid this, a harder spectrum is generated so that more interesting events come out of the simulation. Because one wants to learn about the real world and not about how the world would look with some arbitrary spectrum that happens to fit the research goal, every event is given a weight corresponding to its energy and inclination[7]. This weight expresses the expected flux of similar events in the detector [78].

In the case of neutrino simulation, a neutrino is forced to reach the detection volume and interact in it, this can require altering the neutrino interaction cross sections. For non tau flavours, this happens in two steps: weighted propagation and weighted interaction. For ν_τ, propagation is not an issue because of regeneration. Therefore only weighted interaction has to be applied to ν_τ.

Weighted propagation

For very high energies, the Earth is opaque for neutrinos (see Figure 2.11), a high energy neutrino would never reach the detector from the Nadir. In order not to waste computer time, NuGen forbids CC interaction deep in the earth if the produced lepton can not reach the detection volume. Every time a neutrino is simulated to interact via CC, interaction via the NC or Glashow resonance[8] (if possible) is selected instead and the weight of the event is altered by a cross section dependent factor.

This process is continued until the neutrino reaches the detection volume, in which it is forced to interact. If however a muon was produced outside the detection volume and it was found that it can reach the detection volume, the neutrino is neglected and only the muon is considered.

this is the reason for the switch to PROPOSAL.

[7]The weight is based on the direction, but as the detector sits just below the surface of a sphere, only the inclination counts.

[8]The resonant formation of an intermediate W^- in $\bar{\nu}_e e$ collision at the anti-neutrino energy $E_{\bar{\nu}} = 6.3$ PeV, this is the spike in Figure 2.3.

particle type	dataset
cosmic ray muons	7017
atmospheric ν_μ	6454
atmospheric ν_e	6461
astrophysical ν_τ	6466
astrophysical ν_μ	6454
astrophysical ν_e	6461

Table 3.1: Simulation datasets used in this thesis

Weighted interaction

If only neutrinos reach to the front surface of detection volume, NuGen forces interaction somewhere inside the detection volume by increasing the neutrino interaction cross section. Interaction weight must be applied in order to compensate this. This is also done based on the factor with which the cross sections had to be altered [79].

3.3 Used IceRec and simulation sets

In this thesis, IceRec V04-05-05 was used. However, some modules were added, upgraded, downgraded or even slightly hacked for the analysis to work. The used simulation sets can be found in Table 3.1. ν_τ Lollipop events were selected from the astrophysical ν_τ dataset using the Monte Carlo truth. To be considered a Lollipop event, the neutrino interaction has to take place on the outside of the detector and the tau decay on the inside. Both interaction and decay have to be at least 50 m away from the detector edge.

The top and bottom of the detector are respectively defined as the height of DOM 1 and DOM 60 on string 21. The side of the detector edge is defined by the geometrical shape of the corner strings (strings 2, 6, 50, 74, 72, 78, 75 and 41). This shape can be seen on Figure 2.5.

Within one flavour, the simulation sets for astrophysical and atmospheric simulations are the same sets. Atmospheric and astrophysical neutrinos behave the same in the detector, they simply have a different origin. The different energy spectra and angular distributions are fixed by applying different weighting to the same events so that two sets of files are created from the same simulation set.

Chapter 4

Analysis

In this thesis, it is the intention to find a set of characteristics that Lollipop events share with no other event type. As computing resources and available time are limited, this has to be done in increasing levels of complexity. At first, a lot of events have to branded "Not a Lollipop" using very little CPU time so that tests for treats that are more CPU intensive only have to be done for a limited amount of high potential events.

In this philosophy, the values of all cut parameters are chosen such that the main source of background is rejected as much as possible while ignoring the effect those parameters have on other types of background. The other types of background can then be dealt with later. This effectively comes down to reducing the number of atmospheric muon (AMu) events. For every applied cut, a table with the rejection rates of signal and all types of background will be included at the end of the section that handles it.

4.1 Online filters

A very CPU friendly way to discriminate between Lollipop events and background is using what is already there. Several test are being done online, at the South Pole [80]. The results of these tests are simply available in the data, no CPU time is required. A lot of these tests are for very specific purposes and are therefore not useful. Two tests that have potential are the Cascade Filter and the Extremely High Energy (EHE) Filter.

4.1.1 EHE Filter

The EHE Filter aims at collecting energetic events with as less bias as possible. It was found that the total number of photo electrons collected in the detector (NPE) shows a strong correlation with the event energy. It was chosen to set the EHE filter on 10^3 NPE, this reduces the event rate from 2.1 kHz to 1.8 Hz. Air showers

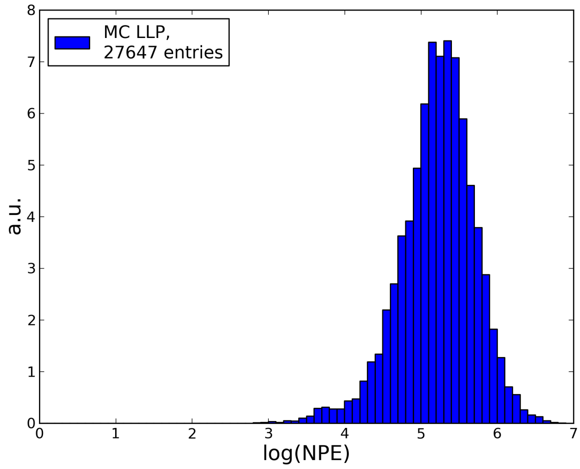

Figure 4.1: NPE histogram of Monte Carlo simulated LLP events, only 0.0309 % of all simulated events has NPE $< 10^3$.

type	rejection rate	pre cut rate	post cut rate	post cut σ
AMu	98.82 %	$2.69 \cdot 10^9$	$31.78 \cdot 10^7$	$0.05 \cdot 10^6$
atm. ν_e	99.67 %	$35.9 \cdot 10^3$	116	1
atm. ν_μ	99.79 %	$584 \cdot 10^3$	$1.21 \cdot 10^3$	$0.02 \cdot 10^3$
astr. ν_e	72.59 %	126.03	34.55	0.04
astr. ν_μ	82.77 %	350.4	60.37	0.009
LLP	0.031%	0.145	0.145	0.001

Table 4.1: EHE Filter information. The rates are expressed in number of expected events per year.

produce 10^3 or more NPE when the total muon energy inside the detector exceeds roughly 300 TeV [81].

When looking at a NPE histogram of Monte Carlo simulated Lollipop events (MC LLPs), as is shown in Figure 4.1, one can see that applying this filter is a good idea. With it, only 0.031% of all Lollipop (LLP) signal gets removed while the data rate decreases with roughly a factor 1000. The flux reduction by this filter for all types of background is shown in Table 4.1.

4.1.2 Cascade Filter

The online Cascade Filter is designed to select cascade like events based on the shape and source *speed* of a distribution of light in the IceCube detector. The shape of the cascade is decided by the *tensor of inertia eigenvalue ratio* ($ToI_{eval.ratio}$). First, the tensor of inertia of the discrete distribution of the triggered DOMs and

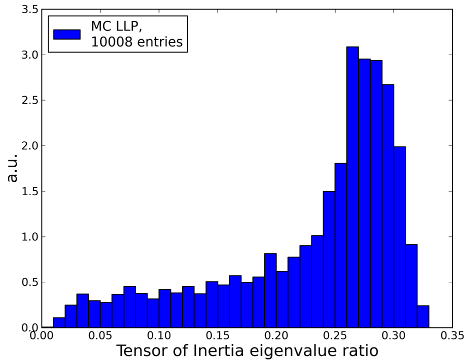

(a) Tensor of Inertia eigenvalue ratio histogram for MC LLP events. The Cascade Filter requires a minimum of 0.05, this is met for 96.49 % of the simulated sample.

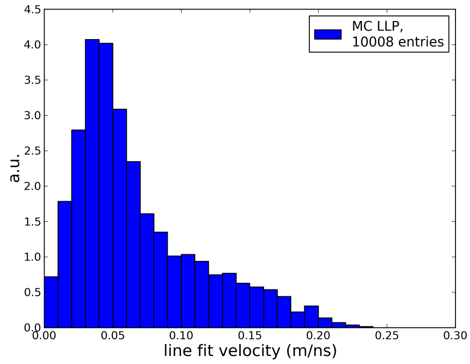

(b) Line fit velocity histogram for MC LLP events. The Cascade Filter sets a maximum of 0.11, this is met for 81.49 % of the simulated sample.

Figure 4.2: Cascade Filter histograms, 18.56 % of MC LLP events gets rejected by this filter.

its eigenvalues are calculate. This is done in the same way as it is done for a mass distribution, using the DOMs as mass elements and the collected PE in that DOM as mass. From these eigenvalues, the eigenvalue ratio is calculated. This is the ratio of the smallest eigenvalue (I_1) and the sum of the eigenvalues,

$$ToI_{eval.ratio} = \frac{I_1}{I_1 + I_2 + I_3}. \tag{4.1}$$

For spherical (cascade like) shapes, the three eigenvalues are roughly the same, leading to a high eigenvalue ratio (~ 0.33). For cylindrical (track like) shapes, the eigenvalue that indicates rotation along the length of the cylinder is significantly smaller than the other two eigenvalues, resulting in a small eigenvalue ratio[1].

The second parameter used is the line fit velocity $\vec{v}$. This can be used to separate a cascade, a stationary source of light, and a track, a moving source of light. Hits are projected along a track moving through the detector with a velocity $\vec{v}$, defined as

$$\vec{v} = \frac{\langle \vec{r} \cdot t \rangle - \langle \vec{r} \rangle \cdot t}{\langle t^2 \rangle - \langle t \rangle^2}, \tag{4.2}$$

where $\langle \vec{r} \rangle$ is the amplitude weighted position of the hits with respect to the track. An event is required to have $ToI_{eval.ratio} > 0.05$ and $\vec{v} < 0.11$ to pass the Cascade Filter, this gives rise to an event rate of 27.3 Hz [82].

It makes sense to have a look at the Cascade Filter. After all, LLPs have a very bright cascade and only a very dim track. Because the track is so dim, it

[1]The eigenvalue ratio decreases as the length of the cylinder increases.

type	rejection rate	pre cut rate	post cut rate	post cut σ
AMu	60.29 %	$31.78 \cdot 10^6$	$12.62 \cdot 10^6$	$0.03 \cdot 10^6$
atm. ν_e	0.86 %	116	115	1
atm. ν_μ	6.61 %	$1.21 \cdot 10^3$	$1.13 \cdot 10^3$	$0.02 \cdot 10^3$
astr. ν_e	0.03	34.55	34.54	0.04
astr. ν_μ	16.91 %	60.37	50.16	0.08
LLP	0.031%	0.145	0.145	0.001

Table 4.2: altered Cascade Filter rejection rates. The rates are expressed in number of expected events per year.

does not make a very large difference for $ToI_{eval.ratio}$, this can be seen on Figure 4.2a. The line fit velocity however does not take track brightness into account. The track drastically increases the line fit velocity, this can be seen in Figure 4.2b. The tail towards high fit velocities contains more events than the tail towards low $ToI_{eval.ratio}$.

An high fraction (18.56%) of the simulated events does not match the criteria set by the Cascade Filter. Due to the low expected event rate for tau Lollipops, the Cascade Filter therefore is not used to detect Lollipop signature events.

4.1.3 Altered Cascade Filter

The online Cascade Filter (oCF) can not be applied in the conditions it is applied on the South Pole. The information from the oCF is however available in the data. Setting the requirements less stringent allows to lose only a small fraction of LLP signal while getting rid of a significant fraction of background from cosmic ray muons. This gives rise to the altered Cascade Filter (aCF) and is depicted in Figure 4.3.

The new thresholds, $ToI_{eval.ratio} > 0.02$ and line fit velocity < 0.2, are chosen such that minimal LLP signal gets rejected while trying to get rid of the bulk of AMu events. Next to the thresholds, also the criterion for rejection are different between aCF and oCF. oCF requires both parameters to be “good” before an event is accepted whereas aCF requires the two parameters to be “bad” before an event is rejected.

In some cases, construction of the tensor of inertia fails (this never happens for Lollipop simulation). In that case, $ToI_{eval.ratio}$ is set to 0 and line fit velocity to c. This is the largest bin in Figure 4.3a. Even when the tensor of inertia can be constructed correctly, $ToI_{eval.ratio}$ sometimes is returned as zero.

Cosmic Ray Muons

The AMu background is depicted in Figure 4.3a. The pattern shown is as expected, a lot of events with low $ToI_{eval.ratio}$ and high line fit velocity indicating a long track.

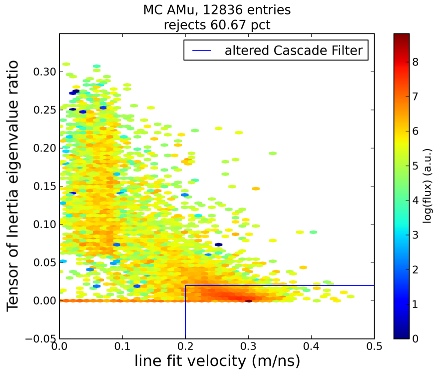

(a) Line fit velocity vs. $ToI_{eval.ratio}$ scatter plot for MC AMu. The colour coding indicates the expected flux and is in a log scale.

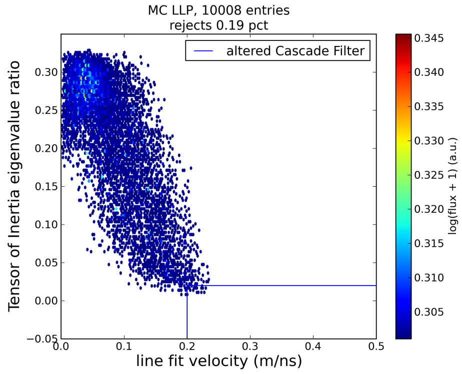

(b) Line fit velocity vs. $ToI_{eval.ratio}$ scatter plot for MC LLP events. The color coding indicates the expected flux.

Figure 4.3: Cascade Filter parameters with modified rejection criteria to suit LLP search. Events that fall below the line indicated with "altered Cascade Filter" and events with $ToI_{eval.ratio} = 0$ are rejected.

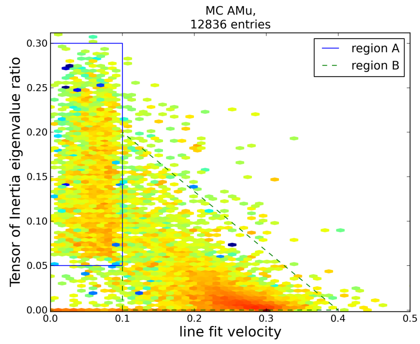

Figure 4.4: A rough topological split of AMu events based on Cascade Filter parameters. Explanation in text.

The AMu events that pass this filter can be separated in two groups, as is shown in Figure 4.4. Region A contains events that undergo a high energy stochastic energy loss inside the detector. Region B holds events that do not undergo such an energy loss. Their combination of parameters is simply due to the orientation and positioning of the muons with respect to the detector.

The events in region A (18.82 % before aCF, 44.36 % after) are those that have a high energy stochastic energy loss within the detector volume. A stochastic energy loss occurs when a charged particle ionizes a molecule in the ice. If the freed electron has enough energy, a cascade that is clearly distinct from the track is created. This cascade increases the smallest eigenvalue of the tensor of inertia while decreasing the two other eigenvalues. Light in a cascade is distributed rather homogeneous, resulting in hits both upstream and downstream from the interaction position. This decreases the line fit velocity.

The events in region B (76.58 % before aCF, 45.45 % after) are ordinary muon tracks that do not undergo a very high stochastic energy loss. The distribution of parameters in the area is due to the length of the muon track inside the detector. The eigenvalue ratio of the event directly depends on the length of the track in the detector, a shorter track has a higher eigenvalue ratio. The decreased line fit velocity can be explained by the Cherenkov cone. DOMs further away from the track get hit by a photon later than DOMs close to the track. If a downstream DOM detects a photon before a further away DOM does, this reduces the line fit velocity. Events with a short track do not have the necessary track length to sort this effect out. Events that travel through the entire detector have a much longer track than events that enter in the top of the detector and quickly leave again via the side or enter from the side and leave through the bottom. These travel only a short distance within the detector.

Next to the two effects explained above, the quality of the line fit also plays a role. A misfit typically results in an increased line fit velocity. Such a misfit is more likely for events with a stochastic energy loss or for events with a very short track.

Lollipops

Figure 4.3b shows the line fit velocity and eigenvalue ratio of the tensor of inertia for MC Lollipop events. The clear correlation that can be seen in Figure 4.3b combined with the energy distribution in Figure 4.5 shows that the events rejected by the altered Cascade Filter have extremely high energies. The maximal energy of an observed neutrino event so far is 2 PeV [83]. The events that get rejected with this altered Cascade Filter have an average energy of 72 PeV. Such an event is expected to occur only once every few centuries.

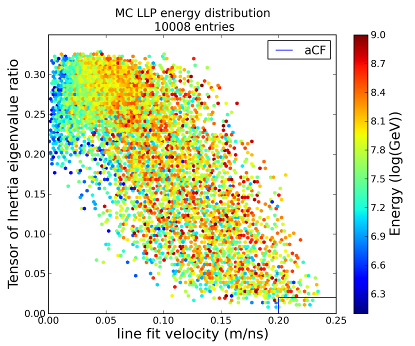

Figure 4.5: Energy distribution of LLP events for the Cascade Filter parameters.

4.2 Peak Charge cut

The main difference between background from atmospheric muons and LLP signal is the decay inside the detector. This happens for LLPs but not for muons. Hadronic or electronic decay of a multi-PeV energy tau lepton produces a large cascade, resulting in a high amount of PE collected in a very short time window. This is not the case for muon beams, those are expected to be bright along the entire track. Periodic differences in light emission and detection can occur. Higher light emission happens when a muon ionizes an atom in the ice, the freed electron then creates a small cascade. Variation in light detection is due to muons being closer or further away from a string and the intrinsic variation in brightness of a muon track.

The described behaviours should result in two very different PE time spectra. A PE time spectrum, as shown in Figure 4.6, shows the amount of photo electrons

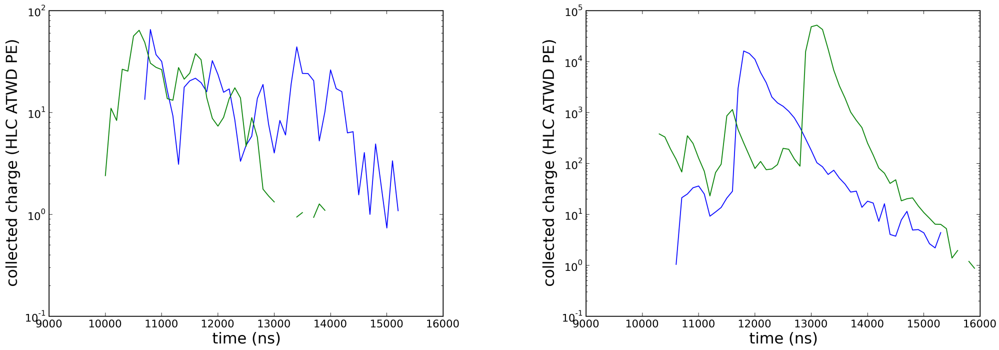

(a) A long and a short AMu event. The short event is a corner clipper, the long event travels a long distance within the detector volume.

(b) Two different energies are shown. The event with the longest track has the highest energy.

Figure 4.6: Time PE spectra for MC AMu and MC LLP events. Bins of 100 ns were used.

detected in the detector at every moment. Because it is not possible and not practical to have this value for every instance, the collected photo electrons are grouped in bins of 100 ns. As Figure 4.6 only serves illustrative purposes, both PE spectra of both event types are ideal cases. It is clear that there is a vast difference between AMu events (Figure 4.6a) and LLP events (Figure 4.6b).

The two AMu events plotted in Figure 4.6a behave as expected. Light is deposited in the DOMs in a fairly constant manner. The variations in brightness can be clearly seen in both events. The two events have a different length, this is to illustrate the difference of a corner clipping event and an event that travels through the center of the detector.

In case of the LLP event, the track and the cascade can be easily separated. The first part with lower light emission is light produced by the tau lepton travelling through the ice. One can see that this part of a LLP event has the same behaviour as an AMu event. Due to the higher mass of the tau lepton, this track should be dimmer than a muon track. The events in Figure 4.6b however have a much higher energy than the events in Figure 4.6a, so that the tau track is brighter. The second part of a LLP event is due to the tau decay and is characterized by a sharp rise followed by a steady decrease in collected light.

This very distinctive peak can be used to separate LLP events from AMu events. On average, the highest collected PE in a bin in an AMu event is not much higher than the average of that event whereas the highest collected PE in a LLP event is much higher than the remainder of the event. For an AMu event and a LLP event to have the same amount of collected PE in their highest bin, the AMu event will

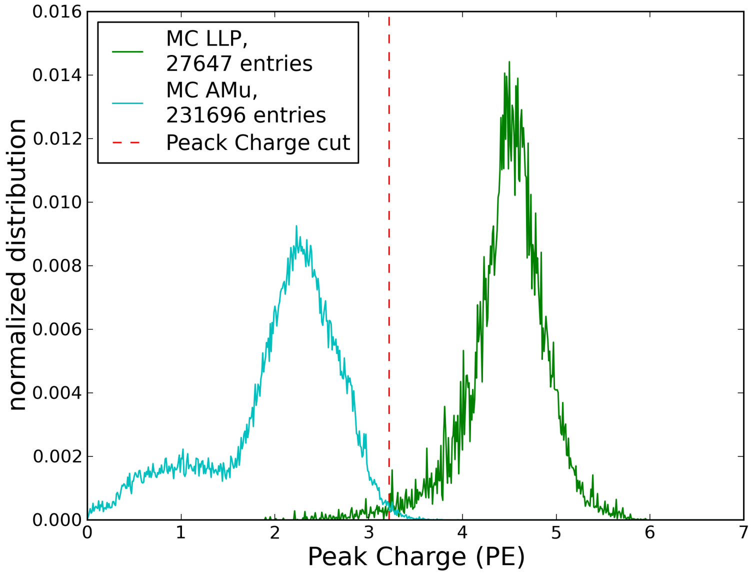

Figure 4.7: Peak charge histogram of MC AMu and MC LLP events. Both histograms are normalized, but represent different total fluxes.

have a much higher average collected PE than the LLP event. Since total PE is correlated with energy, an AMu event with a higher peak bin will, on average, have a higher energy. Because of the primary cosmic ray energy spectrum, the likelihood for a higher highest bin decreases quickly.

This effect can be made even stronger. Light emission in an AMu event happens fairly homogeneous along the track, including the edge of the detector. Light emission of a LLP event mainly comes from the decay cascade. Light from that cascade spreads over the detector, becoming sparser with distance. Due to the topology of a LLP event, this emission starts within the detector. In this way, the edge of the detector collects hardly any light from the cascade. The contribution in the light production of the tau lepton track, which deposits light in the detector edge, is insignificant compared to the contribution of the decay cascade.

Subtracting the contribution of the outer layer of strings and the top and bottom layers of DOMs from the PE time spectrum should therefore separate the PE collected in the highest bin even further for AMu and LLP events. The logarithm of "the value of the highest bin of a PE time spectrum without edge contributions" is the *Peak Charge* of an event. The Peak Charge of a LLP event differs insignificantly with or without the outer layer. The Peak Charge of an AMu events is a drastic decrease of the highest bin at best and an insignificant reduction at worst.

Making a histogram of the peak charge of MC AMu events and MC LLP events shows the difference for those two event types. This is done in Figure 4.7, it can

type	rejection rate	pre cut rate	post cut rate	post cut σ
AMu	99.70 %	$12.62 \cdot 10^6$	$37.8 \cdot 10^3$	$2.6 \cdot 10^3$
atm. ν_e	95.13 %	115	5.6	0.1
atm. ν_μ	97.08 %	$1.13 \cdot 10^3$	33	2
astr. ν_e	76.03 %	34.54	8.28	0.02
astr. ν_μ	83.85 %	50.16	8.10	0.02
LLP	2.76%	0.145	0.141	0.001

Table 4.3: Peak Charge cut rejection rates. The rates are expressed in number of expected events per year.

clearly be seen that there is a large difference between these two event types. Optimisation yields that the Peak Charge for which most AMu background is rejected while keeping as much LLP signal as possible is 3.22. This results in rejecting 99.28% of AMu background while rejecting only 1.41% of LLP signal (in simulation).

4.3 ΔCoG cut

Another result of the presence of the very bright tau lepton decay can be deduced from Figure 4.6. If one were to plot a cumulative distribution of these plots, a steady increase would be seen for AMu. For LLP events on the other hand, the majority of the charge would be collected only in the last part of the event[2]. Because of this different light emission pattern, the center of gravity (CoG) of the emitted light has a different time evolution.

The CoG of (a part of) an IceCube event is calculated in the same way the CoG of a distribution of point masses is calculated. The sum over all DOMs is performed and the collected number of PE in that DOM is used as its mass.

In the case of an AMu event, the CoG simply follows the track in a fairly smooth motion. For very declined tracks, the CoG shifts from string to string as muons passing close by a string deposit more light in its DOMs, keeping the CoG roughly there until the muons come close the next string. This “shift-pause-shift” motion lags behind the particles, but starts where the muons enter the detector and stops where they leave again.

For AMu events coming from very close to the Zenith, there is no “string to string” jump behaviour as the track moves down and stays close to the same strings throughout the entire event. Discrete DOM to DOM jumps are, due to scattering and absorption, only possible if the event is very close to one string. Even if no discrete CoG jumps can be distinguished, the situation is very similar to the declined case. First, the CoG shows where the muon bundle entered the detector; it then moves downwards until it reaches the point where the muons leave the detector.

[2]This feature in itself can not be used to reject AMu background as the light from the decay cascade takes a lot of time to be collected, leading to a long tail.

This behaviour is also there for LLP events before the tau lepton decays. The moment the tau lepton decays, this behaviour changes completely. The CoG jumps towards the decay position and roughly stays there[3]. After the tau decay, the CoG only wiggles around a bit due to random variations in the scattering and absorption of light that makes up the expanding sphere. Due to the very sparse nature of IceCube, this behaviour is very hard to quantify using reasonable time bins. It is harder still to differentiate between MC AMu and MC LLP based on this behaviour.

What one can do is looking at the shift in CoG not based on time but based on collected PE. Due to the i3 file structure, this requires more computing power than calculating the shift based on time. As mentioned in Section 3.1.1, the hits are stored in a library structure with an entry for every DOM. Every entry has a list of time ordered hits. To make this shift based op collected PE, it is necessary to make a cumulative distribution of all hits with only one hit per bin. This is of course not feasible.

A more realistic, but slightly more coarse, way to obtain this PE based CoG shifting is working in two steps. In a first iteration, a cumulative histogram is made with a very coarse bin width to indicate the time window in which a certain PE threshold is crossed[4]. Once the coarse time range is known, a finer histogram can be made of the correct time window using adequate precision.

This is done here dividing the hits in only two parts. The distance between the CoG of both halves (ΔCoG) is subsequently calculated. This parameter can easily differentiate between AMu and LLP events. For AMu events, the light deposition is fairly homogeneous along the track. Because of this, separating the event in two based on time or based on charge does not make a large difference; in both cases, the track is split in two roughly equally long parts. For both the first and second halve, the CoG of both parts is in the middle of the considered piece of track. ΔCoG therefore gives an indication of (half) the track length.

For LLP events, the situation is vastly different. Because a very large part of the detected light comes from the decay of the tau lepton, splitting the event in two based on time or based on collected PE results in two very different situations. Splitting a LLP event in two based on time can have different outcomes, depending on how long the lepton track is. With a very long track, the splitting will occur somewhere in the track. For very short tracks, the splitting will occur somewhere in the expansion phase of the cascade, after most of the light has been deposited in the DOMs closest to the decay. Splitting based on collected PE simply results in splitting somewhere in the cascade maximum.

ΔCoG for LLP events is expected to be very small, as both halves are dominated by the cascade maximum. However, the light deposited by the tau lepton also contributes to the CoG of the first half, shifting it somewhat towards the incoming direction. The cascade itself is slightly forwards peaked, shifting the CoG of the

[3]The CoG does not jump to the exact decay position due to the sparseness of the detector.

[4]The exact values for this bin width and the place where everything is calculated can be found in Appendix A.

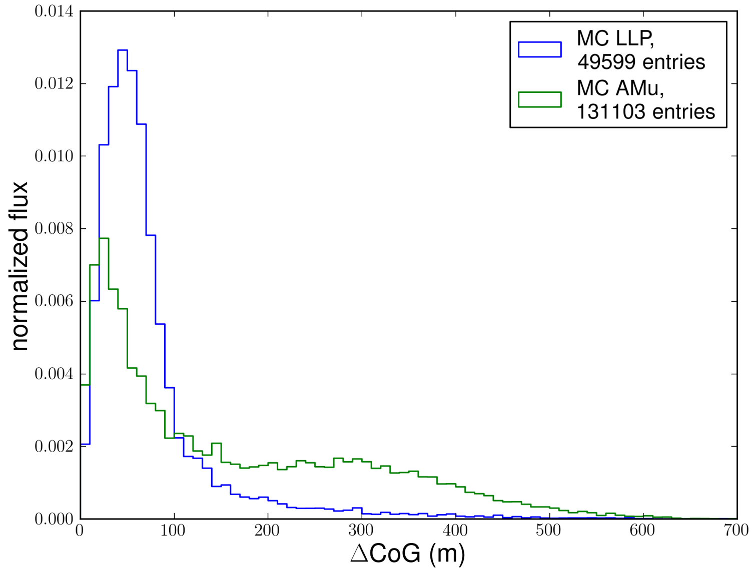

Figure 4.8: ΔCoG histogram for MC AMu and MC LLP events.

second half in the travel direction of the incoming neutrino. The finite volume of the detector also plays a role in the CoG position of the second half. If on one side of the cascade, light leaks out of the detector, light still gets detected on the other side of the cascade. This shifts the CoG of the second half towards the center of the detector.

The behaviour of ΔCoG for different event types described above is shown in Figure 4.8. The peak at low ΔCoG (~ 30 m) for AMu events is initially not expected. Rejecting a significant amount of AMu events is impossible using only this parameter. The spectrum of MC AMu events can however be explained and a solution is then readily found.

A low ΔCoG is not contradictory to a track like event: if there is only a short piece of track inside the detector, it is impossible for the CoG of the two halves to be far apart. The higher-than-average presence of those events becomes clear when the previous steps are considered. All events that made it into this histogram passed the EHE Filter, the altered Cascade Filter and the Peak Charge cut. Where the EHE Filter and the Peak Charge cut do not impose a shape on the event, the altered Cascade Filter does.

The parameters of the aCF are not very harsh, only very track like events get rejected. As explained in Section 4.1.3, the AMu events that pass this level are mostly corner clippers and events with a high energy stochastic energy loss. Figure 4.4 shows that there is a fairly large group of events with low line fit velocity and high Tensor of Inertia eigenvalue ratio. After application of the aCF, this becomes

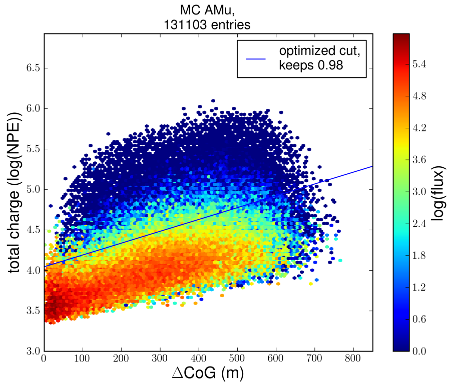

(a) ΔCoG vs. log(NPE) scatter plot for MC AMu. The flux is in arbitrary units.

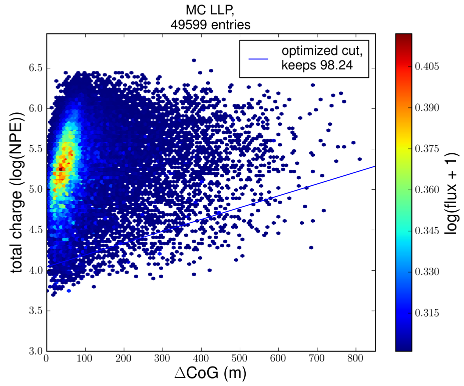

(b) ΔCoG vs. log(NPE) scatter plot for MC LLP. The flux is in arbitrary units.

Figure 4.9: The line on both figures is the optimized rejection line, events below the line are rejected from further analysis.

the main group.

Following this reasoning, the large AMu bins in Figure 4.8 are due to events that are only very shortly in the detector. As these events are in the detector for only a short time, they have less opportunity to deposit light in the PMTs. AMu events with a low ΔCoG should therefore also have a lower number of detected photo electrons (NPE).

This relation is also there for LLP events, although for another reason. A LLP event with a higher energy than another LLP event produce more light. In the first place, this is because on average, more energy is deposited in the decay cascade. In the second place, there is also a higher contribution from the track. A higher energy tau lepton typically travels a longer distance before it decays. Only part of this longer distance lies within the detector; but on average the visible track is longer. This leads to a larger light deposition in a direct way. With an increased energy, also the probability of stochastic energy losses increases. A stochastic energy loss along the tau track can considerably shift the CoG of the first half of the event, increasing the total ΔCoG.

In Figure 4.9, the CoG jump is plotted against the logarithm of the total amount of light collected in the detector (NPE) for MC AMu on the left and for MC LLP events on the right. The rejection line[5] is also indicated on both figures. The effects this cut has on the various background rates can be seen in Table 4.4.

Figure 4.9a confirms the behaviour of AMu events described above. For LLP events, there is a clear correlation between ΔCoG and log(NPE), this can be seen in Figure 4.9b. This correlation is to strong to be due to stochastic energy losses; in fact all events that do not follow this correlation (events with ΔCoG exceeding roughly

[5]The slope and intercept of this line can be found in Appendix A.

type	rejection rate	pre cut rate	post cut rate	post cut σ
AMu	99.62 %	$37.8 \cdot 10^3$	144	28
atm. ν_e	92.93 %	5.6	0.396	0.003
atm. ν_μ	98.33 %	33	0.55	0.02
astr. ν_e	31.04 %	8.28	5.71	0.02
astr. ν_μ	46.30 %	8.10	4.35	0.01
LLP	1.42%	0.141	0.139	0.001

Table 4.4: ΔCoG cut rejection rates. The rates are expressed in number of expected events per year.

200 m) are events in which the tau lepton had a high energy stochastic energy loss before it decayed. Also events where the neutrino interaction took place close to the detector contribute to this area. Even if only a small part of the light produced by the interaction cascade gets detected, this increases the ΔCoG significantly.

There is a very clear correlation between NPE in an event and the energy of the initial neutrino. As the y axis of Figure 4.9b is in a log scale, it actually goes over three orders of magnitude. The difference between LLP events with log(NPE) = 4 and log(NPE) = 6.5 is enormous, the neutrino energy in the second event can be hundred times the energy of the neutrino in the first event or more. The difference in ΔCoG over this huge range is only of the order tens of meters, which is very small compared to the difference in NPE. Because of the smallness of this effect, the increase of ΔCoG with increasing NPE can be due to the increased track.

4.4 High Gain cut

Next to making a PE spectrum with a fixed bin width, as is done for the Peak Charge cut, one can also make a PE spectrum with a fixed number of bins. In this second type of spectrum, the bin width is determined by the length of the event; it is defined as

$$\text{bin width} = \frac{t_{\text{last hit}} - t_{\text{first hit}}}{n_{\text{bins}}}. \tag{4.3}$$

In Equation 4.3, t_{hit} is the time of a hit and n_{bins} is the number of bins in the PE spectrum. A PE spectrum with a fixed number of bins has the advantage that every bin holds a fixed fraction of the event that is known in advance. This fixed fraction in every bin makes it easy to compare different events.

If an event were to emit light in such a way that the detection of photons is perfectly homogeneous, all bins would have the *average bin content*,

$$\text{average bin content} = \frac{\text{NPE}}{n_{\text{bins}}}. \tag{4.4}$$

However, no event has a perfectly homogeneous light detection over time, there will always be bins that fall below or exceed the average bin content. Bins that exceed

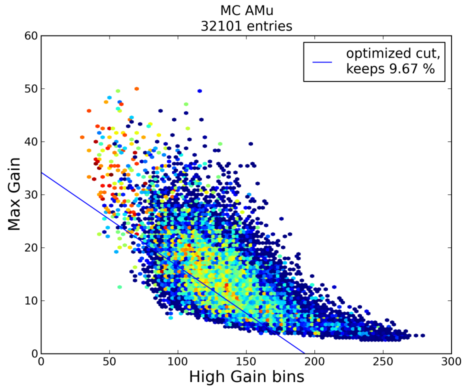

(a) High Gain vs. Max Gain scatter plot for MC AMu events using 500 bins. The colour coding represents the expected flux in arbitrary units.

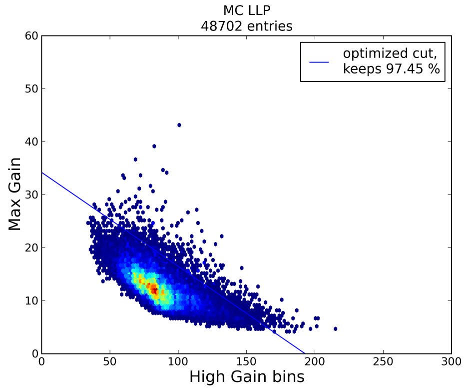

(b) High Gain vs. Max Gain scatter plot for MC LLP events using 500 bins. The colour coding represents the expected flux in arbitrary units.

Figure 4.10: The line on both plots is the optimized rejection line. Events that fall above the line are rejected from further analysis.

the average bin content are labelled “High Gain bins”. The number of High Gain bins can give information about the way light is deposited in the detector.

In an AMu event, the light is produced by Cherenkov radiation and stochastic energy losses. The energy losses give rise to a number of small and localised cascades along the track. In such an energy loss, a large amount of light is deposited over a couple of DOMs in a small amount of time. This leads to a high, short peak in the spectrum on top of the fairly constant Cherenkov radiation. The main source of light in an AMu event is a number of such energy losses, leading to a high number of High Gain bins.

Without the peaks in the spectrum, the average bin content would be level with the constant Cherenkov emission. The peaks that are superimposed on the Cherenkov emission are very thin, a single energy release does not have the required width to increase the average bin content by much. This results in a high *Max Gain*, i.e. the content of the highest bin expresses in units “average bin content”, for AMu events.

In a LLP event, almost all light comes from the decay of the tau lepton. The decay cascade is a very large one, it spreads over almost the entire detector. As the light travels away from the decay point, it becomes less intense. On the one hand, this is due to the geometric inverted square relation between point density on a sphere and the radius of that sphere. On the other, absorption of photons in the ice makes the light fade fade over distance. Notwithstanding these effects, the cascade remains very bright for a long time.

As the cascade is very bright for a long time, it increases the average bin content significantly. This increased average bin content reduces the Max Gain. Even though

type	rejection rate	pre cut rate	post cut rate	post cut σ
AMu	87.15 %	144	18.5	5.9
atm. ν_e	63.66 %	0.396	0.1439	0.0007
atm. ν_μ	79.09 %	0.55	0.115	0.007
astr. ν_e	16.64 %	5.71	4.76	0.02
astr. ν_μ	43.89 %	4.35	2.441	0.008
LLP	2.16%	0.139	0.136	0.001

Table 4.5: High Gain cut rejection rates. The rates are expressed in expected events per year.

the highest bin of a LLP event probably has much more PE than an AMu event, the LLP event has a lower Max Gain.

Because of the high average bin content, only very few stochastic energy losses of the tau lepton will deposit enough energy in the detector to exceed the average bin content. Also a part of the tail of the decay cascade will be below average bin content. This leads to a small number of High Gain bins.

In Figure 4.10, the number of High Gain bins and Max Gain are plotted for MC AMu and MC LLP events. Even though the events of both groups are not as nicely separated as initially hoped, the predicted behaviour is there. LLP events start and finish at a lower number of High Gain bins than AMu events. In the region where both LLP and AMu events are present, LLP events have a lower Max Gain than AMu events for the same number of High Gain bins. The exact rejection rates can be seen in Table 4.5.

4.5 Comparison to data and non-AMu background

All of the cuts described above have been optimized using Monte Carlo simulations. It is relevant to check if the parameters on which the rejection decisions are based are based on real physical effects or if the found differences are simply due to Monte Carlo artefacts. In the case of an artefact, a cut can not be used. This check is done using the *burn sample*, a limited fraction of data that is freely available for researchers to prove that their analysis works. Only when this is done, the entire data set can be used. In this analysis, optimization happened using detector simulation in the IC79 configuration (the 2010 - 2011 season). The IC79 burn sample consists of 780 hours and 55 minutes of data taken between June 2010 and May 2011.

Figure 4.11 shows the expected fluxes at the different cut levels for each type of Monte Carlo simulations and for data. The large difference between the burn sample and the summed MC background before the EHE Filter is explained by the choice of files. The number of analysis that uses only data that passed the EHE filter is significant. The IceCube collaboration therefore provides files that contain only events that passed the EHE Filter. These files were used here. The differences between MC and data at the other levels are not as readily explained. Various

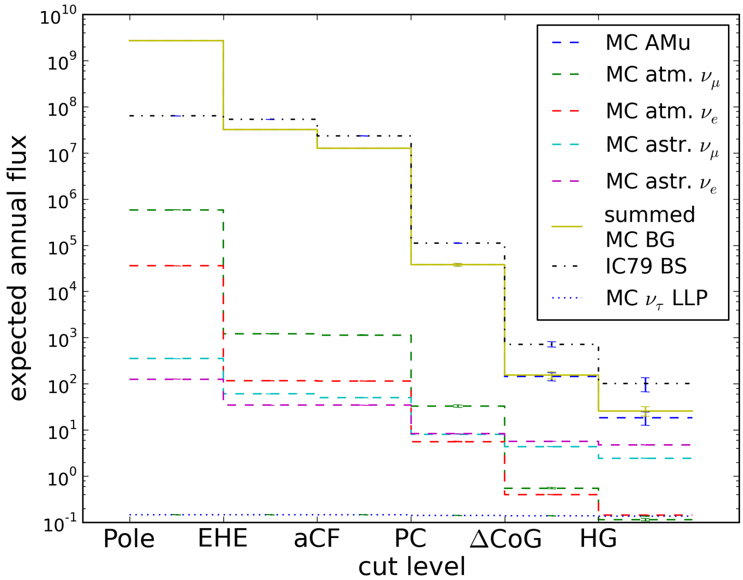

Figure 4.11: The expected fluxes at every cut level for every type of background individually (dashed lines) and summed (full line) using MC, the expected signal (dotted line) using MC and the IC79 burn sample (dashed-dotted line).

elements could be responsible for this.

The difference between the measured and predicted flux right after the EHE Filter suggests that there might be a problem with the event weighting. Both sets of events are provided by the IceCube collaboration and are at that point not yet influenced by this analysis. Event weighting is not a simple task, as was made clear in Section 3.2.3. The subject was only briefly handled but various ambiguities became already apparent.

In this analysis, systematic errors have never been considered. For example DOM efficiency (the efficiency with which a DOM detects an incident photon) and the used ice model (the local variation of absorption and scattering parameters) play a major role in the detector output. Both these subjects were taken for granted in this thesis.

It is also possible that the cuts proposed here are Monte Carlo artefacts and do not stand on a physical difference between the various event types. If this would be the case, not only the absolute predicted flux would be different, also the rejection rates of the flux would be different.

In Table 4.6, the rejection rates for the summed Monte Carlo background and for the burn sample are presented. Except for the High Gain cut, none of the burn sample rejection rates corresponds with their Monte Carlo counterpart. The rejection rates of the Peak Charge cut and the ΔCoG cut are however in the same

type	EHE Filter	aCF Filter	PC cut	ΔCoG	HG cut
BS	/	56.02 ± 0.04	99.521 ± 0.004	99.36 ± 0.08	86 ± 6
MC	98.819 ± 0.005	60.3 ± 0.1	99.70 ± 0.02	99.59 ± 0.08	83 ± 5

Table 4.6: Comparison of the rejection rates of the different introduced cuts for data (BS) and the summed simulation (MC), expressed in %.

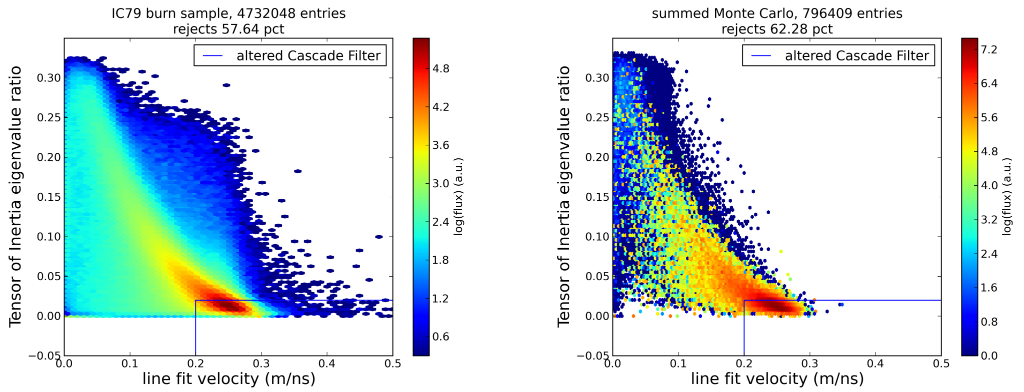

(a) Cascade Filter parameters scatter plot for the IC79 burn sample. The flux is not normalized.

(b) Cascade Filter parameters scatter plot for all MC simulated background combined. The flux is in arbitrary units.

Figure 4.12: On both cuts, the altered Cascade Filter rejection line is plotted. Events that fall below the line are rejected from further analysis.

ballpark, adding systematic errors might make them equivalent.

4.5.1 Altered Cascade Filter

The rejection rate for the altered Cascade Filter is further off than any other cut. In Figure 4.12, the Cascade Filter parameters are plotted for both the burn sample and for the combined simulation. For the simulation plot (Figure 4.12b), only 10% of the used data has been plotted. This explains the difference between the rejection rate in Table 4.6 and the one displayed in Figure 4.12b.

There is a clear difference between data and Monte Carlo on Figure 4.12. There are parts of the $ToI_{eval.ratio}$-lfv plane that are covered by the burn sample but not by Monte Carlo. Most of these areas are not rejected by the altered Cascade Filter, leading to a lower rejection ratio.

4.5.2 Peak Charge cut

For the peak charge cut, the rejection ratio of data and Monte Carlo are very similar. If one compares the Peak Charge histograms for data and Monte Carlo, these are very hard to differentiate. These are plotted in Figure 4.13. It is plausible that the difference between the rejection rates is due to systematic errors that were not included in this analysis.

Both data and Monte Carlo display a bump in histogram slightly below three. This is due to the combined effect of all four remaining sources of background. The histograms for these sources individually can be found in Appendix B, the histogram of the summed Monte Carlo simulations without AMu events is displayed in Figure 4.14. The peak right before three can be identified.

4.5.3 ΔCoG cut

Also for this cut, there is very little difference in the rejection rate of data and Monte Carlo simulation. Comparing a ΔCoG-NPE scatter plot starts loosing its functionality as there are only a limited number (10933) of events left[6]. At this point, the contribution of AMu events is still three orders of magnitude higher than any other source of background, the burn sample plot should therefore be almost identical the AMu scatter plot (Figure 4.9a). It can be seen in Figure 4.15a that this is the case.

The events in Figure 4.15b that are in the upper right corner are due to atmospheric and astrophysical muon neutrinos, this can be seen in Figure 4.16. This makes sense as an interacting muon neutrino has almost exactly the same layout as a LLP event, only the brightness of the track is higher. The large difference is the time at which everything happens. For a LLP event, the track comes in first and the decay cascade is last. For a muon neutrino event, the interaction cascade is first and the track leaves. The ΔCoG cut does not take this sort of time information into account. For this cut, a LLP event and a high energy muon neutrino event are the same.

In Figure 4.16, there is also a fairly strong trend towards higher ΔCoG, much like AMu events. This behaviour can easily be explained, both AMu events and muon neutrino events end with a muon travelling through the detector. Muon neutrinos that interact within the detector but have a lower energy than the typical LLP energy will have a dimmer cascade than higher energies. If this cascade is of the same magnitude of a high energy stochastic energy loss, parameters for this cut will be indistinguishable from an AMu event.

Also electron neutrinos behave as expected. An interacting electron neutrino produces an interaction cascade and an electromagnetic cascade on the same position. ΔCoG for such an event should be very small, independent of the number of collected PE. This behaviour can be seen on Figure 4.17.

[6]Optimization of the cuts was performed using the complete 7017 simulation. For this comparison section, only 10% of that simulation is used.

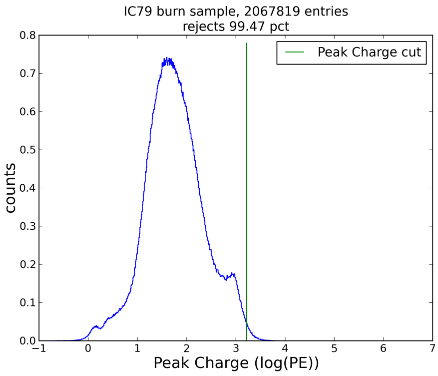

(a) Peak Charge histogram of the IC79 burn sample. The flux is normalized.

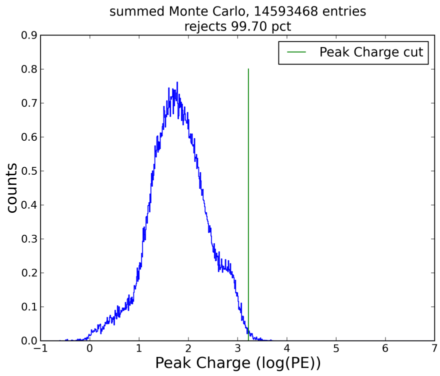

(b) Peak Charge histogram of combined Monte Carlo. The flux is normalized.

Figure 4.13: On both cuts, the Peak Charge cut rejection line is plotted. Events that fall below the line are rejected from further analysis.

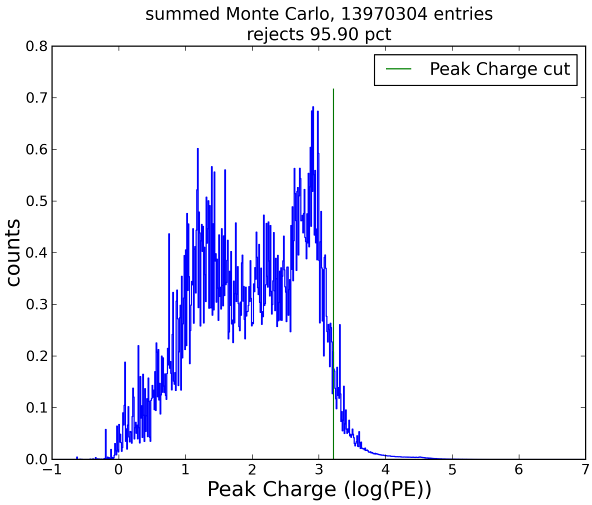

Figure 4.14: Peak charge histogram of MC background without AMu contribution. The histogram is normalized.

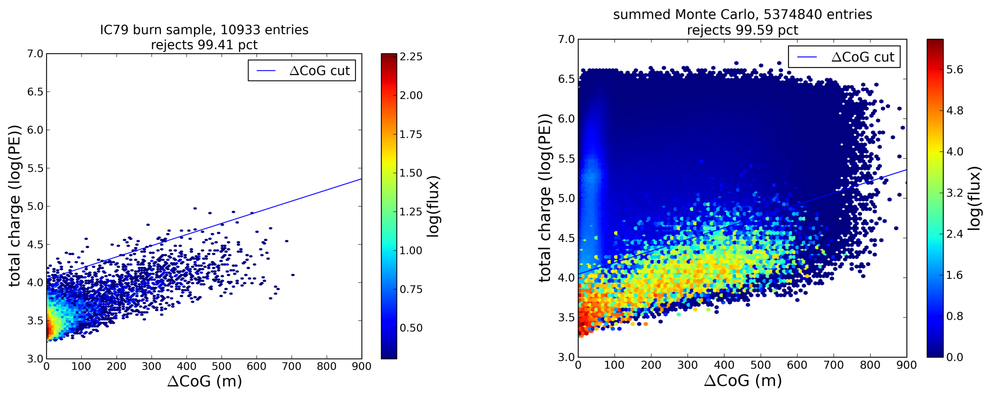

(a) Burn sample scatter plot of the ΔCoG cut parameters. The flux is not normalized.

(b) Monte Carlo scatter plot of the ΔCoG cut parameters. The flux is not normalized.

Figure 4.15: On both cuts, the ΔCoG cut rejection line is plotted. Events that fall below the line are rejected from further analysis.

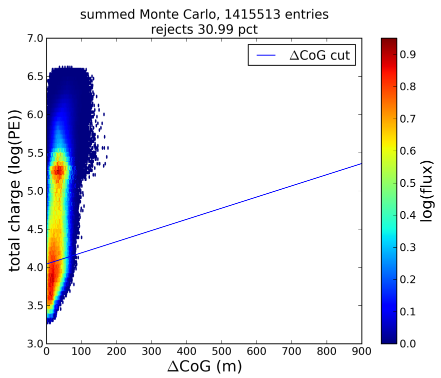

Figure 4.16: Scatter plot of ΔCoG cut for astrophysical electron neutrinos.

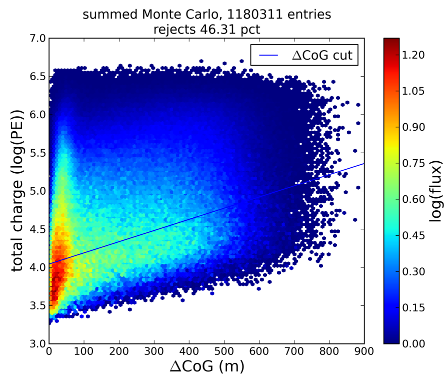

Figure 4.17: Scatter plot of ΔCoG cut for astrophysical muon neutrinos.

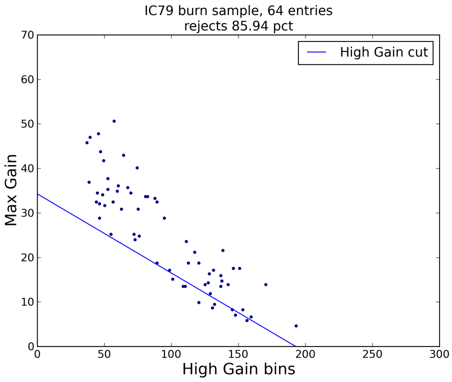

(a) scatter plot of the HG cut parameters of the remaining events in the IC 79 burn sample.

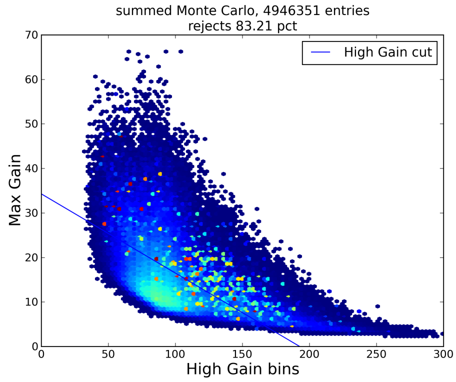

(b) scatter plot of the HG cut parameters of the remaining events in the summed Monte Carlo sample.

Figure 4.18: The line on both figures is the rejection line, only events that fall below this line are kept for further analysis. The line was optimized for rejection of MC AMu events.

In both Figure 4.16 and Figure 4.17, the astrophysical component is plotted. As was mentioned in Section 3.3, the files are the same, only the weighting is different. As a result, the same events are present in an astrophysical and an atmospheric plot. For both figures mentioned here, the difference is that events with lower NPE have higher weights for atmospheric neutrinos.

4.5.4 High Gain cut

The High Gain cut is the only cut where the summed Monte Carlo rejection rate is consistent with the burn sample rejection rate. It is also the only cut for which the variance on the rejection rates for both the burn sample and for MC exceed 0.1%. In any case, there are only 9 events left in the burn sample after this cut. These events are plotted in Figure B.11.

If one compares a scatter plot of the High Gain cut parameters of the burn sample (Figure 4.18a) and the combined Monte Carlo simulation (Figure 4.18b), it is clear that the Monte Carlo covers a much larger area than the burn sample. This is partially because there are much more MC events than there are true events. In Figure 4.19b, the HG cut parameters are plotted for MC non-AMu events, Figure 4.19a is plotted again as a reminder. It is clear that the non-AMu Monte Carlo events cover a much larger area of the parameter plane.

It is normal that the non-AMu background contributions, i.e. atmospheric and astrophysical ν_e and ν_μ, are close to the behaviour of ν_τ LLP events. As explained in the previous section, ν_μ events are very similar to LLP events. Almost the only

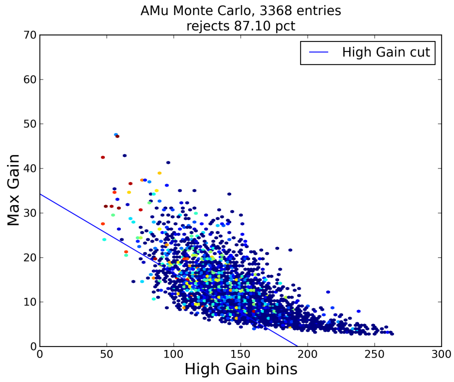

(a) scatter plot of the HG cut parameters for MC AMu events

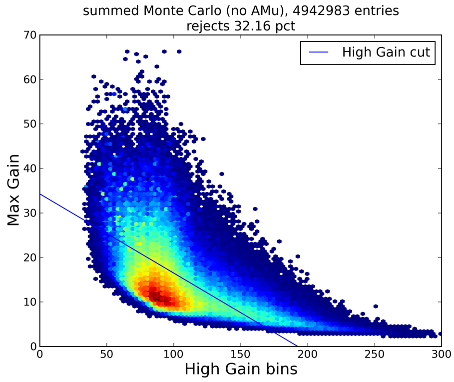

(b) scatter plot of the HG cut parameters for MC non-AMU BG events

Figure 4.19: The line on both figures is the rejection line, only events that fall below this line are kept for further analysis. The line was optimized for rejection of MC AMu events and conservation of ν_τ LLP events.

way to differentiate between a LLP a ν_μ event is based on time[7]. In this cut, time is again not considered. Muon neutrinos therefore can easily pass this cut.

Also electron neutrinos can easily pass this cut. An electron neutrino is only one big cascade. The entire first part of the event will be High Gain bins, only the tail of the expanding cascade will not be above the average. Because so much light is deposited, the cascade remains very bright for quite some time, giving a lot of DOMs a lot of charge over a long period. Because of this, the Max Gain will be rather low.

[7]Also comparison of the brightness of the track and the cascade can be done, but using time will be much easier.

Chapter 5

Conclusion and outlook

The IceCube Neutrino Observatory has a twofold purpose. IceTop is a square kilometre cosmic ray observatory and IceCube is a cubic kilometre neutrino telescope. With IceCube, atmospheric and astrophysical neutrinos can indirectly be detected if they interact within the detector. A high energy (100 GeV and higher) neutrino interaction produces relativistic secondary charged particles. These particles produce Cherenkov light as they travel through the ice; it is this light that gets detected by the IceCube DOMs.

Neutrinos are not the only source of charged particles in the IceCube detector. When a highly energetic charged particle coming from outer space interacts in the Earth atmosphere, it creates an extensive air shower. An extensive air shower has an electromagnetic, muonic, hadronic and neutrino component. The electromagnetic and hadronic component do not penetrate the ice, only muons and neutrinos do. The neutrinos produced in extensive air showers are a part of the physics goals of IceCube, these are the atmospheric neutrinos. The muons are of no interest to IceCube, but they do deposit light in the detector. Annually, about 2.7 billion events are caused by muons from extensive air showers, this is the main background to most analysis.

In this thesis, a search for tau neutrinos in the Lollipop detection channel is performed. Also for this analysis, muons produced in extensive air showers are the main background. This thesis consists of finding patterns in simulated detector output that are as dissimilar as possible for Lollipop and muon simulation. Once a pattern is found, it has to be tested on real IceCube data to test if it is a real effect or a Monte Carlo artefact. For this, the IC79 burn sample is used.

Several patterns were found to be different between Lollipop events and cosmic ray muon events. As the amount of detected PE is highly correlated with the energy of the event, the first difference is simply an energy consideration. Muons that pass through the detector range from barely visible to very bright whereas Lollipop events are only very bright. Using the EHE filter reduces the background rate with 98.82% while reducing the data rate with only 0.013%.

A second difference is based on the topology of the track. Muons leave a long track in the detector whereas Lollipops have a track and then a huge cascade. This differentiates the eigenvalues of the tensor of inertia for both event types. The eigenvalue ratio of a track like event is much lower than that of a cascade like event. Combined with the line fit velocity (which is c for a perfect track and 0 for a perfect cascade), this allows to reject all the near perfect muon tracks (60.26%) while keeping all but the highest energy Lollipop events (rejecting only 0.19%). Both of these parameters are calculated for the online Cascade Filter in the IC79 detection season and are therefore readily available.

The third difference focusses on the decay cascade of a Lollipop event. This cascade deposits an enormous amount of light in the detector in a very short amount of time. Splitting the event up in 100 ns bins and requiring $10^{3.22}$ PE to be collected in the brightest bin is a good lower limit for the brightness of a LLP decay cascade. This requirement also doubles as increased energy filter. To pass the EHE filter, only 10^3 PE is required to be collected over the entire event. This new, increased requirement removes 99.70% of the background events while reducing the signal with only 1.96%.

For the fourth difference, a cascade is again required. As the background of cosmic ray muons is still by far the largest, this cut is designed specifically to reject those events. The distance between the CoG of the first and second halve of the collected charge is very small for events whose main light contribution is a cascade; this is not the case for events without cascade. Because of the finite size of IceCube, not all tracks travel the same distance in the equipped volume. Events that have a long path within the detector have a large CoG difference and produce a lot of light in the detector as well. Events that travel only a short distance through the detector have a smaller CoG distance but produce less light within the detector than a longer track of similar energy. Setting a minimum NPE for every ΔCoG results in a 99.59% background reduction at a cost of only 1.76% signal.

The fifth and final difference of this thesis focusses on the way light is collected. Splitting an event in a fixed number of bins allows easy comparing of the fractions of an event with another event. Collecting the majority of light in small bursts leads to a lot of bins that collect more light than the average bin while keeping the peak of the highest bin high compared to the average. Collecting most of the light in a single cascade while also having a piece of track results in a limited number of bins that exceed the average bin. Also the value of the highest bin is relatively low compared to the average bin. Rejecting events with a high Max Gain or a high number of High Gain bins reduces the total background with 83.29% and the Lollipop signal with 2.16%

The predicted MC flux is not consistent with the behaviour of the burn sample. Even though no systematic errors are taken into account, it seems unlikely that the predicted and the measured rate will be consistent. Despite the fluxes being different, the rejection rates are similar. For the High Gain cut, data and Monte Carlo are consistent. For the Peak Charge cut and the ΔCoG cut it seems plausible that the rejection rates for data and Monte Carlo will be consistent if systematic errors are taken into account.

For the altered Cascade Filter, considerable differences between data and Monte Carlo simulations were found.

After one year of work, the background was reduced from $2.69 \cdot 10^9 \pm 0.01 \cdot 10^9$ event per year to 25.9 ± 5.9 events per year. This is however still two orders of magnitude higher than the expected signal (which reduced from 0.145 to 0.136 expected events per year). Further analysis is therefore still needed.

From the burn sample, nine events were not rejected by the proposed cuts.

So far, seven parameters have been considered to optimize four cuts. The optimization of these cuts happened cut by cut and was very stringent on not removing to much signal. Links between the parameters of the different cuts have not been investigated, it is not unimaginable that more connections can be found there.

No attempt has been made to reconstruct the energy of a Lollipop event, this also still has to be done. This can be done using modules such as Millipede. A seed for Millipede is prepared and ready for use.

In the appendices, an overview of failed or unfinished ideas to differentiate Lollipop signal from background events is given. More inspiration to further reduce the background can be found there.

Appendices

Appendix A

Computation

In this appendix, the computation of the various cuts is explained. Also the program structure and the error calculation will be explained shortly.

A.1 Cuts

For the EHE Filter and the altered Cascade Filter, no calculations were done. They are not discussed here.

A.1.1 Peak Charge Cut

The Peak Charge is calculated using a root TH1F histogram with a bin width of 100 ns. The number of bins is chosen such that the first hit falls in the first bin and the last hit in the last bin. The Peak Charge is than simply the logarithm of highest entry.

The cut is then performed by checking if the found value exceeds the required value of 3.22. If the found value is less than 3.22, the event is rejected.

A.1.2 ΔCoG cut

To calculate the ΔCoG, first the Half Charge time is estimated to a 100 ns precision using a root TH1F histogram. In a second iteration, a TH1F histogram with 1 ns is created but only for the time range that was estimated with the previous histogram. This allows determination of the Half Charge time to 1 ns precision. Next, the CoG for both halves is calculated.

The CoG is calculated as the charge weighted average position of all ATWD hits. ΔCoG is then simply calculated as the distance between the CoG of the first and second half. log(NPE) is calculated summing the charge of all ATWD hits, excluding DeepCore, and taking the logarithm.

The cut is then performed by checking if $\log(\text{NPE}) > 4.03747201 + \Delta\text{CoG} \cdot 1.36917225 \cdot 10^{-3}$. All events that fail this test are rejected.

A.1.3 High Gain cut

The High Gain cut is calculated with a 500 bin histogram. First, the exact bin width is calculated, only then the histogram is filled. A python array with 500 entries is used for this task. Once the histogram is filled, every entry is divided by the total NPE so that every bin holds the fraction of the event and no absolute number of PE.

To count the number of High Gain bins, a loop is performed over the histogram to check if a bin holds more than the average. In this same loop, the highest bin is selected. Afterwards, conversion to Max Gain is performed.

All events for which Max Gain $> 34.2892805 - 0.17787058\cdot$ (number of High Gain bins) are rejected from further analysis.

A.2 Program structure

For the clarity of the analysis, the different cuts are calculated in separated files. Several cuts require however multiple loops over all hits. To minimize the total number of loops in the analysis, calculation of the parameters in a cut is sometimes spread over several files. In this section, what is calculated in each file is explained.

A.2.1 Level4.py

Level4.py contains two loops over all hits: the first is to find the first and last hit so that the appropriate range for a hit histogram can be selected, the second to fill this histogram. In the first loop, also the total number of PE is counted (excluding DeepCore).

In the second loop, two histograms are constructed. Both histograms have the same bin width (100 ns) and number of bins (the number depends on the event length). One histogram is filled with the hits from the centre of the detector, the other histogram holds the hits from the edge of the detector. The Peak Charge is calculated from the first, central, histogram.

The two histograms are then combined to find the time range in which the threshold of half the total collected charge is exceeded. This is needed for the accurate calculation of ΔCoG.

A.2.2 Level5.py

Using the time range calculated in level4.py, a histogram with 100 bins of 1 ns width is created in this time range. During the first of two loops in level5.py, this histogram is filled. The moment half the charge has been detected is the “Half Charge time”. In the second loop, the position of the CoG of both halves and the distance between those positions is calculated. Combined with the total log NPE that was calculated in level4.py, a decision is made about the event.

Also in level5.py, some approximations of the decay time and positions are calculated. These can be used as seed for modules such as Millipede. This can later be used to calculate the energy of the event. When this seed is used in Monopod, a very good decay position is obtained (on average 14 m away from the Monte Carlo Truth).

A.2.3 Level6.py

Level6.py contains two loops over all hits. In the first loop, the time of the first and last hit are determined[1]. In the second loop, the number of High Gain bins and Max Gain is calculated. Next, the event is either rejected or kept for further analysis based on the cut criteria.

[1]This loop can be avoided by writing the first and last hit time in the frame in Level4.py.

Appendix B

Additional plots

In this chapter, additional plots are given. First, energy and zenith distributions of all MC primaries are given. The azimuth distribution is not given, as this is homogeneous for all primaries. Second, different cut parameters for all MC primaries are given. Third, a steamshovel reconstruction of the nine events from the burn sample that survived all cuts is given.

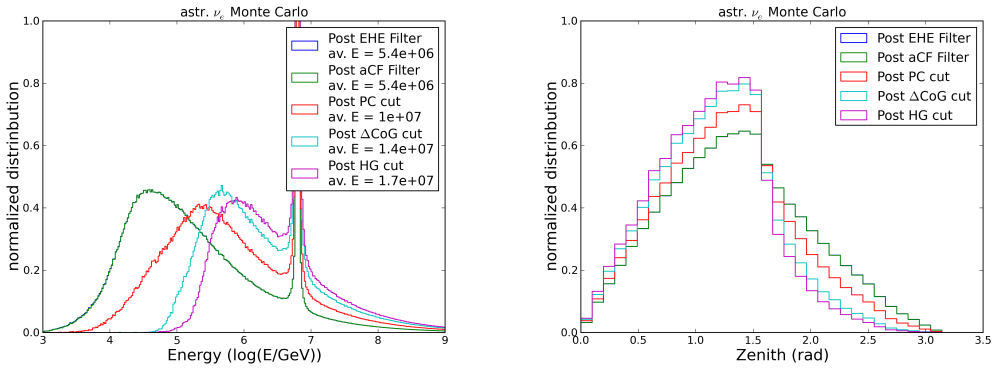

(a) astr. ν_e energy distribution (b) astr. ν_e Zenith distribution

Figure B.1: The increasing opacity of the earth with increasing neutrino energy can be seen. The peak slightly below 10^7 GeV is a MC artefact that only occurs for electron neutrino simulation. This makes the displayed average energy incorrect. It can still be seen that the energy increases with increasing cut levels.

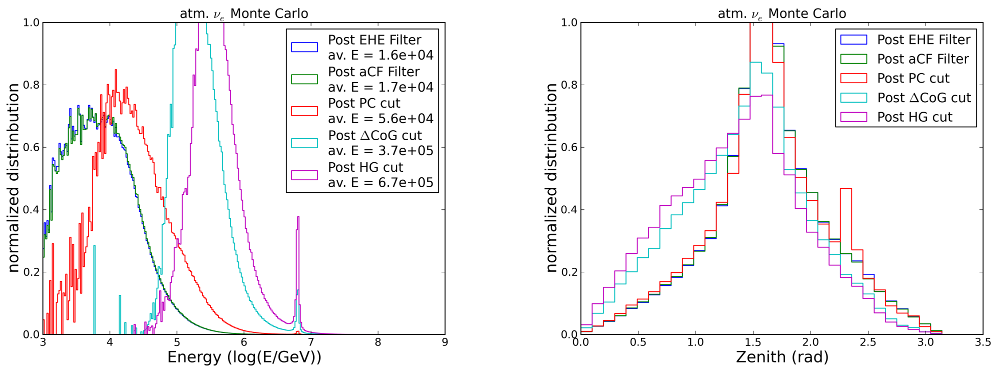

(a) atm. ν_e energy distribution (b) atm. ν_e Zenith distribution

Figure B.2: It can clearly be seen that both the Peak Charge cut and the ΔCoG cut places a hard energy requirement on the event by requiring a certain amount of PE. This can also be seen from the decrease in events coming from below the horizon after these cuts.

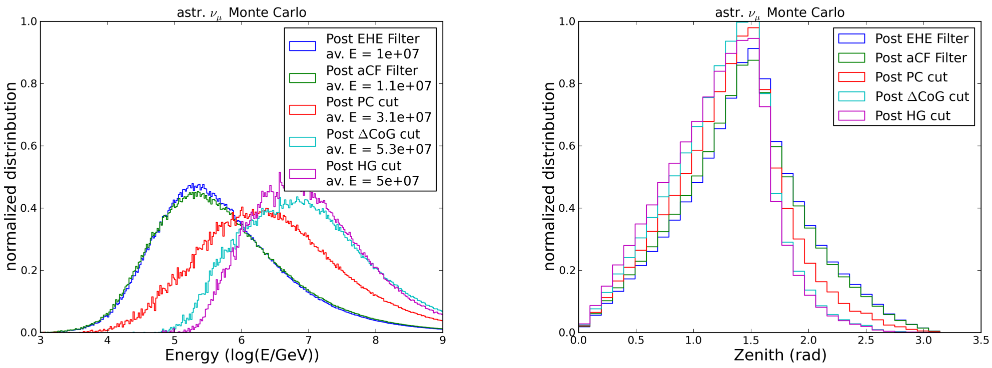

(a) astr. ν_μ energy distribution

(b) astr. ν_μ Zenith distribution

Figure B.3: Here as well, it can be seen that the average energy increases after every cut (except for the High Gain cut, which does not affect some muon neutrino interaction topologies).

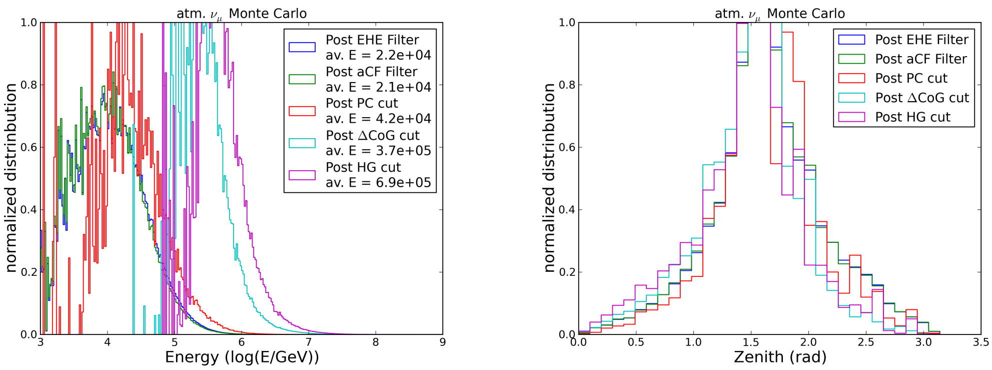

(a) atm. ν_μ energy distribution

(b) atm. ν_μ Zenith distribution

Figure B.4: The effects that are visible for atmospheric electron neutrinos are also visible here, but are less clear.

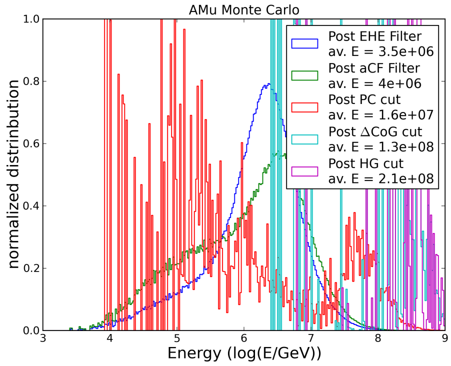

(a) AMu energy distribution

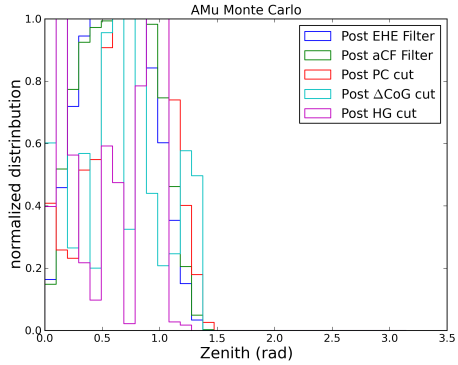

(b) AMu Zenith distribution

Figure B.5: It is clear that cosmic ray muons can only come from above the horizon. This can also be seen on the right figure. The ugly energy histogram is due to a lack of statistics (only 10000 simulation files were used to make these plots). Despite the bad statistics, it is clear that the average energy of an event increases with the cut level. No real trend can be assigned to the directional behaviour.

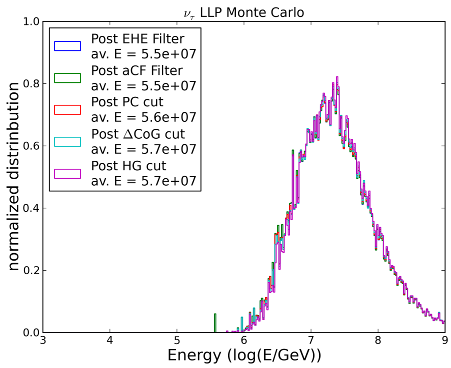

(a) ν_τ LLP energy distribution

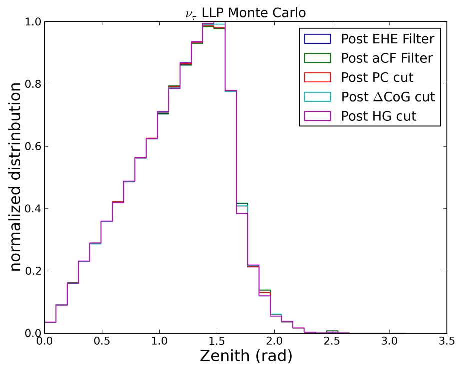

(b) ν_τ LLP Zenith distribution

Figure B.6: It can clearly be seen that IceCube is only 2π sensitive to LLPs. To much energy is lost in the regeneration process to allow LLP signatures to happen. From the energy histogram, it becomes clear why all previous cuts do not affect the LLP events. From the displayed average energies, it is clear that all cuts have some sort of implicit energy requirement. As the average energy of a LLP event is already very high, they easily pass these tests.

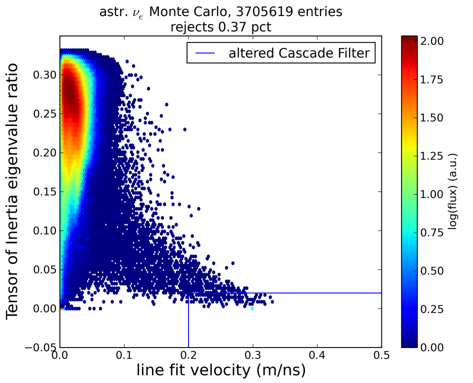

(a) altered Cascade Filter parameters

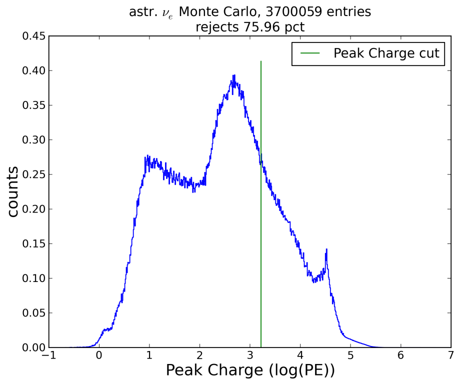

(b) Peak Charge cut parameters

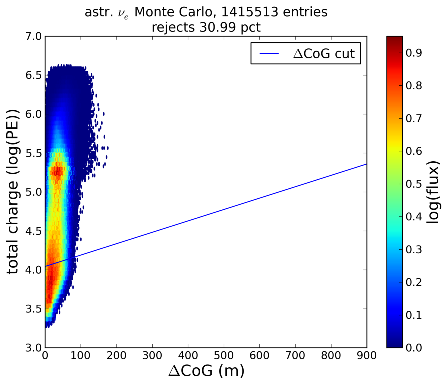

(c) ΔCoG cut parameters

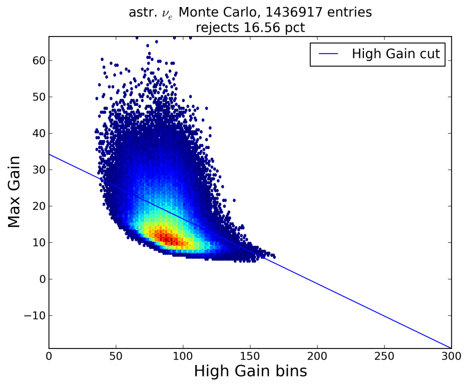

(d) High Gain cut parameters

Figure B.7: astr. ν_e cut parameters

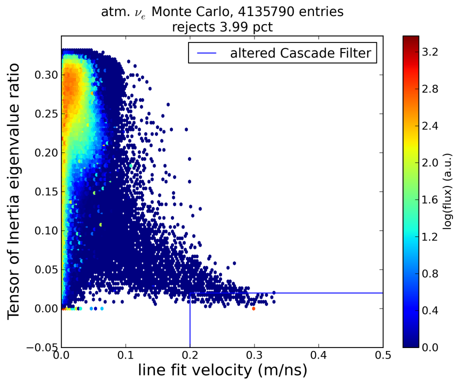

(a) altered Cascade Filter parameters

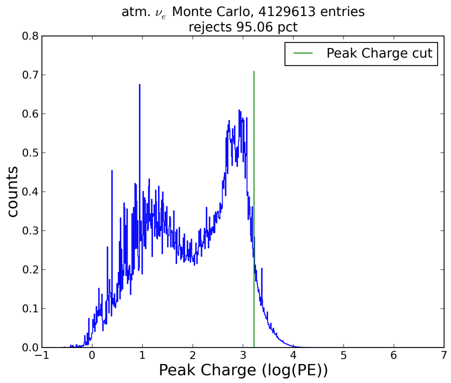

(b) Peak Charge cut parameters

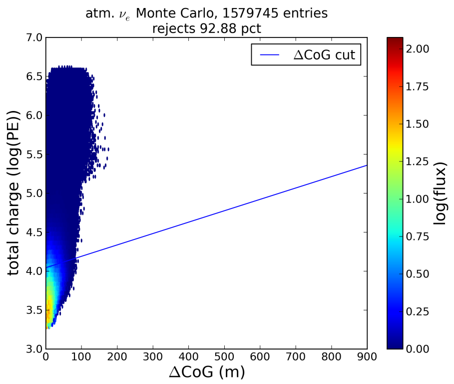

(c) ΔCoG cut parameters

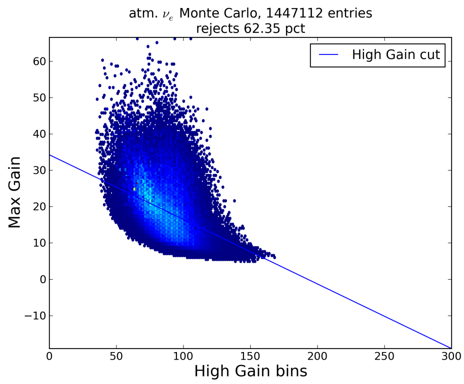

(d) High Gain cut parameters

Figure B.8: atm. ν_e cut parameters

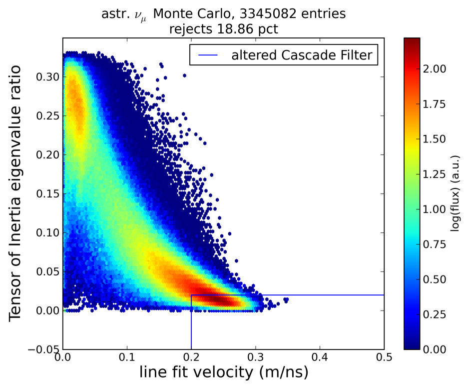

(a) altered Cascade Filter parameters

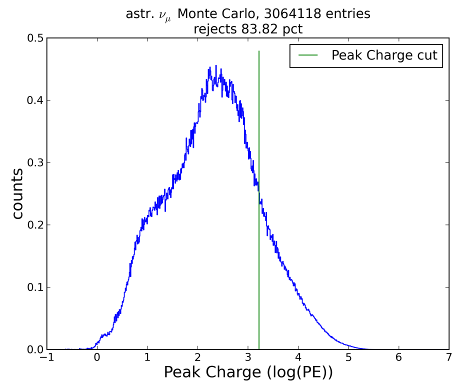

(b) Peak Charge cut parameters

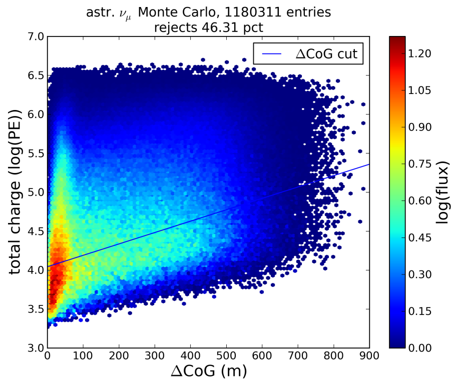

(c) ΔCoG cut parameters

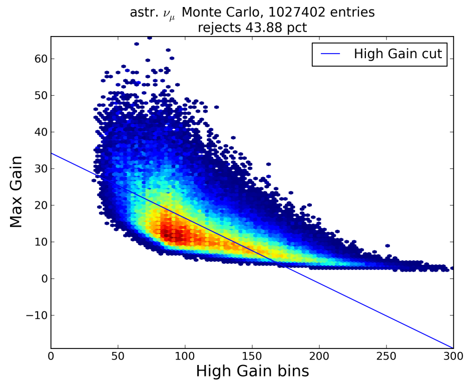

(d) High Gain cut parameters

Figure B.9: astr. ν_μ cut parameters

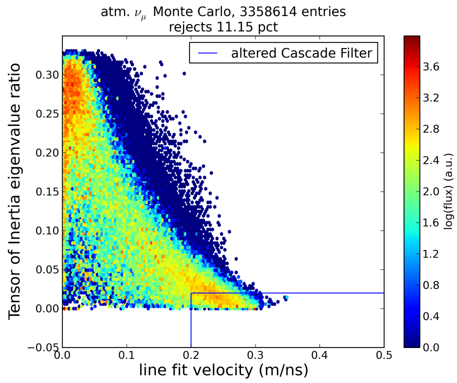

(a) altered Cascade Filter parameters

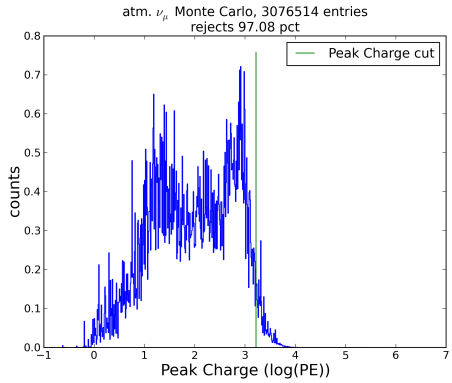

(b) Peak Charge cut parameters

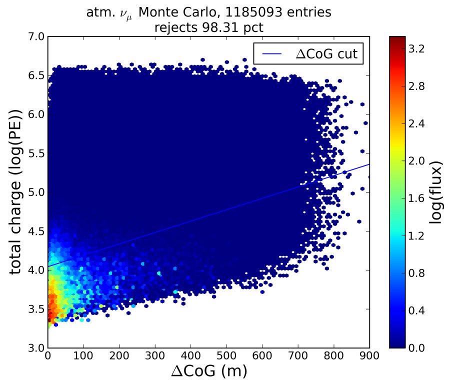

(c) ΔCoG cut parameters

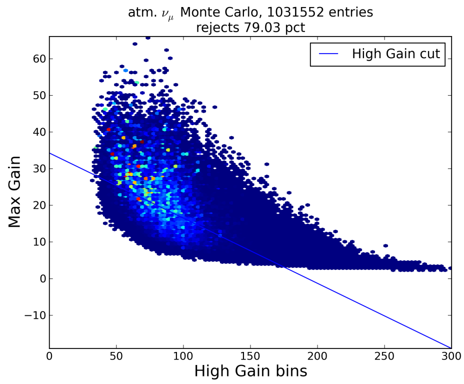

(d) High Gain cut parameters

Figure B.10: atm. ν_μ cut parameters

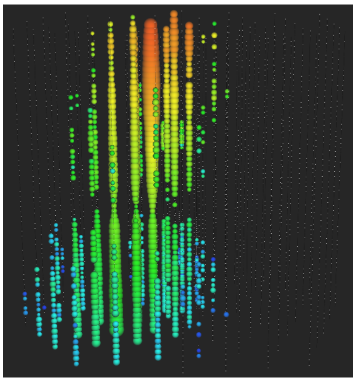

(a) runID: 116560, eventID: 11552477

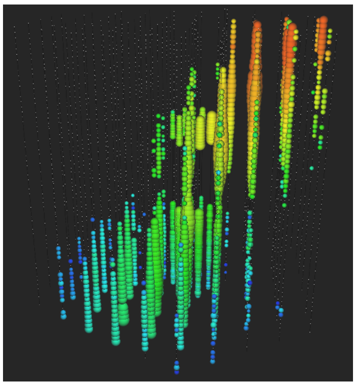

(b) runID: 116720, eventID: 33577584

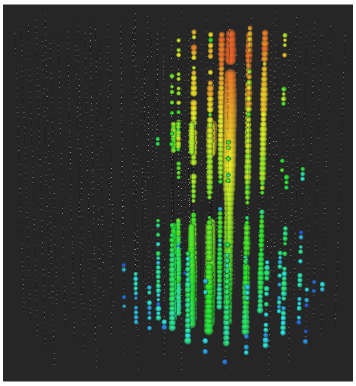

(c) runID: 116890, eventID: 50738365

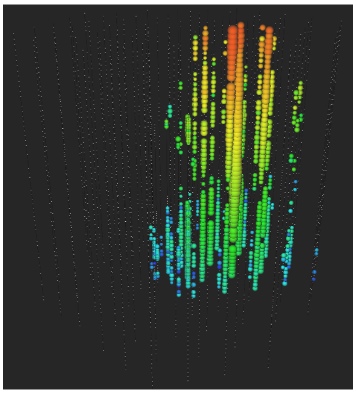

(d) runID: 117210, eventID: 6983440

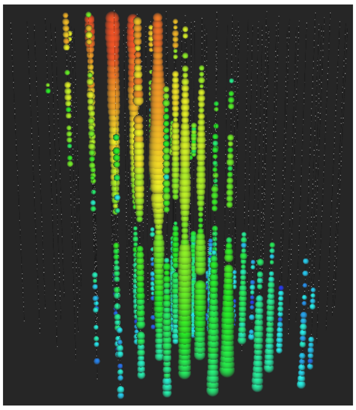

(e) runID: 117260, eventID: 48056868

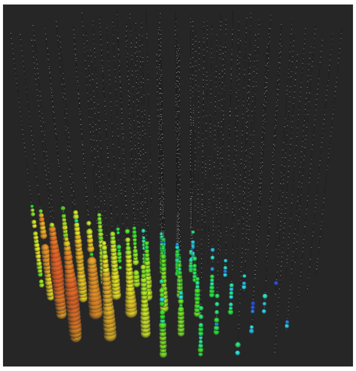

(f) runID: 117700, eventID: 8097613

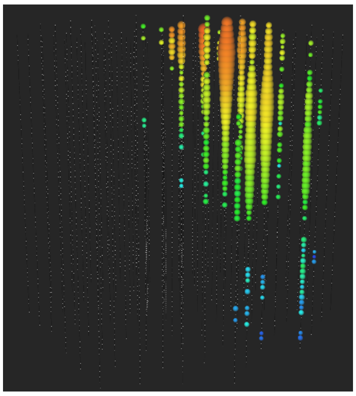

(g) runID: 117810, eventID: 37751601

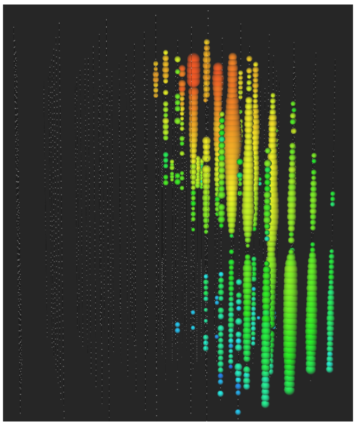

(h) runID: 117900, eventID: 27511524

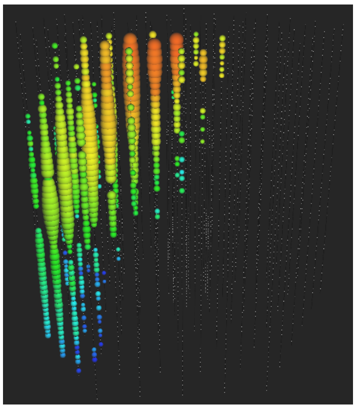

(i) runID: 117940, eventID: 35990074

Figure B.11: The nine remaining events in the burn sample.

Appendix C

Rejected and unfinished ideas

C.1 Rejected ideas

- loneliness: the ratio of the highest peak over the second highest peak. AMu events are fairly homogeneous in their light emission, so the second highest peak should not be much lower than the highest peak. LLP events on the other hand have one huge peak that dwarves al the other peaks. The determination of peaks however was not that straightforward. Using the root histogram functions did not give a good result, searching in this direction was abandoned.
- using Monopod/Millipede to discriminate LLP from AMu was not as straightforward as it initially seemed. This was only attempted late in the year, more thorough research might give more results.

C.2 Abandoned but not rejected ideas

- up-down ratio. Simply looking at the distribution of charge above and below the reconstructed decay position. For LLP, this is heavily z-dependent but follows a nice correlation. Therefore, this needs a good decay position reconstruction in order to work. At the time, that was not yet available. AMu events do not follow this correlation.

- The spherical-ness of the event. Plotting the theta and phi of every hit DOM with respect to the reconstructed decay position yields for LLP simulation a map that is fairly homogeneous (taking into account the finite volume of the detector). This is far more polarized for AMu events that form a track. No sufficient algorithm was found to express how homogeneous a map is.

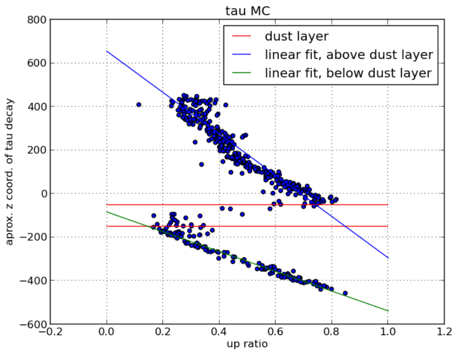

(a) up down ratio for LLP

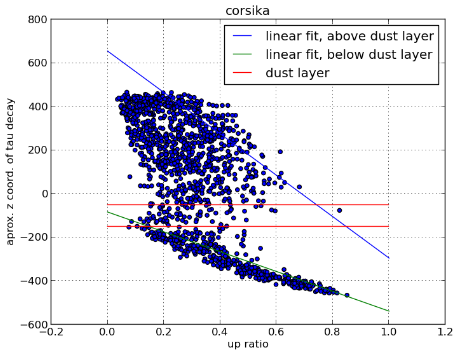

(b) up down ratio for AMu

Figure C.1: up down ratio for MC LLP and MC corsika, the dust layer is nicely visible on both plots (also indicated in red)

Bibliography

[1] F. Englert and R. Brout. Broken Symmetry and the Mass of Gauge Vector Mesons. *Phys.Rev.Lett.*, 13:321–323, 1964.

[2] Peter W. Higgs. Broken Symmetries and the Masses of Gauge Bosons. *Phys.Rev.Lett.*, 13:508–509, 1964.

[3] S. Schael et al. Precision electroweak measurements on the Z resonance. *Phys.Rept.*, 427:257–454, 2006.

[4] M. Gell-Mann. Symmetries of Baryons and Mesons. *Physical Review*, 125:1067–1084, February 1962.

[5] S. L. Glashow. Partial-symmetries of weak interactions. *Nuclear Physics*, 22:579–588, February 1961.

[6] J. Beringer et al. Review of Particle Physics (RPP). *Phys.Rev.*, D86:010001, 2012.

[7] John N. Bahcall, Aldo M. Serenelli, and Sarbani Basu. New solar opacities, abundances, helioseismology, and neutrino fluxes. *Astrophys.J.*, 621:L85–L88, 2005.

[8] A. Salam. Weak and Electromagnetic Interactions. *Conf.Proc.*, C680519:367–377, 1968.

[9] A. Bettini. *Introduction to Elementary Particle Physics.* Cambridge University Press, 2008.

[10] C. Grupen, G. Cowan, S. Eidelman, and T. Stroh. *Astroparticle Physics.* SpringerLink: Springer e-Books. Springer, 2005.

[11] A. Quadt. Top quark physics at hadron colliders. *The European Physical Journal C - Particles and Fields*, 48(3):835–1000, 2006.

[12] E.M. Henley and A. Garcia. *Subatomic Physics.* World Scientific Publishing Company, third edition, 2007.

[13] G. Kramer. *Theory of jets in electron-positron annihilation.* Springer tracts in modern physics. Springer-Verlag, 1984.

[14] E.W. Otten and C. Weinheimer. Neutrino mass limit from tritium beta decay. *Rept.Prog.Phys.*, 71:086201, 2008.

[15] Serguei Chatrchyan et al. Observation of a new boson at a mass of 125 GeV with the CMS experiment at the LHC. *Phys.Lett.*, B716:30–61, 2012.

[16] K. Winter. *Neutrino Physics.* Cambridge Monographs on Particle Physics, Nuclear Physics and Cosmology. Cambridge University Press, 2000.

[17] M. Goldhaber, L. Grodzins, and A. W. Sunyar. Helicity of neutrinos. *Phys. Rev.*, 109:1015–1017, Feb 1958.

[18] L. Wolfenstein. Neutrino oscillations in matter. *Phys. Rev. D*, 17:2369–2374, May 1978.

[19] Q.R. Ahmad et al. Measurement of the rate of $\nu_e + d \to p + p + e^-$ interactions produced by ^8B solar neutrinos at the Sudbury Neutrino Observatory. *Phys.Rev.Lett.*, 87:071301, 2001.

[20] N. Agafonova et al. Observation of a first candidate event in the opera experiment in the cngs beam. *Physics Letters B*, 691(3):138 – 145, 2010.

[21] R.N. Mohapatra, S. Antusch, K.S. Babu, G. Barenboim, Mu-Chun Chen, et al. Theory of neutrinos: A White paper. *Rept.Prog.Phys.*, 70:1757–1867, 2007.

[22] Th.M. Nieuwenhuizen. Do non-relativistic neutrinos constitute the dark matter? *Europhys.Lett.*, 86:59001, 2009.

[23] A. Goobar, S. Hannestad, E. Mörtsell, and H. Tu. The neutrino mass bound from WMAP 3 year data, the baryon acoustic peak, the SNLS supernovae and the Lyman-α forest. *Journal of Cosmology and Astroparticle Physics*, 6:19, June 2006.

[24] Shaun A. Thomas, Filipe B. Abdalla, and Ofer Lahav. Upper Bound of 0.28eV on the Neutrino Masses from the Largest Photometric Redshift Survey. *Phys.Rev.Lett.*, 105:031301, 2010.

[25] P.A.R. Ade et al. Planck 2013 results. XVI. Cosmological parameters. 2013.

[26] Richard A. Battye and Adam Moss. Evidence for massive neutrinos from cosmic microwave background and lensing observations. *Phys. Rev. Lett.*, 112:051303, Feb 2014.

[27] Th.A. Mueller, D. Lhuillier, M. Fallot, A. Letourneau, S. Cormon, et al. Improved Predictions of Reactor Antineutrino Spectra. *Phys.Rev.*, C83:054615, 2011.

[28] G.L. Fogli, E. Lisi, A. Marrone, A. Palazzo, and A.M. Rotunno. Evidence of θ_{13} from global neutrino data analysis. *Phys.Rev.*, D84:053007, 2011.

[29] M. Gell-Mann and A. Pais. Behavior of neutral particles under charge conjugation. *Phys.Rev.*, 97:1387–1389, 1955.

[30] T. Adam et al. Measurement of the neutrino velocity with the OPERA detector in the CNGS beam. *JHEP*, 1210:093, 2012.

[31] M. Antonello et al. Measurement of the neutrino velocity with the ICARUS detector at the CNGS beam. *Phys.Lett.*, B713:17–22, 2012.

[32] Andrew G. Cohen, Sheldon L. Glashow, and Zoltan Ligeti. Disentangling Neutrino Oscillations. *Phys.Lett.*, B678:191–196, 2009.

[33] V. Hess. Nobel lecture, December 1936.

[34] W. Pauli. Dear radioactive ladies and gentlemen. *Phys.Today*, 31N9:27, 1978.

[35] Fred L. Wilson. Fermi's theory of beta decay. *American Journal of Physics*, 36(12):1150–1160, 1968.

[36] H. Bethe and R. Peierls. The 'neutrino'. *Nature*, 133:532, 1934.

[37] S.M. Bilenky. Neutrino. History of a unique particle. *Eur.Phys.J.*, H38:345–404, 2013.

[38] C. L. Cowan, F. Reines, F. B. Harrison, H. W. Kruse, and A. D. McGuire. Detection of the free neutrino: a confirmation. *Science*, 124(3212):103–104, 1956.

[39] D.J. Griffiths. *Introduction to elementary particles*. Physics textbook. Wiley, 1987.

[40] G. Danby, J.M. Gaillard, Konstantin A. Goulianos, L.M. Lederman, Nari B. Mistry, et al. Observation of High-Energy Neutrino Reactions and the Existence of Two Kinds of Neutrinos. *Phys.Rev.Lett.*, 9:36–44, 1962.

[41] S.H. Neddermeyer and C.D. Anderson. Note on the Nature of Cosmic Ray Particles. *Phys.Rev.*, 51:884–886, 1937.

[42] Raymond Davis, Don S. Harmer, and Kenneth C. Hoffman. Search for neutrinos from the sun. *Phys. Rev. Lett.*, 20:1205–1209, May 1968.

[43] John N. Bahcall, Aldo M. Serenelli, and Sarbani Basu. New solar opacities, abundances, helioseismology, and neutrino fluxes. *Astrophys.J.*, 621:L85–L88, 2005.

[44] B. Pontecorvo. Mesonium and anti-mesonium. *Sov.Phys.JETP*, 6:429, 1957.

[45] Ziro Maki, Masami Nakagawa, and Shoichi Sakata. Remarks on the unified model of elementary particles. *Prog.Theor.Phys.*, 28:870–880, 1962.

[46] K.S. Hirata et al. Observation of B-8 Solar Neutrinos in the Kamiokande-II Detector. *Phys.Rev.Lett.*, 63:16, 1989.

[47] W. David Arnett and Jonathan L. Rosner. Neutrino mass limits from sn1987a. *Phys. Rev. Lett.*, 58:1906–1909, May 1987.

[48] M. L. Perl et al. Evidence for anomalous lepton production in e+ e- annihilation. *Phys. Rev. Lett.*, 35:1489–1492, Dec 1975.

[49] Martin L. Perl. Evidence for, and Properties of, the New Charged Heavy Lepton. 1977.

[50] D. Decamp et al. Determination of the Number of Light Neutrino Species. *Phys.Lett.*, B231:519, 1989.

[51] K. Kodama et al. Observation of tau neutrino interactions. *Phys.Lett.*, B504:218–224, 2001.

[52] D.H. Perkins. *Particle Astrophysics, Second Edition*. Oxford Master Series in Physics. OUP Oxford, 2009.

[53] C.D. Anderson. The positive electron. *Phys. Rev.*, 43:491–494, Mar 1933.

[54] M.G. Aartsen et al. Evidence for High-Energy Extraterrestrial Neutrinos at the IceCube Detector. *Science*, 342(6161):1242856, 2013.

[55] Enrico Fermi. On the Origin of the Cosmic Radiation. *Phys.Rev.*, 75:1169–1174, 1949.

[56] M. Ackermann et al. Detection of the characteristic pion-decay signature in supernova remnants. *Science*, 339(6121):807–811, 2013.

[57] J.K. Becker. High-energy neutrinos in the context of multimessenger astrophysics. *Physics Reports*, 458(4):173–246, 2008.

[58] A.G. Cocco, G. Mangano, and M. Messina. Probing low energy neutrino backgrounds with neutrino capture on beta decaying nuclei. *Journal of Cosmology and Astroparticle Physics*, 2007(06):015, 2007.

[59] M.G. Aartsen et al. Probing the origin of cosmic-rays with extremely high energy neutrinos using the IceCube Observatory. *Phys.Rev.*, D88:112008, 2013.

[60] K. Greisen. End to the cosmic-ray spectrum? *Phys. Rev. Lett.*, 16:748–750, Apr 1966.

[61] G. T. Zatsepin and V. A. Kuz'min. Upper Limit of the Spectrum of Cosmic Rays. *Soviet Journal of Experimental and Theoretical Physics Letters*, 4:78, August 1966.

[62] I.M. Frank and I. Tamm. Coherent visible radiation of fast electrons passing through matter. *C.R.Acad.Sci.URSS*, 14:109–114, 1937.

[63] G.F. Knoll. *Radiation Detection and Measurement*. John Wiley & Sons, 2010.

[64] J.A. Formaggio and G.P. Zeller. From eV to EeV: Neutrino Cross Sections Across Energy Scales. *Rev.Mod.Phys.*, 84:1307, 2012.

[65] R. Abbasi et al. Calibration and Characterization of the IceCube Photomultiplier Tube. *Nucl.Instrum.Meth.*, A618:139–152, 2010.

[66] Francis Halzen and Spencer R. Klein. Invited review article: Icecube: An instrument for neutrino astronomy. *Review of Scientific Instruments*, 81(8):–, 2010.

[67] R. Abbasi et al. The IceCube Data Acquisition System: Signal Capture, Digitization, and Timestamping. *Nucl.Instrum.Meth.*, A601:294–316, 2009.

[68] R. Abbasi et al. The Design and Performance of IceCube DeepCore. *Astropart.Phys.*, 35:615–624, 2012.

[69] M. Ackermann et al. Optical properties of deep glacial ice at the south pole. *Journal of Geophysical Research: Atmospheres*, 111(D13):n/a–n/a, 2006.

[70] M. Voge. Ice shear measurement. "Ice shear measurement" on IceCube wiki, 2010.

[71] M.G. Aartsen et al. Observation of Cosmic Ray Anisotropy with the IceTop Air Shower Array. *Astrophys.J.*, 765:55, 2013.

[72] J. Ahrens et al. IceCube Preliminary Design Document. unpublished, October 2001.

[73] The IceCube Collaboration.

[74] John F. Beacom, Patrick Crotty, and Edward W. Kolb. Enhanced signal of astrophysical tau neutrinos propagating through earth. *Phys.Rev.*, D66:021302, 2002.

[75] D. Cowen. Tau Neutrinos in IceCube. Internal IceCube Report, June 2006.

[76] N. Whitehorn. Madison python primer 2010-02-04. "Madison Python Primer 2010-02-04" on IceCube wiki, 2010.

[77] A.M. Dziewonski and D.L. Anderson. Preliminary reference earth model. *Phys.Earth Planet.Interiors*, 25:297–356, 1981.

[78] G.C. Hill. Generation and weighting of neutrino-induced events with the "nusim" monte carlo simulation. Internal IceCube Report, 1999.

[79] K. Hoshina. Neutrino generator/weighting. "Neutrino Generator/Weighting" on IceCube wiki, 2012.

[80] E. Blaufuss. "tft 2010 season planning". "TFT 2010 Season Planning" on IceCube wiki, 2009.

[81] A Ishihara and S. Yoshida. Ic77ehefilter. "IC77EHEFilter" on IceCube wiki, 2009.

[82] S. Seunarine. 2010 request for online cascade filter. "Internal IceCube Report", 2009.

[83] M.G. Aartsen et al. Observation of High-Energy Astrophysical Neutrinos in Three Years of IceCube Data. 2014.

the end